Passive and Active Control of Radiative Heat Flow

Thesis by
Nathan H. Thomas

In Partial Fulfillment of the Requirements for the
Degree of
Doctor of Philosophy

CALIFORNIA INSTITUTE OF TECHNOLOGY
Pasadena, California

2019
Defended January 24, 2019

Nathan H. Thomas
ORCID: 0000-0003-4648-5325

ACKNOWLEDGEMENTS

I have had the good fortune of working with and receiving help from many people at Caltech. These people used their precious time to teach me much of what I know and provided me both emotional and intellectual support when I needed it most. Without these people, this thesis surely would have never been written, and I am eternally grateful to them.

Firstly, I would like to extend heart-felt thanks to my adviser, Prof. Austin Minnich. Thank you, not only for accepting me into the lab late, long after first year courses had ended, but also thank you for your patience, accessibility, and above all, your persistent support in the face of our risky endeavours. You gave me the opportunity to take on some risky challenges (some worked and many failed), which has ultimately made me feel my PhD worthwhile.

I would also like to thank the members of my committee, Prof. Harry Atwater, Prof. Julia Greer, and Prof. Andrei Faraon. Your appetite for collaboration is unparalleled. Not only have I received guidance from you directly, but I have also worked closely with people in each of your research groups. I am particularly grateful to Harry, who opened his lab to me for my experiments and even provided one-on-one academic and career advice when time would allow.

I also received a great deal of help from Prof. George Rossman, whose time and resources were vital to my research. George's positive attitude and excitement for scientific exploration are contagious. Thank you also to the students and post-docs in the Atwater lab who helped train me: Sunita Darbe, Carissa Eisler, Jeremy Broulliet, Will Whitney, Rebecca Glaudell, Kelly Mauser, Rebecca Saive, Yulia Tolstova, and Ognjen Ilic. Special thanks goes to my partner in near field heat transport, Michelle Sherrott, who taught me everything I know about graphene and nanofabrication.

Thank you also to the Minnich group, past and present. Ding Ding took me under his wing when I first joined the thermal radiation group. Hang Zhang and Xiangwen Chen first helped me with sample fabrication and characterization. Navaneeth Ravichandran helped me get familiar with the numerical methods I needed for my simulation work. Thank you also to Nick Doh, Peishi Cheng, Chengyun Hua, Zoila Jurado, and Andrew Robbins, who were wonderful office mates; and to Junlong Kou for your helpful discussions.

Many times over the last five and a half years I have leaned on the support staff at

Caltech, many of whom have become close friends: Jennifer Blankenship, Tiffany Kimoto, Sonya Lincoln, Felicia Hunt, Natalie Gilmore, Bruce Dominguez, and John Van Deusen. Jonathan Gross and Christy Jenstad deserve particular recognition for helping me navigate through much of grad school. Thank you also to Alex Wertheim, Bert Mendoza, Guy DeRose, Carol Garland, Nathan Lee, and the other staff in the Kavli Nanoscience Institute.

I think the greatest gift I have received from Caltech has been the lifelong friendships. To Andrew Robbins, Dylan Tozier, Nick Weadock, Michael Floyd, Ryan McMullen, Soichi Hirokawa, and the former members of Steuben House, thank you for making Caltech feel like home.

Finally, thank you to my family. It feels a little silly trying to write down in words just how grateful I am to my parents Ann and Glenn and my brother Steve. But thank you for everything. And to my wife Sarah, who carried much of the pressure of this work and did it with dignity and grace, thank you, I couldn't have done it with you.

Two-by-two.

ABSTRACT

Materials that control the absorption and emission of thermal radiation have attracted renewed interest for energy applications. Materials of interest include those with static optical properties that vary with photon wavelength in a desired manner as well as those with dynamic properties that can be actively tuned by external stimuli. The research in this thesis focuses on creating materials in both categories.

First, we examine selective absorbers for solar thermal energy conversion with high absorptivity in solar wavelengths and low emissivity in infrared wavelengths. Achieving stagnation temperatures exceeding 200 °C with unconcentrated sunlight, pertinent to technologies like industrial process heat, air conditioning, and electricity generation, requires better spectrally selective absorbers with ultra-low thermal emittance. Current state-of-art surfaces are based on ceramic-metal mixtures and patterned metal or metal-dielectric structures. Semiconductor based selective surfaces with near zero absorption below the bandgap offer the potential for lower thermal emittance than that achieved with such surfaces that employ metals in the primary absorbing medium. In this thesis, we report a semiconductor-based multilayer selective absorber that exploits the sharp drop in optical absorption at the band gap energy to achieve a measured absorptance of 76% at solar wavelengths and a low emittance of approximately 5% at thermal wavelengths. In field tests, we obtain a peak temperature of 225 °C, comparable to that achieved with state-of-the-art selective surfaces. With straightforward optimization to improve solar absorption, our work shows the potential for unconcentrated solar thermal systems to reach stagnation temperatures exceeding 300 °C, higher than any available selective surface. Our surface would eliminate the need for solar concentrators for mid-temperature solar applications such as supplying process heat.

Second, we theoretically propose and experimentally implement a thermal switch for near-field radiative transfer. In the field of active thermal materials for manipulating heat flow in a controllable and reversible manner, numerous approaches to perform thermal switching have been reported. However, they typically suffer from various limitations, including small switching ratio or requiring large temperature differentials. We report the experimental implementation of a scheme to electrostatically control near-field radiative transfer in a graphene field effect heterostructure. We measure a maximum heat flux modulation of 4 ± 3% and an absolute heat flux modulation rate of 24 ± 7 $\mathrm{mWm^{-2}}$ per V bias. Employing gate

dielectrics with lower surface warp and higher dielectric breakdown strength as well as reducing conductive losses would enable modulations up to 100%, substantially exceeding the switching ratios achievable by other methods. Our work paves the way for electrostatic control of near-field radiative transfer using two-dimensional materials.

PUBLISHED CONTENT AND CONTRIBUTIONS

[1] Ognjen Ilic, Nathan H. Thomas, Thomas Christensen, Michelle C. Sherrott, Marin Soljačić, Austin J. Minnich, Owen D. Miller, and Harry A. Atwater. Active Radiative Thermal Switching with Graphene Plasmon Resonators. *ACS Nano*, March 2018. doi: 10.1021/acsnano.7b08231.
N. H. Thomas expanded the thermal switching idea to systems with optically active substrates, performed confirming calculations, and assisted in writing the manuscript.

[2] Nathan H. Thomas, Zhen Chen, Shanhui Fan, and Austin J. Minnich. Semiconductor-based Multilayer Selective Solar Absorber for Unconcentrated Solar Thermal Energy Conversion. *Scientific Reports*, 7(1):5362, July 2017. doi: 10.1038/s41598-017-05235-x.
N. H. Thomas designed the selective surface, performed materials characterization, and wrote the manuscript.

[3] Nathan H. Thomas, Michelle C. Sherrott, Jeremy Broulliet, Harry A. Atwater, and Austin J. Minnich. Electronic Modulation of Near Field Radiative Transfer in Graphene Field Effect Heterostructures. *In preparation*, 2019.
N. H. Thomas built the measurement apparatus, fabricated the samples, conduced theoretical modeling, and wrote the manuscript.

TABLE OF CONTENTS

LIST OF ILLUSTRATIONS

LIST OF TABLES

Chapter 1

INTRODUCTION

Light carries heat. Anyone reading this thesis in Pasadena, CA on a summer day understands this concept well. Reading this in the shade is considerably more pleasant than in the direct sunshine. What it means in a thermodynamic context (as opposed to a meteorological one) is that any two objects in optical contact are exchanging radiative thermal energy. There is a net flux of heat (light) from the body at a higher temperature to the body at a lower temperature.

The second half of the 19th century and the turn of the 20th saw a flurry of scientific progress in this area of thermal radiation. In 1860, Gustav Kirchhoff proved theoretically that the fraction of light an object absorbs is also the fraction of thermal radiation it emits; absorptance equals emittance. Conversely, if an object is not absorptive it is also not emissive. This is often referred to as *Kirchhoff's law of thermal radiation* and is referenced often in this thesis [1]. In 1896, Wilhelm Wien gave an empirical and approximate formulation for the wavelength dependent nature of thermal radiation, sometimes called the *Wien displacement law*, upon which Max Planck improved with the theoretical derivation of *Planck's law* in 1900 [2, 3]. Planck's law is often referred to as the black body distribution. Plots showing the wavelength dependent nature of the black body distribution at different temperatures are shown in Fig. 1.1.

The laws of thermal radiation developed at this time are valid in the regime known as the "far-field," where the distance between radiating bodies is much larger than wavelength of light. The quintessential example for such a system is the earth and the sun. From the point of view of the earth, we see two different and distant thermal objects. There is the obvious one, the sun, with a surface temperature of about 5770 K. Then there is deep space itself, sometimes called the "Cosmic Microwave Background," with a temperature of 2.725 K. A basic heat transfer calculation with the earth gaining heat from the sun and losing heat to deep space shows that to first approximation the earth should have a temperature of 271 K.[4] The actual actual answer is ~290 K, where the discrepancy is due to the greenhouse effect.

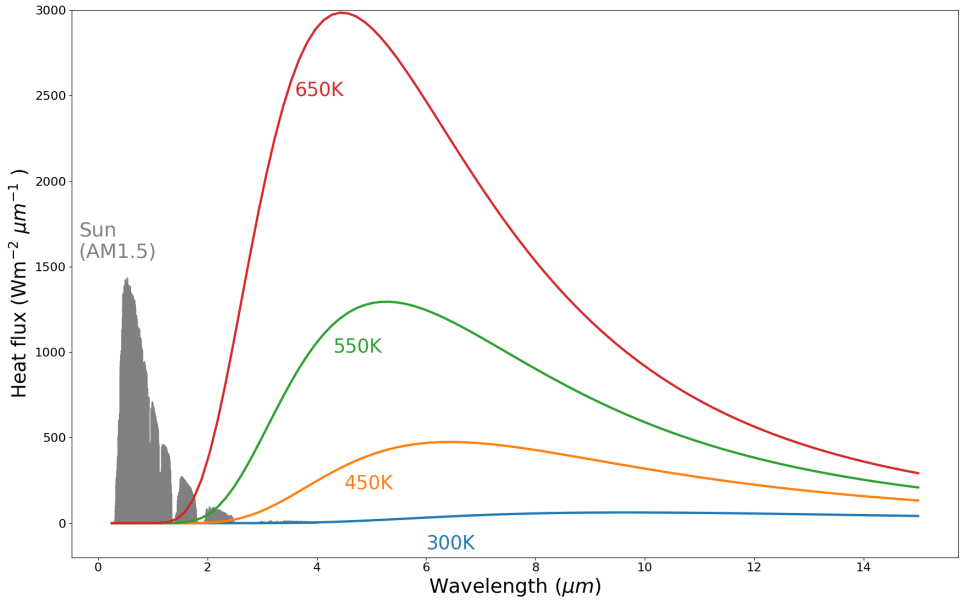

Figure 1.1: Solar (AM1.5) spectrum (grey) and the black body distribution at various temperatures. Because the surface temperature of the sun is so high, its emission spectrum is at considerably shorter wavelengths than even an object at 650 K.

Evident in Figure 1.1, thermally distributed light in the far field is broadband, spanning many microns. However, as the surface of the sun is so much hotter than the surface of the earth (thankfully), the light radiating from the sun is at much shorter wavelengths than the light coming from even moderately hot objects ($T < 650$ K) on the earth. A more general statement is also valid; that objects at different temperatures with different wavelength specific optical properties emit different radiative spectra. By modifying materials' optical properties at thermal wavelengths, we can alter how they are thermodynamically coupled to their environment and to one another.

1.1 Radiation in the Far Field

As this concept is one fundamentally about energy flow between materials, the study of thermal radiation has seen rapid development with the field of materials science, particularly in energy conversion technologies. For example, solar thermal photovoltaics offer the potential to surpass thermodynamic limitations for solar cells in conversion of sunlight into electricity [5–8]. Such devices absorb the entire solar spectrum, converting the solar flux into heat, and subsequently radiate that heat to a photovoltaic cell. In 2018, Omair and others from the Yablanovitch group at U.C. Berkeley reported thermophotovoltaic efficiences exceeding 28% [9]. Efforts in this

area have also focused on tailoring of thermal emission, making it narrow band and better suited for emission into a photovoltaic [10].

Progress has also been made in the area of radiative cooling, which takes advantage of our radiative coupling to the cold depths of space [11, 12]. Earth's atmosphere is transparent at wavelengths from 8 microns to 13 microns, which coincides with the peak of the black body spectrum at room temperature. Raman et al. from the Fan group at Stanford first demonstrated radiative cooling in the daytime with a device that was highly emissive at these wavelengths while also reflective of sunlight [13]. Since then additional progress has been made with even simpler systems of UV-grade silica and silver [14, 15]. Devices can now reach temperatures well below freezing despite direct solar illumination [16].

The primary area of study for materials development in the field of thermal radiation is in efficient photothermal energy conversion of sunlight. In 1956, Harry Tabor first theorized a wavelength "selective surface" that would only absorb and emit radiation at solar wavelengths but would reflect and thereby trap radiation at longer infrared wavelengths [17]. Instead of wasting heat to radiative emission, the surface temperature increases. Such materials are used for flat plate solar hot water collection around the world [18]. Active research in selective surfaces is still ongoing with new developments in ceramic-metal mixtures, nanophotonic metal-dielectrics, and patterned metallic surfaces[19–26]. Cao et al. developed a state of the art selective surface that absorbed 91% of sunlight while losing only 13% to radiative losses at 500 °C. However, even these developments for solar thermal energy conversion employ metal structures like nanoparticles or lithographic patterns that have non-negligible infrared emission. In Chapter 2 of this thesis, we design and characterize a semiconductor-dielectric selective surface making use of infrared transparent materials to exhibit ultra-low thermal emittance.

1.2 Radiation in the Near Field

One feature of the materials mentioned so far is that they radiate to the far field, where the fundamental limit on heat transfer is comparatively quite low. In the "near field," however, where the distance between radiating bodies is on the order of the wavelength of transmitted light, these limits can be overcome. At these length scales, Planck's Law is no longer valid as additional modes of light can tunnel from one medium to the next, enhancing the total heat flow, potentially by many orders [27–35]. Ultimately, the limit on radiative heat transfer even in the near field

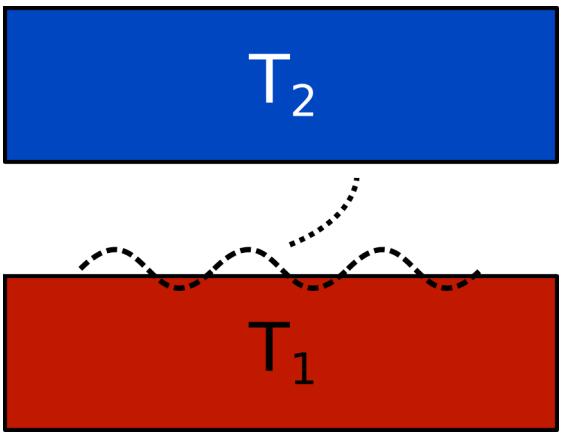

Figure 1.2: Diagram of surface mode coupling between two objects in the near field

is the conductive limit, where the distance between objects is zero [36].

The additional modes that contribute to heat flow are evanescent surface waves (resonances) with electric and magnetic field amplitudes that exponentially decay away from the object's surface; see Figure 1.2 [37]. When the gap spacing between objects is sufficiently small, these field amplitudes do not decay to negligible levels before encountering the next object, where the light may be absorbed. Materials that support optical resonances are therefore of considerable interest. Polar materials with sharp optical phonon resonances, like SiC or SiO_2, are often used in both theoretical and experimental works for near field heat transfer [38, 39].

Hyperbolic metamaterials, which promote tuned optical resonances based on assigned geometry, can couple near field optical modes into the far field [40–42]. Such applications are found in imaging, sensing, and radiative cooling [43–46]. Plasmonic materials like metals or doped semiconductors also support surface modes where light couples to dipole excitations in a free electron gas that also contribute to near field heat flux [47–49].

1.3 Graphene: Tunable Plasmonic Material

Graphene, a single layer of sp^2 bonded C atoms arrayed in honeycomb pattern, is the plasmonic material investigated in this thesis for near field heat transfer. The crystal structure and reciprocal lattice are shown in Figure 1.3. A consequence of graphene's honeycomb crystal structure is that the graphene electronic band structure, shown in Figure 1.4, exhibits a linear dispersion near the K and K' points,

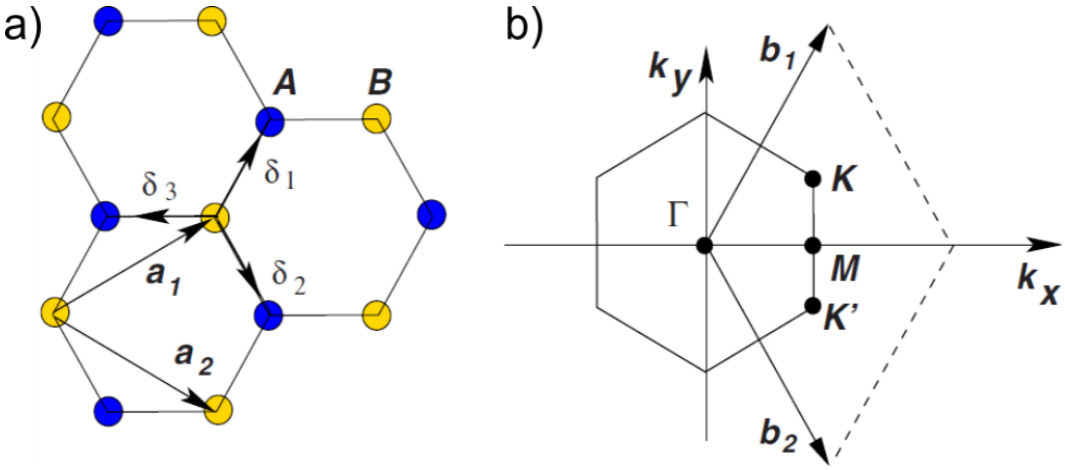

Figure 1.3: Adapted from Costra et al. [50]. (a) Graphene honeycomb crystal structure and (b) reciprocal lattice. Graphene exhibits a linear dispersion relation near the K and K' points, called Dirac points, as shown in Figure 1.4.

where the charge carrier energy is proportional to the wavevector, $E = v_F|k|$. The proportionality constant v_F is the Fermi velocity, roughly equal to 1/300 the speed of light. This linear relationship extends down to zero wavevector and zero Fermi level at the Dirac point.

Graphene does not have a bandgap, and at the Dirac point, the charge carrier concentration is minimized (theoretically zero). Here, there is no free electron gas, and no surface plasmons are supported. However, as the electron chemical potential (Fermi level) changes, which can be achieved with chemical doping or an applied electric field, so too does the carrier concentration. Graphene behaves more like a metal and exhibits surface plasmons. The oscillation frequency of the surface plasmons, often called the plasma frequency, is proportional to the square root of the Fermi level. A complete review of the electronic transport properties of graphene can be found in Sarma et al. [51].

The plasmon resonance dependence on Fermi level makes graphene intrinsically tunable through the application of an external electric field. Such gate tuning of graphene plasmons has been experimentally demonstrated in nanoribbon geometries, and Brar et al. further showed that the far-field emission of thermal radiation from graphene/*h*BN structures could by modulated [52–54].

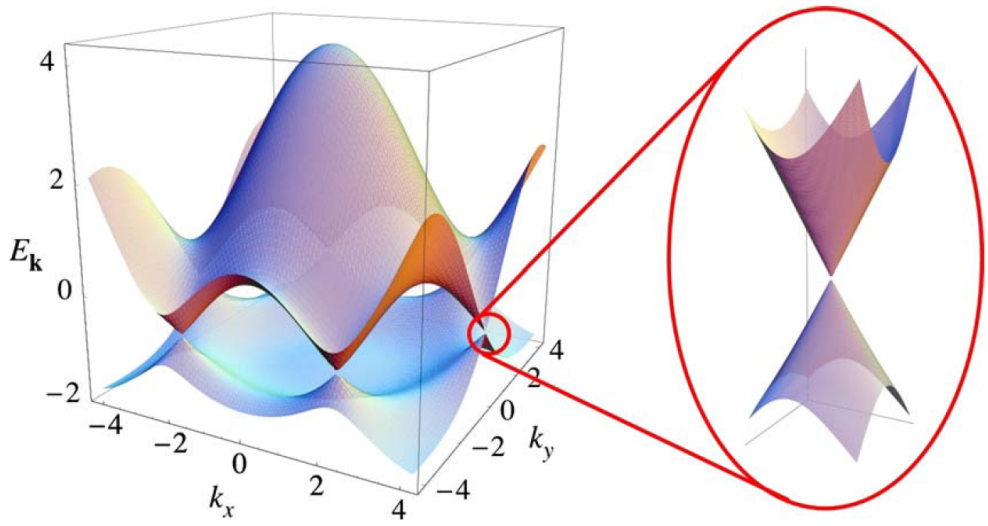

Figure 1.4: Adapted from Costra et al. [50]. Graphene band structure, calculated via a tightbinding method, and a zoomed-in image at one of the Dirac points, showing the linear dispersion

Alongside the development of 2-dimensional materials, there has also been rapid improvement in experimental techniques to probe the limits of near field radiation. In 1970, Domoto et al. first explored radiative transfer between metallic plates spaced 50 μm [55]. Hargreaves made further improvement in 1973 between plates of Cr spaced 1 μm apart [56]. However, as both of these works employed metals, which are poor thermal emitters, the measured heat flux was still below the black body limit. It wasn't until 2008 that Hu et al. in the Chen group at MIT first measured radiative heat flux enhancement beyond the black body limit between parallel plates of glass [38]. In the same year, work from Shen and Narayanswamy from the same group extended these experiments to other geometries, e.g. between a sphere and a plane [57]. Subsequent development of the sphere-plane system came from Shen et al. in 2009 and 2012 [49, 58].

Recently, since 2015, great experimental progress in measuring near field heat flux has come out of the Reddy group at the University of Michigan. Kim et al. reported vacuum gap spacing separating two objects as small two nanometers in the case of an atomic force microscope tip and a planar substrate, confirming the conventional theory of fluctuational electrodynamics down to these length scales [30]. Between two planar samples, a gap spacing as small as 30 nm has been reported from Fiorino et al. [34, 35]. These experimental techniques rely on careful placement

of microscopic samples with nanometer precision. Alternative techniques from the Zhang group at Georgia Tech, Kato Ito at Toyota Central Research and Development Laboratories, and Hiroshi Toshiyoshi at the University of Tokyo have also been developed to measure near field heat flux between larger scale samples on the order of 1 cm $\times$ 1 cm [29, 59].

Although great experimental progress has been made in the field of near field heat transfer, particularly in studying the vacuum gap dependence of heat flux to nanometer scales, a feature of these experiments is that the radiative properties of the materials are fixed. Heat flux cannot be tuned with an external signal. There has been theoretical work on modulation of thermal radiation in the near field through tuning of optical resonances or causing a metal-insulator phase transition in VO_2 [60–62]. But only recently in 2017 has heat flux modulation in the near field been demonstrated experimentally with VO_2 [63]. In this thesis, we use the tunability of graphene plasmons by electrostatic bias to experimentally modulate radiative heat flux in the near field.

1.4 Overview

This thesis is divided largely into two parts. The first studies passive control of radiation in the far-field in Chapter 2. A semiconductor-dielectric selective surface is proposed, fabricated, and characterized for the purpose of maximizing surface temperature under nonconcentrated sunlight. The second part of this thesis is a study of actively modulated heat transfer in the near field and is split over Chapters 3, 4, and 5. In Chapter 3, near field heat transfer is investigated theoretically, and a experimentally viable configuration is proposed. In Chapter 4, an experimental apparatus is designed to measure modulated heat transport and a sample fabrication protocol is developed. In Chapter 5, results from four samples are discussed. Finally, in Chapter 6, we conclude and provide a future outlook for the field of radiative heat transport.

Chapter 2

SEMICONDUCTOR-DIELECTRIC SELECTIVE SOLAR ABSORBER

Nathan H. Thomas, Zhen Chen, Shanhui Fan, and Austin J. Minnich. Semiconductor-based Multilayer Selective Solar Absorber for Unconcentrated Solar Thermal Energy Conversion. *Scientific Reports*, 7(1):5362, July 2017

2.1 Introduction

Solar thermal energy conversion is of intense interest due to environmentally sustainable applications in industrial heating, air conditioning, and electricity generation. [65–68] For instance, solar thermal input can be used for industrial process heat instead of furnaces or can replace the compressor in conventional air conditioning units [65, 66] Solar thermal energy can also be used for desalination of sea water, particularly in remote locations [69]

A key element of a solar thermal system is a selective surface that simultaneously maximizes solar absorption while minimizing parasitic heat losses due to infrared thermal emission. A non-selective black surface like carbon-black can only reach a maximum temperature of about 130 °C under unconcentrated sunlight. Selective surfaces were originally proposed in the 1950s, and numerous designs have been proposed since, including cermets, metal dielectric structures, and patterned metal surfaces [17, 19–26]. For example, Barshilia et al. developed a multilayer stack of $Al_xO_y/Al/Al_xO_y$ that is stable up to 400 °C in air and exhibits 96% solar absorptance and 7% thermal emittance [26]. Recently, Cao et al. used a calorimetric technique to determine the temperature dependent, hemispherical solar absorptance and thermal emittance of an yttria-stabilized zirconia cermet to be 91% and 13%, respectively at 600 °C [22].

Another approach for achieving spectral selectivity at moderate temperatures below 500 °C is to use semiconductors with appropriately chosen bandgaps. For photon

energies above the bandgap, semiconductors absorb strongly, while for sub-bandgap energies they absorb very little. Because of the near zero absorption below the bandgap, semiconductor based selective surfaces offer the potential for thermal emittance lower than that achieved with surfaces that employ textured metals in the primary absorbing medium. Further, the transition from absorbing to non-absorbing occurs over a very narrow bandwidth compared to that of traditional selective surfaces. Early work by Seraphin and others has demonstrated the potential of using semiconductors for solar thermal purposes [70–73]. However, semiconductors with small band-gaps suitable for absorbing the solar spectrum (0.6 eV to 1.4 eV) have a high refractive index and consequently require elaborate anti-reflection coatings. Standard materials for solar-cell anti-reflection coatings such as SiO_2, Si_3N_4, and TiO_2 are quite emissive in the mid-infrared, however, and are unsuitable for solar-thermal applications. As a result, the performance of semiconductor-based solar thermal absorbers has lagged that of metallic and ceramic counterparts.

In this chapter, we present a semiconductor-based multilayer stack that achieves the high solar absorption and low thermal emission necessary for unconcentrated solar thermal applications. We divide this chapter up into a two main parts. In the first, we introduce the transfer matrix method as a way to model the multilayer surface. In the second, we cover the fabrication and characterization of said surface.

2.2 Model Thin Film Optical Properties

There are several methods to calculate the reflection and transmission coefficients for layered, planar surfaces. Due to its intuitive nature and straightforward relation to physical quantities, the transfer matrix method is the preferred way in this thesis. A complete derivation can be found in Appendix A. A simplified formulation is shown here, where we consider the single layer sandwiched by two infinite half-spaces, shown in Figure 2.1.

Assuming a linearly polarized light wave propagating in the z direction towards the first interface, the electric field has forward and backward components[1]

$$\boldsymbol{E}(\boldsymbol{r},t) = E_y\hat{\boldsymbol{y}}e^{i(\boldsymbol{k}\cdot\boldsymbol{r}-\omega t)} = \left(E_y e^{ik_z z} + E'_y e^{-ik_z z}\right) e^{i(k_x x + k_y y - \omega t)}, \tag{2.1}$$

where $E_{x(y)}$ and $E'_{x(y)}$ are the forward and reverse propagating components, respectively. The wave vector components parallel to the interface are invariant, as is the

[1] A note on notation: All ***bold*** terms are vectors and terms with the $\hat{hat}$ are unit vectors.

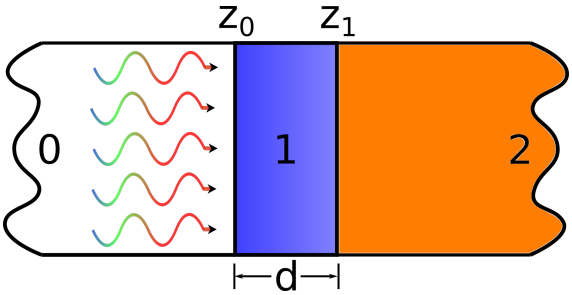

Figure 2.1: Diagram of a single thin film for transfer matrix analysis. Light starts in semi-infinite medium 0 and propogates towards the interface at z_0 with medium 1, a thin film of thickness d, which lies on semi-infinite substrate, medium 2.

time dependence. Hence, to model the refraction, we need only consider the wave vectors in z. As outlined in Appendix A, the amplitudes of the electric field refracted at the interface between media 0 and 1 are modeled with the matrix equation

$$M^{(0)}(z_0)\begin{bmatrix} E^{(0)}_{x(y)} \\ E'^{(0)}_{x(y)} \end{bmatrix} = M^{(1)}(z_0)\begin{bmatrix} E^{(1)}_{x(y)} \\ E'^{(1)}_{x(y)} \end{bmatrix}, \tag{2.2}$$

where the matrix M for transverse magnetic (TM) polarized light for a given layer j is equal to

$$M^{(j)}(z) = \begin{bmatrix} e^{ik_z^{(j)}z} & e^{-ik_z^{(j)}z} \\ \frac{\epsilon_{xx}^{(j)}}{k_z^{(j)}} e^{ik_z^{(j)}z} & -\frac{\epsilon_{xx}^{(j)}}{k_z^{(j)}} e^{-ik_z^{(j)}z}, \end{bmatrix} \tag{2.3}$$

and for transverse electric (TE) polarized light is equal to

$$M^{(j)}(z) = \begin{bmatrix} e^{ik_z^{(j)}z} & e^{-ik_z^{(j)}z} \\ -\frac{k_z^{(j)}}{\mu^{(j)}} e^{ik_z^{(j)}z} & \frac{k_z^{(j)}}{\mu^{(j)}} e^{-ik_z^{(j)}z} \end{bmatrix}. \tag{2.4}$$

Hence, for the three layer system shown in Figure 2.1 without any conductive interfaces, we get the matrix equation for TE light[2]:

$$\begin{bmatrix} 1 \\ r \end{bmatrix} = M^{(1)}(z_0)^{-1} M^{(2)}(z_0) M^{(2)}(z_1)^{-1} M^{(3)}(z_1) \begin{bmatrix} t \\ 0 \end{bmatrix}, \tag{2.5}$$

where

$$M^{(j)}(z) = \begin{bmatrix} e^{ik_z^{(j)}z} & e^{-ik_z^{(j)}z} \\ -\frac{k_z^{(j)}}{\mu^{(j)}} e^{ik_z^{(j)}z_0} & \frac{k_z^{(j)}}{\mu^{(j)}} e^{-ik_z^{(j)}z_0} \end{bmatrix}. \tag{2.6}$$

We can split M into two matrices to aid in multiplication and inversion:

$$M^{(j)}(z) = \begin{bmatrix} 1 & 1 \\ -\frac{k_z^{(j)}}{\mu^{(j)}} & \frac{k_z^{(j)}}{\mu^{(j)}} \end{bmatrix} \begin{bmatrix} e^{ik_z^{(j)}z} & 0 \\ 0 & e^{-ik_z^{(j)}z} \end{bmatrix} \equiv K_{(j)} \begin{bmatrix} e^{ik_z^{(j)}z} & 0 \\ 0 & e^{-ik_z^{(j)}z} \end{bmatrix} \tag{2.7}$$

[2]Calculations for TM light follow analogously.

Hence the inverse of M is

$$M^{(j)}(z)^{-1} = \begin{bmatrix} e^{-ik_z^{(j)}z} & 0 \\ 0 & e^{ik_z^{(j)}z} \end{bmatrix} \begin{bmatrix} \frac{1}{2} & \frac{\mu^{(j)}}{2k_z^{(j)}} \\ \frac{1}{2} & -\frac{\mu^{(j)}}{2k_z^{(j)}} \end{bmatrix} \equiv \begin{bmatrix} e^{-ik_z^{(j)}z} & 0 \\ 0 & e^{ik_z^{(j)}z} \end{bmatrix} K_{(j)}^{-1} \tag{2.8}$$

Now we can rewrite Eq. 2.5 to be

$$\begin{bmatrix} 1 \\ r \end{bmatrix} = \begin{bmatrix} e^{-ik_z^{(1)}z_0} & 0 \\ 0 & e^{ik_z^{(1)}z_0} \end{bmatrix} K_{(1)}^{-1} K_{(2)} \begin{bmatrix} e^{ik_z^{(2)}z_0} & 0 \\ 0 & e^{-ik_z^{(2)}z_0} \end{bmatrix} \begin{bmatrix} e^{-ik_z^{(2)}z_1} & 0 \\ 0 & e^{ik_z^{(2)}z_1} \end{bmatrix} K_{(2)}^{-1} K_{(3)} \begin{bmatrix} e^{ik_z^{(3)}z_1} & 0 \\ 0 & e^{-ik_z^{(3)}z_1} \end{bmatrix} \begin{bmatrix} t \\ 0 \end{bmatrix}. \tag{2.9}$$

Consolidating terms we get

$$\begin{bmatrix} 1 \\ r \end{bmatrix} = \begin{bmatrix} e^{-ik_z^{(1)}z_0} & 0 \\ 0 & e^{ik_z^{(1)}z_0} \end{bmatrix} K_{(1)}^{-1} K_{(2)} \begin{bmatrix} e^{-ik_z^{(2)}d} & 0 \\ 0 & e^{ik_z^{(2)}d} \end{bmatrix} K_{(2)}^{-1} K_{(3)} \begin{bmatrix} e^{ik_z^{(3)}z_1} & 0 \\ 0 & e^{-ik_z^{(3)}z_1} \end{bmatrix} \begin{bmatrix} t \\ 0 \end{bmatrix}, \tag{2.10}$$

where $d = z_1 - z_0$ is the thickness of the layer.

In general, the multilayered system starts at $z_0 = 0$, so the first matrix in Eq. 2.10 is simply the identity. Secondly, the last matrix in Eq. 2.10 only acts to provide a phase relation of $e^{\pm ik_z^{(3)}z_1}$. We can always add this phase later if necessary, but as is more often the case, we care more about the *magnitude* of the reflection and transmission coefficients, generally referred to as the reflectance and the transmittance. In that case, the phase is irrelevant. Therefore, for simplicity, we remove the final matrix as well, and get the following relation for the transfer matrix:

$$M = K_{(1)}^{-1} K_{(2)} \begin{bmatrix} e^{-ik_z^{(2)}d} & 0 \\ 0 & e^{ik_z^{(2)}d} \end{bmatrix} K_{(2)}^{-1} K_{(3)} \tag{2.11}$$

This is a particularly convenient form as it immediately allows us to write the transfer matrix for more layered structures. For example, the 4-layer case reduces to

$$M = K_{(1)}^{-1} K_{(2)} \begin{bmatrix} e^{-ik_z^{(2)}d_1} & 0 \\ 0 & e^{ik_z^{(2)}d_1} \end{bmatrix} K_{(2)}^{-1} K_{(3)} \begin{bmatrix} e^{-ik_z^{(3)}d_2} & 0 \\ 0 & e^{ik_z^{(3)}d_2} \end{bmatrix} K_{(3)}^{-1} K_{(4)}, \tag{2.12}$$

where $d_1 = z_1 - z_0$ and $d_2 = z_2 - z_1$. In which case for TM polarized light, the reflectance and transmittance is

$$R = \left| \frac{M[2,1]}{M[1,1]} \right|^2 \tag{2.13}$$

$$T = \left| \frac{\epsilon_{xx}^{(4)}}{\epsilon_{xx}^{(1}} \frac{k_z^{(1}}{k_z^{(4)}} \frac{1}{M[1,1]} \right|^2 \tag{2.14}$$

and for TE light

$$R = \left| \frac{M[2,1]}{M[1,1]} \right|^2 \tag{2.15}$$

$$T = \left| \frac{1}{M[1,1]} \right|^2 . \tag{2.16}$$

2.3 Optimization for Spectral Selectivity

Having motivated the method to calculate theoretical reflectance and transmittance values for layered structures, we can now optimize the layers for spectrally selective solar absorption. The criteria for an optimal selective solar absorber are well defined. The goal is to maximize absorption at solar wavelengths and to minimize absorption beyond a certain wavelength cutoff. Assuming a perfectly opaque surface (as is often the case), these criteria are equivalent to minimizing reflectance above this cutoff and maximizing reflectance below it. Although we are limiting the optimization space by considering only 1-dimensional multilayer structures, there are still a number of factors to consider.

We begin by discussing the constituent materials for a multilayer stack needed to achieve the desired optical behavior. The most important component is the semiconductor that provides the spectrally selective absorption. The semiconductor bandgap energy must correspond to photon wavelength between 1 μm and 2 μm to absorb as much of the solar spectrum as possible. As semiconductors typically have large refractive index, additional materials with lower refractive index must be included in the stack to reduce visible wavelength reflections. For these materials, it is essential that they be transparent at wavelengths longer than the bandgap cutoff wavelength.

Considering these factors, we chose Ge as the semiconductor due to its favorable bandgap energy and CaF_2 as the dielectric for antireflection. CaF_2 has low refractive index of about 1.4 and is transparent in the infrared out to 20 μm, making it ideal for antireflection purposes in solar thermal applications [74]. For the primary back reflector, we chose Ag, sandwiched by two thin layers of Cr to improve semiconductor-metal film adhesion.

Room temperature deposited films of Ge tend to be amorphous, but thin films of amorphous Ge (aGe) have been shown to exhibit temperature stability at moderate

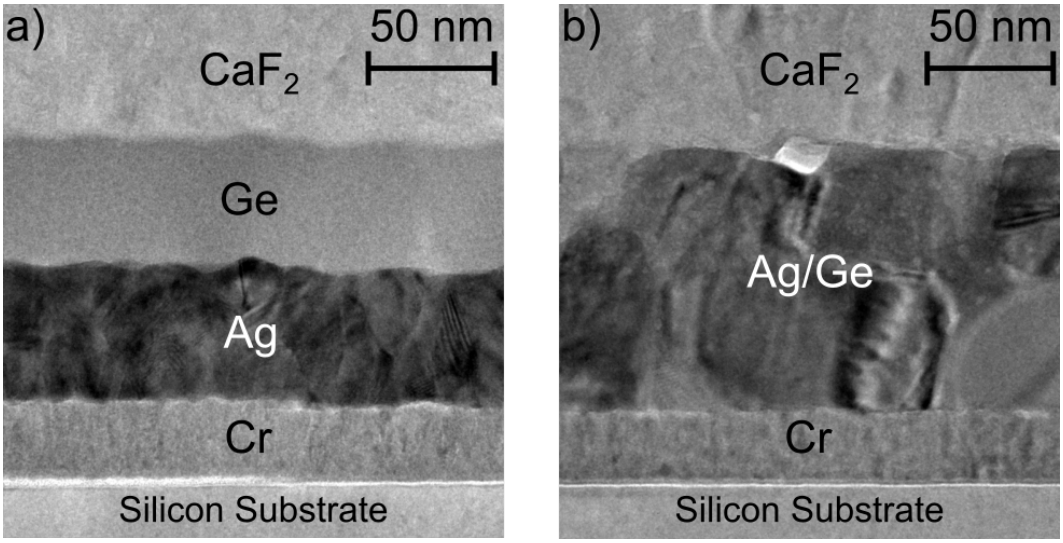

Figure 2.2: Cross section TEM of test sample (a) before and (b) after temperature cycling to 450 °C. There is clear mixing of the Ge and Ag layers. *TEM micrographs courtesy of Bryce Edwards and Peishi Cheng - MS122*

temperatures less than 300 °C [75, 76]. Amorphous Ge has different above-bandgap optical properties than those of its crystalline counterpart [77]. Therefore, to model the 1-D stack, we use the bulk refractive index of amorphous Ge but that of crystalline Cr, Ag, and CaF_2. We optimize the sequence and thickness of thin films of *a*Ge and CaF_2 for high reflectivity at wavelengths above 1.7 μm and low reflectivity below 1.5 μm using a needles method [78].

Beyond just optical properties, materials processing and temperature stability limitations must also be considered for optimizing the surface design. TEM micrographs of a test sample before and after temperature cycling to 450 °C are shown in Figures 2.2a and b, respectively. In the Figure 2.2a, before cycling, there is a clear delineation between the layers. However, after cycling, this delineation between the Ag and the Ge has disappeared and the layers have clearly mixed. The additional 5 nm layer of Cr between the Ag and the first Ge layer inhibits this mixing at high temperature. The optimization algorithm removes this Cr buffer layer, indicating a thin layer is necessary for optimal spectral selectivity. A table of the layer thicknesses is shown in Table 2.1, followed by a schematic of the optimized multilayer structure in Figure 2.3.

Layer	Material	Thickness (nm)
0	Cr	30
1	Ag	75
2	Cr	5
3	Ge	51
4	CaF_2	196
5	Ge	32
7	CaF_2	50
8	Ge	27
9	CaF_2	65
10	Ge	5
11	CaF_2	87

Table 2.1: Table of layer thicknesses

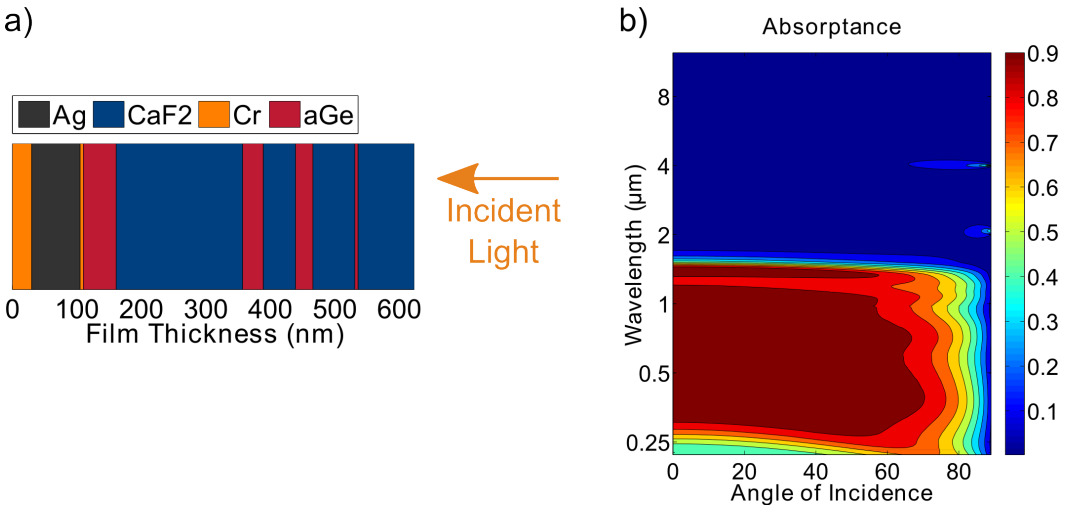

Figure 2.3: (a) Schematic of multilayer stack consisting of Ag, CaF_2, Cr, and *a*Ge. (b) Contour plot of simulated absorptance versus angle and wavelength of incident light. The simulated solar absorptance and thermal emittance is 86.4% and 4.4%, respectively.

The simulated absorptance of the structure at all incident angles is shown in Figure 2.3b. How efficiently a selective surface converts direct sunlight into usable heat is determined by two spectrally averaged quantities. The first is the solar absorptance, α_s:

$$\alpha_s = \frac{\int_0^\infty \alpha(\lambda) I_{AM1.5}(\lambda) d\lambda}{\int_0^\infty I_{AM1.5}(\lambda) d\lambda}, \tag{2.17}$$

where $\alpha(\lambda)$ is the spectral absorptance and $I_{AM1.5}(\lambda)$ is AM1.5 spectrum from the

sun. The second is the average thermal emittance, ϵ_t:

$$\epsilon_t = \frac{\int_0^{\pi}\int_0^{\pi/2}\int_0^{\infty} \alpha(\lambda,\theta) I_{BB}(T,\lambda)\cos\theta\sin\theta d\lambda d\theta d\phi}{\sigma T^4}, \tag{2.18}$$

where $I_{BB}(T,\lambda)$ is the black body distribution at temperature T, and σ is the Stefan-Boltzmann constant [79]. Using the simulated absorptance of the structure at all incident angles, shown in Figure 2.3b, we calculate the average solar absorptance to be 86.4% and the average thermal emittance to be 4.4%. In particular, the calculated emissivity is lower than those of prior reported works by over 50%, highlighting the potential of semiconductor-based selective absorbers for unconcentrated solar thermal applications for which low emissivity is essential [22, 25]. The solar absorptance can be further increased by introducing additional layers, but for simplicity we consider the stack as designed.

2.4 Fabrication of Device

Physical deposition methods are well suited for growth of thin film layers. Sputtering functions by igniting an Ar plasma, which ablates a material target, dispersing the target atoms omnidirectionally. They eventually adhere to the substrate and grow into films. Electron beam evaporation works by heating up a target crucible with a 10 kV electron beam. As the temperature of the target increases, so too does the vapor pressure, which eventually exceeds that of the surrounding vacuum chamber. The target material then evaporates and travels ballistically towards the substrate. Both of these growth techniques allow for multiple materials to be deposited on a surface in a single run without needing to remove the substrate from vacuum, which make them ideal for the fabrication of the surface proposed in Section 2.3.

The primary concern in depositing thin films is determining the deposition rate. In many systems, this is done with a quartz crystal microbalance. In our case for sputtering, we calibrate our system by growing multiple samples over different run times and measuring the film thickness with profilometry, ellipsometry, or x-ray reflectometry (XRR). Profilometry is well suited for films that grow fast enough such that a well defined step-edge is achieved. Ellipsometry works well for materials where the optical properties of thin films are well established, and XRR works for samples that are otherwise difficult to measure. An example XRR spectrum is shown in Figure 2.4 where the peak positions (called Kiessig fringes) are labeled with a dot. The index m and 2θ location of each peak is related to film thickness d by, $\theta^2 = \left(\frac{\lambda}{2d}m\right)^2 + \theta_c^2$, where λ is the x-ray wavelength and θ_c is the critical angle where the x-ray beam is totally internally reflected off the material interface [80].

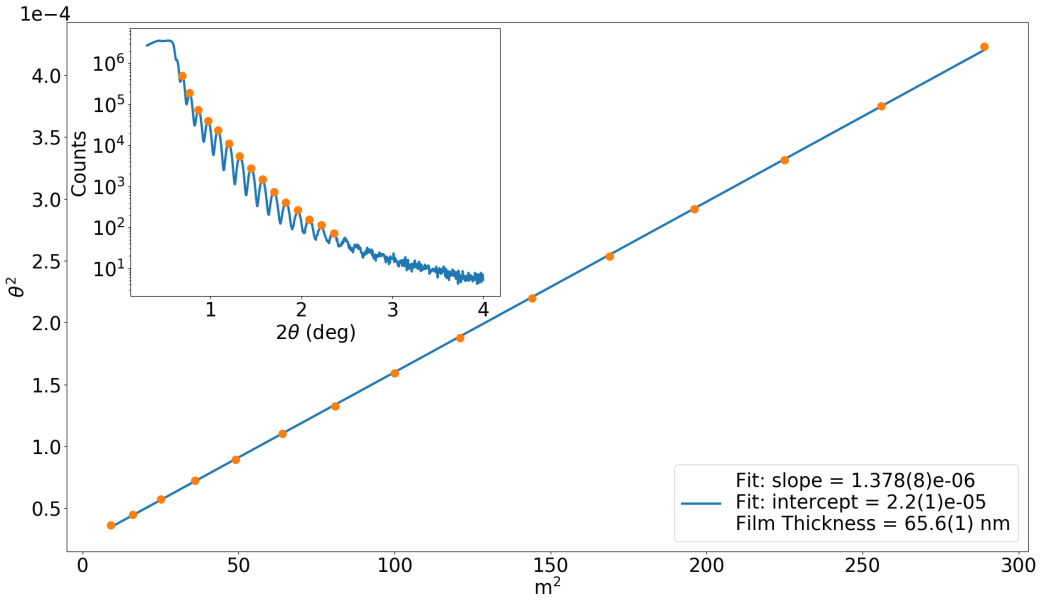

Figure 2.4: Representative x-ray reflectometry data and fit of $\theta^2 = \left(\frac{\lambda}{2d}m\right)^2 + \theta_c^2$, for $\lambda = 1.5406$Å Cu K-α x-rays. Inset: Raw signal for thin film of aGe. The peak maxima are marked with orange dots.

The measured deposition rates are shown in Figures 2.5. This deposition rate is found to be consistent for each Ag, Cr, and aGe over multiple runs. However, over the age of the CaF_2 target, the deposition rate was found to vary substantially (see inset of Figure 2.5). As a result, the final samples that exhibited the best spectral selectivity were ultimately grown by electron beam evaporation by a third party company, LGA Thin Films.

Cross-section micrographs of the selective surface sample fabricated by LGA Thin Films are shown in Figures 2.6a-b. The first layer of Ge, deposited on top of the Ag layer with the invisible 5 nm layer of Cr in between, is dense. However, subsequent layers of Ge, deposited on CaF_2, are not dense and mix with the sandwiching layers of CaF_2. The CaF_2 appears to form columns that do not provide adequate adhesions sites for the subsequently deposited Ge atoms. These columns of CaF_2 are evident in the bright field/dark field images in Figure 2.7. The dark field image also indicates further the mixing of CaF_2 and Ge as small crystallites of CaF_2 appear in the Ge layers.

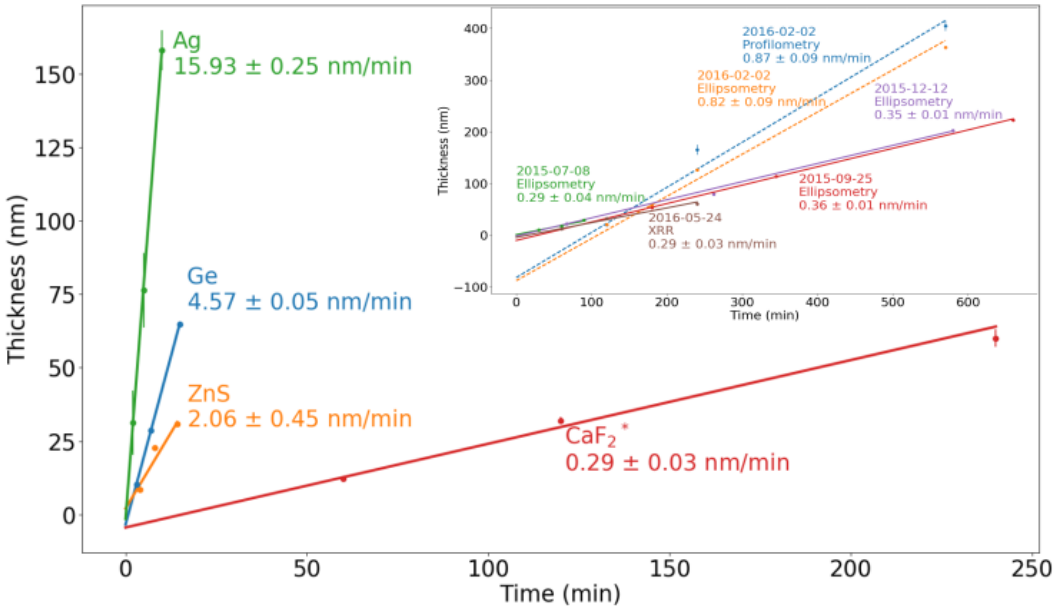

Figure 2.5: Deposition rates for all sputtered materials used in fabricating selective surface. ZnS was also used as a transparent dielectric. It was ultimately left out of the final surface fabricated by LGA Thin Films as sulfides generally contaminate physical deposition chambers quite severely. *The deposition rate for CaF_2 was taken from data collected on May 24th, 2016. Inset: Deposition rates for CaF_2 over the period of 10 months. The rates vary between 0.29 nm/min and 0.36 nm/min. For two data sets shown in dotted lines, there seems to be definitive nonlinear behavior, where the growth does not appear to begin for about 100 minutes. The variability in the growth rate forced us to find alternative deposition techniques other than sputtering.

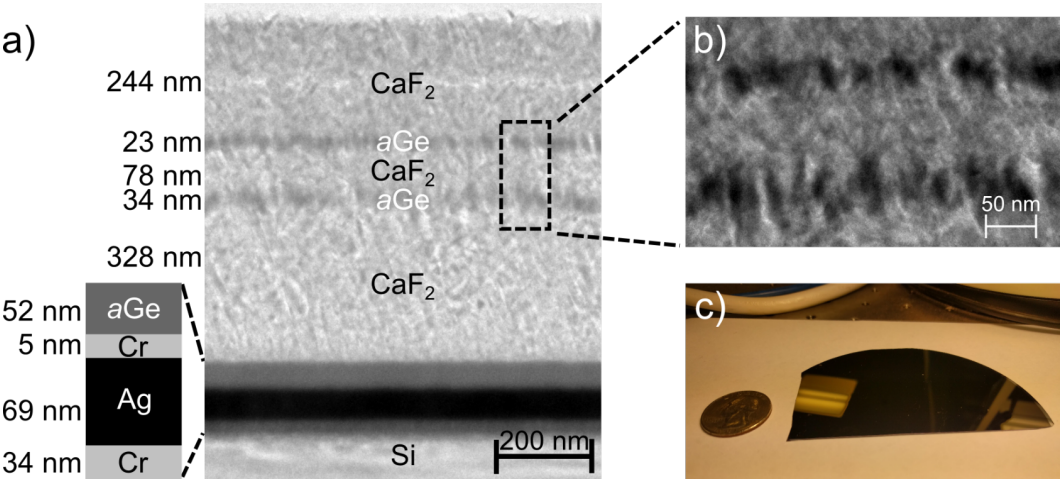

Figure 2.6: (a) Cross section transmission electron micrograph with layers and thicknesses labeled. (b) Zoomed in image of CaF_2 columns (grey) protruding through Ge layers (black). (c) Wafer fragment of surface next to U.S. quarter for size.

2.5 Characterization of Optical Properties

As the Ge layers are not pure but a mixture, they do not exhibit the same optical properties as would a dense layer of *a*Ge. As a result, the simulated and measured reflectance spectra are quite different, as shown in Figure 2.8. Instead, the effective refractive index of the Ge layers that are deposited on the CaF_2 layers is that of a *a*Ge-CaF_2 mixture. The refractive index n_{eff} of those layers is modeled as

$$n_{eff} = n_{aGe}x + n_{CaF_2}(1 - x), \tag{2.19}$$

where x is the percentage composition of *a*Ge. By comparing the theoretical prediction to the measured, we find the simulated reflectance spectrum with those layers comprising 50% *a*Ge and 50% CaF_2 to agree well with the measured result. We attribute further small discrepancies between simulation and experiment to surface defects and layer inhomogeneities that scatter incident light. As a result, subsequent optimization of layer thicknesses assumed layers of Ge deposited onto CaF_2 would have an effective refractive index of the 50%-50% mixture.

The final design of the selective surface accounted for this mixing, but the refractive index of the initial *a*Ge layer was still that of pure amorphous Ge. The deposition rate of CaF_2 was also recalibrated to correct for the discrepancy in thickness between the fabricated surface and the design. A wafer fragment of the final selective absorber is shown in Figure 2.6c.

We measured the room temperature spectral reflectance of the sample using UV-Vis spectroscopy and Fourier-Transform Infrared Spectroscopy (FTIR), as shown in Figure 2.9a. Under real-world conditions, incident sunlight is typically close to normally incident, and the spectra in Figure 2.9a can be used reliably to determine average solar absorptance. The solar absorptance before exposure to the sun obtained from this measurement is 76%. This value is lower than that of the simulated design due to discrepancies in the actual and targeted thicknesses of the individual layers. Although lower than that of other reported selective surfaces, the solar absorptance can be improved by straightforward optimization of the deposition process.

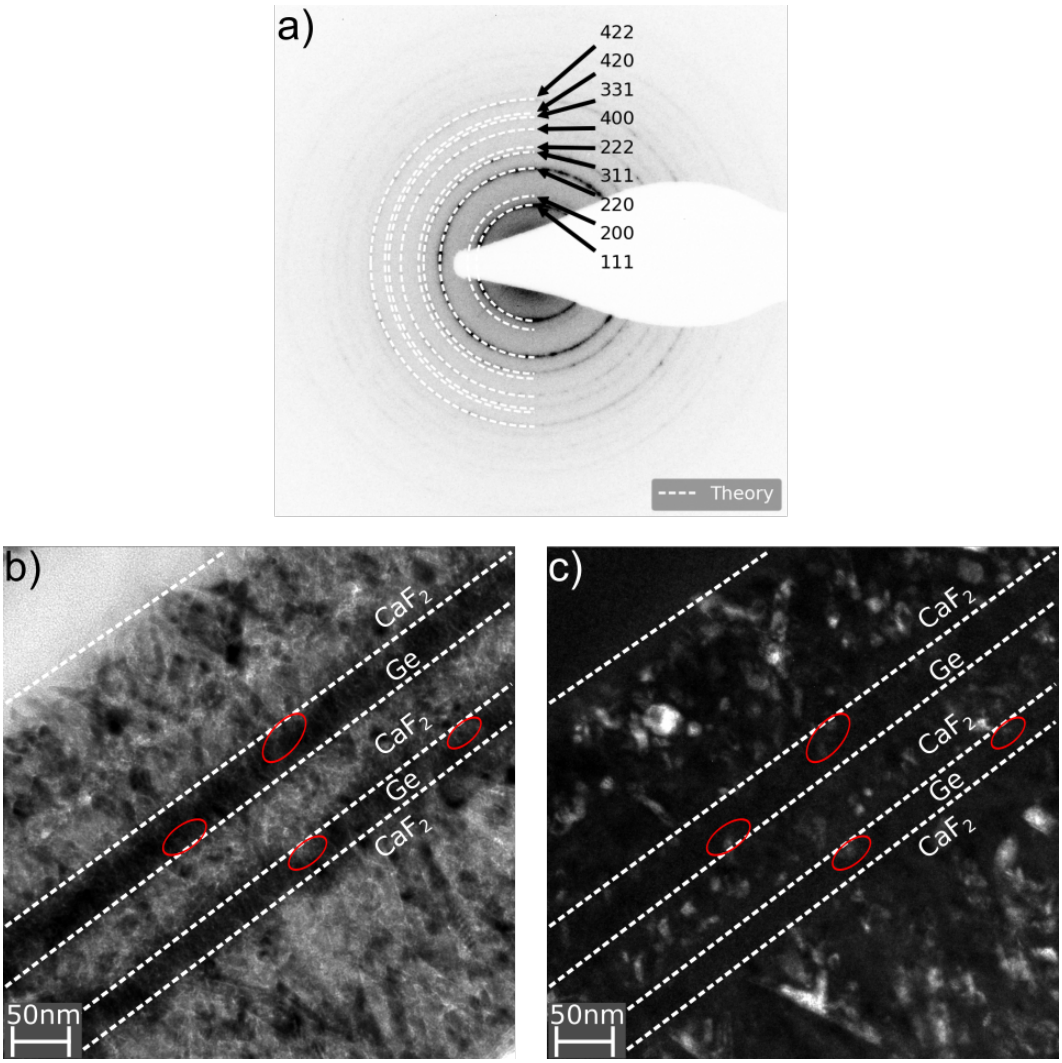

Figure 2.7: (a)TEM diffraction pattern of selective surface. The Laue rings from the CaF_2 are quite clear with the theoretical rings plotted in white for the corresponding reflection planes. (b) Bright Field image of CaF_2 and Ge layers. The columnar like structures in the CaF_2 layers are evident, particularly in the lower right hand corner of the imarge. Also clear, are smaller "whisker" like features of the CaF_2 poking into the black Ge layers. (c) Dark Field image of the same structure as in (b) focusing along the 111 axis. The crystallites show up in the CaF_2 layer providing more evidence that the CaF_2 is polycrystalline. Furthermore, the dark spots in the CaF_2 layers are not Ge contaminates, but are in fact CaF_2 crystallites. There is further evidence that CaF_2 is protruding into the Ge layers, as some faint patches are showing up in the dark field image, shown in red.

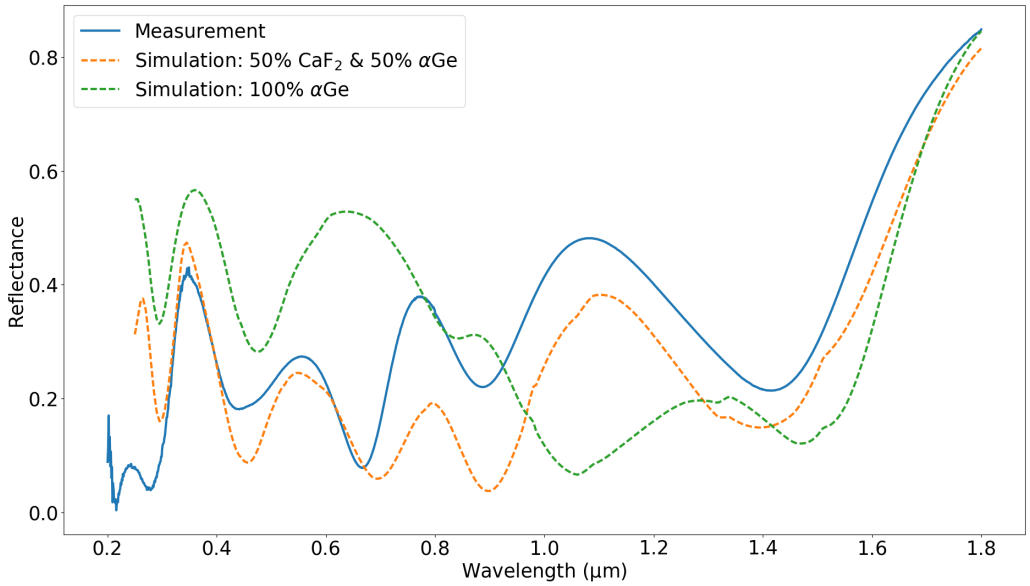

Figure 2.8: Measured and simulated reflectance spectra. Using the thicknesses measured in Figure 2.6a, we simulate the reflectance spectra for different compositions of aGe-Ca_2 mixtures in the aGe* layers.

The infrared reflectance spectra were also measured at temperatures up to 300 °C in dry air, as shown in Figure 2.9b. The spectra were taken with a confocal microscope and an HgCdTe (MCT) detector, while the samples were heated on a Linkham FTIR 600 temperature stage with a KBr window. Because of the added KBr window, we found the temperature dependent FTIR spectra depended sensitively on the microscope focus, and the uncertainty of these measurements was 5% absolute. As a result, there are regions in the IR where the high IR reflectance is shown to exceed unity but by no more than 5%. We still use these measurements to determine trends in thermal stability. As the temperature increases, the dip in reflectance at 3 μm becomes less pronounced and is stable from 100 °C to 200 °C. At 300 °C, as indicated by the red curve in Figure 2.9b, the reflectance dip at 3 μm begins to decrease again. Interestingly, the temperature cycling seems to initially cause a beneficial increase in IR reflectance. As water is absorptive at 3 μm and these samples were stored in air, a layer of water had likely adsorbed to the surface and evaporated after heating above 100 °C, causing the reflectance to increase [81]. Hence, the room temperature FTIR spectra shown in Figure 2.9a of samples with the adsorbed water layer indicate a *lower* infrared reflectance than is actually the case. In general, the reflectance drops as temperature increases, as expected, however the total absolute change is about 5% at 300 °C.

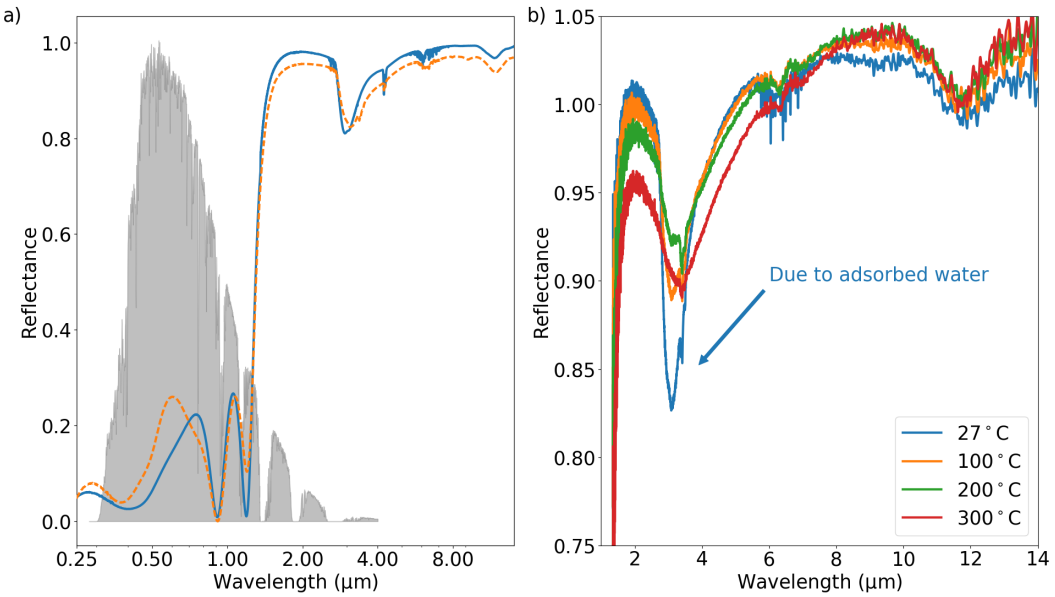

Figure 2.9: (a) Measured reflectance of sample versus wavelength before and after 4 temperature cycles under the sun and 2 cycles under an AM1.5G solar simulator. The solar spectrum, shown in gray, ranges from 0.28 μm to 2.5 μm, and thermal wavelengths extend beyond 3μm. Only slight changes in the optical properties are observed after multiple cycles. (b) Infrared reflectance versus wavelength at various temperatures. The sharp dip in reflectance at room temperature is primarily due to adsorbed water on the sample surface that evaporates at elevated temperatures. The reflectance exceeds unity due to an absolute uncertainty in the measurement of around 5%.

Determining the hemispherical total thermal emittance requires infrared reflectance measurements over all angles and wavelengths. As these measurements are challenging using readily available equipment, the effectiveness of selective surfaces has been traditionally quantified by a single absorptance or reflectance spectrum, taken at room temperature. A recent work reported a procedure to obtain measurements of average solar absorptance and hemispherical thermal emittance of solar absorbers at operating temperatures [82]. Rather than performing this measurement, we instead determined device performance by measuring the stagnation temperature under solar insolation in field tests in Pasadena, CA. We placed the sample in a 11" $\times$ 11" vacuum chamber with a glass lid that was in turn placed outside and angled toward the sun, as shown in Figures 2.10a-b. We adjusted the angle to $\sim 55^{\circ}$ such that the absorber sample was normal to the incoming sunlight. The sample temperature was measured with a type-K thermocouple secured to the surface initially with either Kapton tape or thermal epoxy. A second thermocouple was also taped to the cham-

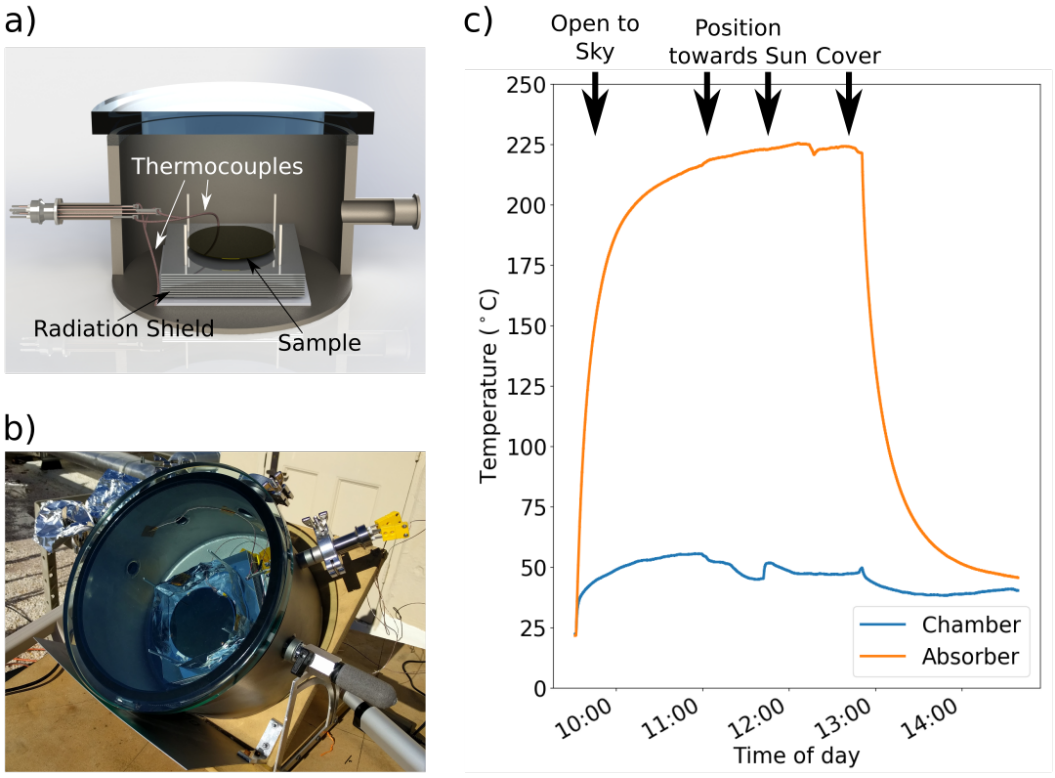

Figure 2.10: (a) Diagram of sample vacuum chamber and radiation shield. (b) Photo of vacuum chamber on the roof under solar insoluation. (c) Sample surface temperature over the course of the day on Dec. 20, 2016 in Pasadena, CA. The temperature peaked at 225 °C.

ber wall to determine the local temperature of the heat sink. We limited conductive and radiative heat losses by supporting the sample using low thermal conductivity aerogel foam on a radiation shield. The radiation shield was composed of 10 dual-sided aluminum mirrors separated by low thermal conductivity ceramic washers. The vacuum chamber was pumped continuously to eliminate convective losses and air conductive losses. The chamber was initially pumped to below 1×10^{-5} Torr, but as the chamber warmed in the sun, outgassing occurred, leading to a maximum pressure of around 1×10^{-4} Torr.

The chamber was positioned to face south and was first exposed to the sun around 9:30am to warm up. Around 11:00am and then again around 12:00pm, the chamber was positioned to face normal to the sun to maximize absorber temperature. At 1:00pm after the temperature had plateaued and reached its maximum, the chamber was covered. Measured on Dec. 20, 2016, the absorber temperature peaked at 225 °C.

We also measured the stagnation temperature under insolation from a AM1.5G solar simulator, under which the peak temperature reached 201.7 °C. Under the same conditions, a commercial state-of-the-art selective absorber reached a peak temperature of 223.1 °C, indicating that our unoptimized sample already achieved performance that is on par with state-of-the-art surfaces.

To determine sample stability, we repeated 6 temperature cycles (4 under the sun and 2 under the AM1.5G solar simulator) over the course of 20 days, and the surface temperature was measured to be 199 °C or higher in all cases. Shown in Figure 2.9a, the solar testing and consequent temperature cycling does cause noticeable changes in reflectance in the UV and in the IR, due to changes in layer morphology at high temperature. However, the *average* solar absorptance, calculated to be 74% after solar insolation, and the average thermal emittance are largely stable, which explains why real-world temperature performance over the 6 independent tests is consistent.

While the performance of our fabricated selective surface compares favorably with that of a state-of-the-art surface, our surface's stagnation temperature is still considerably below 350 °C, which we predicted from its simulated optical properties. To further understand the reason we look at the energy balance of the absorber under solar illumination. This model is then used to predict the stagnation temperature of the selective absorber assuming optimal conditions.

We begin by analyzing the radiative heat flux into the selective absorber from the sun and from the surrounding atmosphere,

$$\begin{aligned} q_{in} =& A\int_0^\infty \alpha(\lambda) I_{AM1.5}(\lambda) d\lambda \\ &+ A\int_0^\pi \int_0^{\pi/2} \int_0^\infty \alpha(\lambda,\theta,\phi) I_{BB}(\lambda, T_{atm}) \cos\theta \sin\theta d\lambda d\theta d\phi, \end{aligned} \tag{2.20}$$

where A is the absorber area, $\alpha(\lambda)$ is the spectral absorptance, $I_{AM1.5}(\lambda)$ is the solar spectral irradiance, and $I_{BB}(T_{atm}, \lambda)$ is the black body distribution at temperature of the atmosphere T_{atm}. The heat out of the selective surface is both radiative and conductive,

$$q_{out,rad} = A\int_0^\pi \int_0^{\pi/2} \int_0^\infty \alpha(\lambda,\theta,\phi) I_{BB}(\lambda, T_{absorber}) \cos\theta \sin\theta d\lambda d\theta d\phi, \tag{2.21}$$

$$q_{out,cond} = h_{loss}(T_{absorber} - T_{atm}), \tag{2.22}$$

where h_{loss} is the heat flux coefficient between the device and the environment. As the selective absorber is placed on a piece of aerogel foam, we anticipate h_{loss} to be

quite low. Further, as the sample is on a radiation shield, the emitted heat out the backside is negligible. The solar absorptance is defined as

$$\alpha_s = \frac{\int_0^\infty \alpha(\lambda) I_{AM1.5}(\lambda) d\lambda}{S}, \tag{2.23}$$

where S is the total heat flux from the sun. The thermal emittance weighted by the black body spectrum at temperature T is defined as

$$\epsilon_{t,T} = \frac{\int_0^\pi \int_0^{\pi/2} \int_0^\infty \alpha(\lambda, \theta, \phi) I_{BB}(\lambda, T) \cos\theta \sin\theta d\lambda d\theta d\phi}{\sigma T^4}, \tag{2.24}$$

where σ is the Stefan-Boltzmann constant. The net heat flux is therefore

$$\begin{aligned} q_{net} &= C\frac{dT}{dt} \\ &= \alpha_s AS - A\left(\epsilon_{t,T_{absorber}} \sigma T_{absorber}^4 - \epsilon_{t,T_{atm}} \sigma T_{atm}^4\right) - h_{loss}\left(T_{absorber} - T_{atm}\right), \end{aligned} \tag{2.25}$$

where C is the thermal capacitance of the absorber. The thermal capacitance is approximated as that of the silicon wafer such that $C = \rho V c_p$, where ρ is the density of silicon, V is the wafer volume, and c_p is the specific heat of silicon. We adopt the conventional methodology by approximating the second term on the right side of equation S7 as

$$A\left(\epsilon_{t,T_{absorber}} \sigma T_{absorber}^4 - \epsilon_{t,T_{atm}} \sigma T_{atm}^4\right) = A\epsilon_t \sigma\left(T_{absorber}^4 - T_{atm}^4\right), \tag{2.26}$$

where ϵ_t is an effective thermal emittance. In general, due to the wavelength selective nature of the absorber, $\epsilon_{t,T_{absorber}}$ does not equal $\epsilon_{t,T_{atm}}$. However as we are operating at moderate temperatures under unconcentrated sunlight, the difference between black body spectra at $T_{absorber}$ is not appreciably different than that at T_{atm} and $\epsilon_{t,T_{absorber}} \sim \epsilon_{t,T_{atm}}$. Therefore, we model the heat flux in and out of the absorber by

$$\frac{dT_{absorber}}{dt} = \frac{A}{\rho V c_p}\left[\alpha_s S - \epsilon_t \sigma\left(T_{absorber}^4 - T_{atm}^4\right) - G\left(T_{absorber} - T_{atm}\right)\right], \tag{2.27}$$

where G is the interface conductance between the absorber and the environment.

The measured absorber and chamber temperatures over time under illumination from the solar simulator are shown in Figure 2.11a. We first examine the part of

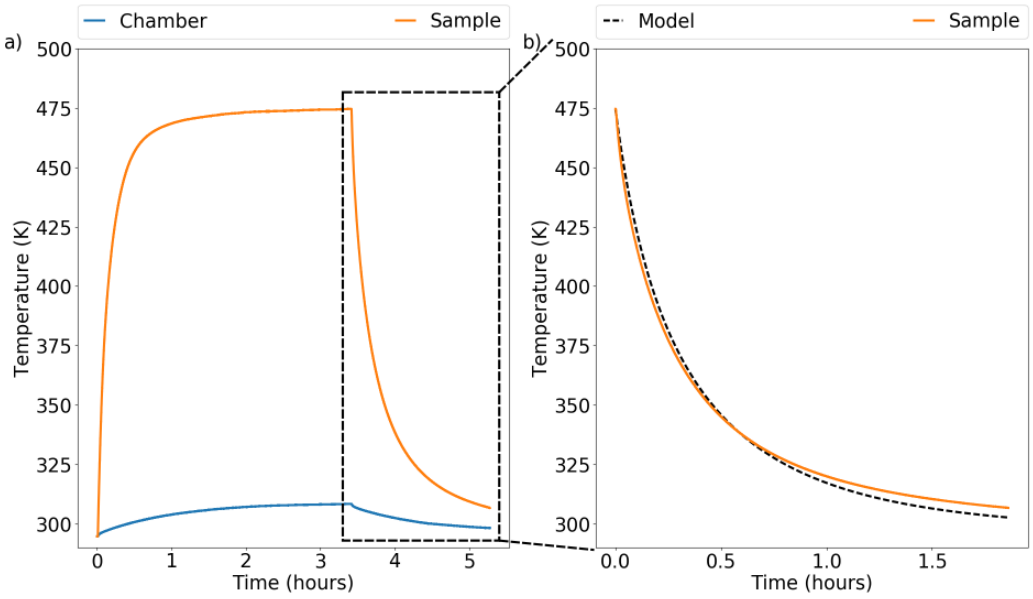

Figure 2.11: (a) Temperature data from solar simulator. (b)Measured and modeled temperature decay of sample after the chamber has been covered.

the curve after the sample has been covered and the surface is allowed to thermally decay. In this case, we set $S = 0$ in Equation S9. We then perform a numerical parametric fit for ϵ_t and G for the temperature solution of the differential equation,

$$\frac{dT_{absorber}}{dt} = \frac{A}{\rho V c_p}\left[-\epsilon_t \sigma \left(T_{absorber}^4 - T_{atm}^4\right) - G\left(T_{absorber} - T_{atm}\right)\right], \qquad (2.28)$$

where T_{atm} is fitted as a spline function to the chamber temperature data. From the parametric fit, we find $\epsilon_t = 0.128$, and $G = 2.809\times10^{-6}$ W/m^{2}K. The hemispherically averaged thermal emittance at operational temperatures is therefore approximately 13%, as opposed to ~5% as indicated by the FTIR spectra taken at a single angle, shown in Figure 2.9. The value for G does validate our initial assumption that the conductive heat loss would be negligible. The measured and modeled temperature decay are shown in Figure 2.11b. The marginal discrepancy between the fit and measured data is likely due to the slight temperature dependence of the thermal emittance.

We then use these fitted values to predict the temperature decay for the field test experiment, taken under the sun. The result is shown in Figure 2.12a. Having validated the model, we calibrate the incident solar flux such that at thermal equilibrium $T_{absorber}$ equals the maximum measured temperature. As a result of this calibration, we find that the solar flux into the absorber is 54% of the expected value. Using a simple Si photodiode, we determined that the transmissivity through the glass cover

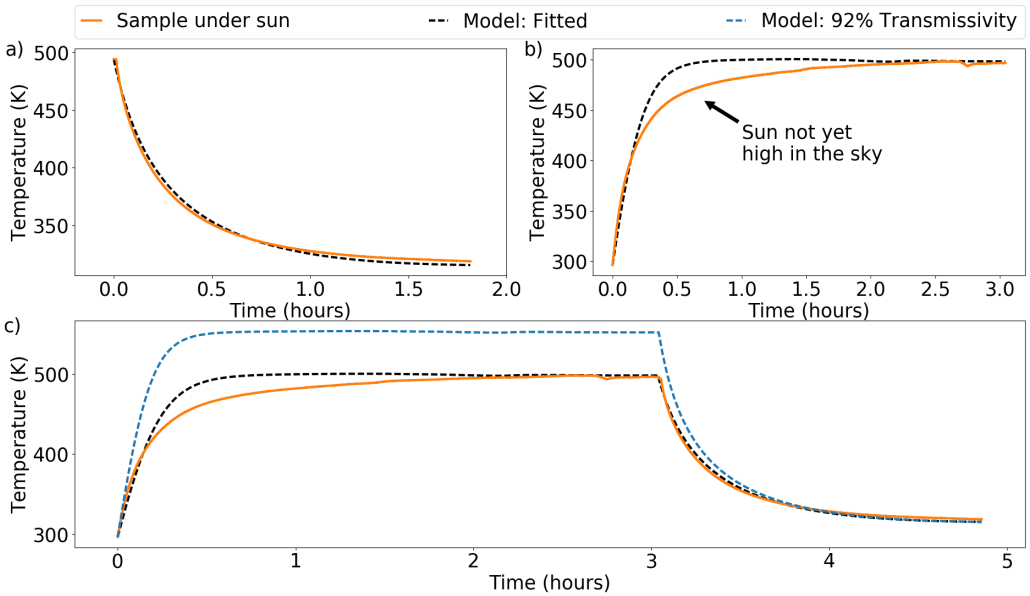

Figure 2.12: (a) Measured (solid yellow line) and predicted (dotted black line) temperature decay of sample under the sun, using the fitted values for ϵ_t and G from Figure 2.11b. (b) Temperature growth curves for sample (solid yellow line) and model (dotted black line). The fitted solar irradiance S indicates that the glass transmissivity is ~54%, assuming DNI of 900 Wm^{-2}. (c) Full modeled temperature rise under the sun. With a 92% transmissive window and $\alpha_{s,opt} = 0.76$ and $\epsilon_{t,opt} = 0.13$ (dotted blue line), we predict the peak temperature to reach 553 K or 280 °C.

of the vacuum chamber is in fact 56%. Hence, even though the glass cover appears to be perfectly transparent to the eye, as evidenced in Figure 2.10b, we are in fact losing nearly half of the sunlight. The simulated temperature rise compared to the measured result is shown in Figure 2.12b. The simulated temperature rises faster than the measured result because the measurement begins at 9:30AM, when the sun is not high in the sky, and the solar flux is not at its maximum.

The final simulation results are shown in Figure 2.12c, where the predicted surface temperature is plotted in blue, given a standard 92% tranmissive chamber window. The maximum steady-state temperature is 553 K or 280 °C. Given the demonstrated stability of the infrared reflectance, we would expect to reach this temperature given a high quality glass window. With further optimization of material quality to reduce parasitic infrared absorption, further increase of the stagnation temperature to above 300 °C could be achieved.

2.6 Conclusion

To further improve performance, primarily by improving solar absorptance, optimization of porosity and layer thickness of the CaF_2 films is necessary. It has been shown that thermally evaporated CaF_2 films can be grown for optical coatings with high precision [83]. Moreover, ion-assisted deposition of CaF_2 has been shown to produce layers of smooth, dense films with the refractive index of bulk CaF_2, necessary for designing absorbers with predictable optical properties [84]. By optimizing these two factors and incorporating higher quality glass in our chamber design, we predict our surface should achieve a stagnation temperature exceeding 300 °C, with a solar absorptance of around 85%. Such a solar absorptance would be competitive with existing selective surfaces, while the low thermal emittance of our surface would lead to a substantially improved stagnation temperature that would allow unconcentrated sunlight to be used for mid-temperature applications that are presently only achievable using geometric concentrators [23]. In addition, our selective absorber could significantly decrease the area required for rooftop solar thermal systems, thereby facilitating their adoption.

In summary, we have designed and fabricated a semiconductor based selective solar absorber that exploits the sharp absorption transition of semiconductors at the band gap energy to achieve high visible absorption yet low infrared emission. In field tests we obtain peak temperatures consistently exceeding 200 °C, a value comparable to the performance of state-of-the-art surfaces. Straightforward optimization of layer thicknesses and deposition conditions indicate the peak temperature could be increased to 300 °C. Semiconductor-dielectric based selective surfaces can play an important role in expanding the application of unconcentrated solar thermal systems for mid-temperature applications.

Chapter 3

RADIATIVE HEAT FLUX MODULATION IN THE THERMAL NEAR FIELD

This chapter has been adapted in part from:

Nathan H. Thomas, Michelle C. Sherrott, Jeremy Broulliet, Harry A. Atwater, and Austin J. Minnich. Electronic Modulation of Near Field Radiative Transfer in Graphene Field Effect Heterostructures. *In preparation*, 2019

3.1 Introduction

Radiative heat transfer between two bodies in the far field is bounded by the Stefan-Boltzman relation of $Q <= \sigma(T_1^4 - T_2^4)$, often referred to as the *blackbody limit*. In the near field, where the length scale between radiating objects is on the order of the wavelength of heat carrying optical modes, evanescent modes can couple from one body to the next, thereby enhancing heat transport. This phenomenon is most readily seen in systems that support evanescent surface waves [37], which do not carry any radiative power in the far-field but can transport energy in the near field.

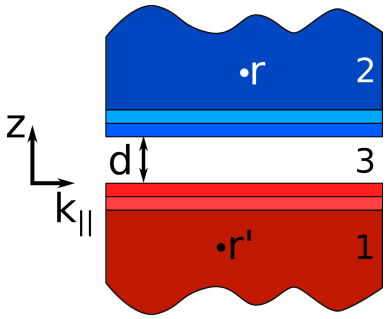

Figure 3.1: Diagram of two layered half-spaces. Media 1 and 2 are two different layered systems, and medium 3 is vacuum.

In this thesis, the focus is on planar, layered structures as diagrammed in Figure 3.1, which is a simple geometry that allows for an analytic expression for the heat flux from body 1 to body 2, first developed by Polder and van Hove in 1971 [86]. The full derivation is laid out in Appendix B, but a cursory introduction is given

here. The basic approach employs the fluctuation dissipation theorem, developed for electrodynamics by S.M. Rytov in 1953 [87, 88], which relates the fluctuations of current densities j to the local temperature T and the material permittivity ϵ:

$$\langle j_\alpha(\boldsymbol{r},\omega) j_\beta(\boldsymbol{r'},\omega)\rangle = \epsilon_0 \omega \frac{\Im(\epsilon)}{\pi} \Theta(\omega,T)\delta(\boldsymbol{r}-\boldsymbol{r'})\delta_{\alpha\beta}. \tag{3.1}$$

As we are only concerned with non-magnetic materials, these are electric current densities, but this expression also holds for magnetic ones. The heat flux from body 1 into body 2 is the z-component of the Poynting vector at $\boldsymbol{r}$ due to a source charge at $\boldsymbol{r'}$. We calculate the Poynting vector

$$\langle \boldsymbol{S}(\omega)\rangle \cdot \hat{z} = \frac{1}{2}\Re\left(\langle \boldsymbol{E}(\boldsymbol{r},\omega) \times \boldsymbol{H}(\boldsymbol{r},\omega)\rangle\right) \cdot \hat{z} \tag{3.2}$$

from the electric and magnetic fields, which are in turn related to the current densities by their respective dyadic Green functions $\overleftrightarrow{\boldsymbol{G}}$:

$$\boldsymbol{E}(\boldsymbol{r},\omega) = \int_V d^3r' i\omega\mu_0 \overleftrightarrow{\boldsymbol{G}}_E(\boldsymbol{r},\boldsymbol{r'},\omega)\boldsymbol{j}(\boldsymbol{r'},\omega) \tag{3.3}$$

$$\boldsymbol{H}(\boldsymbol{r},\omega) = \int_V d^3r' \overleftrightarrow{\boldsymbol{G}}_H(\boldsymbol{r},\boldsymbol{r'},\omega)\boldsymbol{j}(\boldsymbol{r'},\omega). \tag{3.4}$$

The total heat flow from body 1 to body 2 is

$$\langle S_{z1\to2}\rangle = \int_{V_1} d^3r' \int_{V_1} d^3r'' \left(G^E_{xk}G^{H*}_{yl} - G^E_{yk}G^{H*}_{xl}\right)\langle j_k(\boldsymbol{r'}\omega) j_l(\boldsymbol{r''}\omega)\rangle. \tag{3.5}$$

After plugging in the fluctuation dissipation theorem Eq 3.1 into Eq. 3.5, we only need the expressions for the Green functions to compute the heat flux. These are given explicitly in Appendix B, but the end result for the spectral heat flux as a function of frequency $H(\omega, T_1, T_2)$ is

$$H(\omega,T_1,T_2) = \Phi(\omega)\left(\Theta(\omega,T_1) - \Theta(\omega,T_2)\right), \tag{3.6}$$

where $\Phi(\omega)$ is the transmissivity function, partitioned over propagating modes where $k_{||} < \omega/c$, and evanescent modes where $k_{||} > \omega/c$ [86, 89],

$$\begin{aligned}\Phi(\omega) = &\sum_{s,p}\int_0^{\omega/c} dk_{||}\frac{k_{||}}{2\pi}\frac{(1-|r^{s,p}_{13}|^2)(1-|r^{s,p}_{23}|^2)}{|1-r^{s,p}_{13}r^{s,p}_{23}e^{i2k_{z0}d}|^2} \\ &+ \int_{\omega/c}^{\infty} dk_{||}\frac{k_{||}}{2\pi}\frac{4\Im(r^{s,p}_{13})\Im(r^{s,p}_{23})}{|1-r^{s,p}_{13}r^{s,p}_{23}e^{-2|k_{z0}|d}|^2},\end{aligned} \tag{3.7}$$

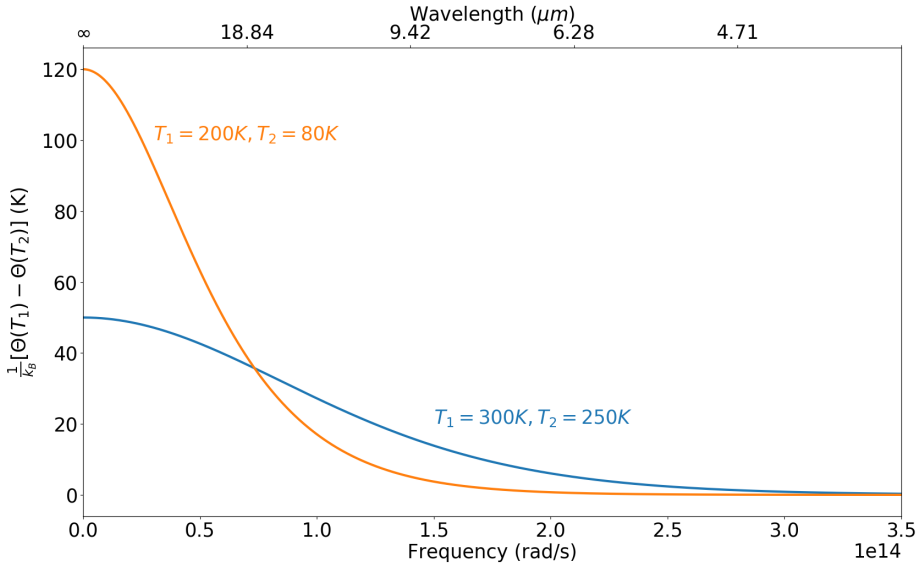

Figure 3.2: Thermal envelope function. Lower frequency modes carry more heat than those at higher frequencies.

where r_{13} and r_{23} are the Fresnel reflection coefficients from halfspace 1 into vacuum and halfspace 2 into vacuum, respectively. To get the total heat flux, we integrate $H(\omega, T_1, T_2)$ over all frequencies such that

$$Q(T_1, T_2) = \int_0^\infty \frac{d\omega}{2\pi} H(\omega, T_1, T_2). \tag{3.8}$$

The difference in the energy distributions $\Theta(\omega, T_1) - \Theta(\omega, T_2)$ in Eq. 3.6, acts as an envelope function that modifies the spectral transmissivity $\Phi(\omega)$. Shown in Figure 3.2, this envelope function approaches $k_B(T_1 - T_2)$ as $\omega \to 0$ and monotonically decays to 0 as $\omega \to \infty$. There are two important conclusions to draw; lower frequency modes convey more heat than high frequency modes and by changing *both* temperatures we can change by how much more. At the temperatures near room temperature or lower investigated in this thesis, the relevant frequencies for heat transport are in the mid to far infrared.

Another important result from this analysis is that the spectral transmissivity $\Phi(\omega)$ is dependent on the optical properties of the two half-spaces, manifest in the Fresnel reflection coefficients. By tuning the infrared optical properties appropriately, we may either enhance or reduce the total heat flow. In this chapter, we theoretically

motivate a way to demonstrate active modulation of heat flow for thermal switching applications, taking advantage of graphene's gate-tunable optical properties.

3.2 Graphene Based Radiation Modulation

Thermal switches that change thermal resistance in response to external stimuli have long been desired for applications [90]. Typical thermal switches used in practice operate by changing the physical contact of metallic leads or flow control of heat transfer fluids, both of which require mechanical parts prone to failure [91]. Numerous other schemes for controlling conductive heat flow have been proposed, including biasing of ferroelectrics [92–94], exploiting changes in properties across a phase transition [95–98], and magnetically aligning crystal networks [99]. Thermal switches for radiative transfer can be realized if the dielectric function or optical resonances at the surface of a solid can be altered by an external stimulus [61, 100–102]. In particular, theoretical and experimental works have described radiative heat flux modulation based on the insulator-metal transition of VO_2 [62, 63, 103].

Two-dimensional solids now offer a capability to alter the surface dielectric constant by electrostatic tuning of the free carrier concentration in a controllable and reversible manner and without requiring large temperature differentials [52, 104–109]. Despite this capability, achieving even modest modulation of far-field radiative flux is challenging as thermal radiation is broadband. In the near field, however, thermal radiation is primarily due to resonant coupling of evanescent surface modes, such as plasmons or phonon-polaritons [37, 110], which are narrowband and can be tuned by external stimuli. Additionally, the near field heat flux can be orders of magnitude larger than the far-field blackbody limit, and thus near field radiative heat transport has been an area of intense experimental [27–33, 38, 57, 58] and theoretical [36, 41, 45, 48, 111–115] interest.

Graphene has been proposed as an ideal material for thermal switching of near field radiation at room temperature as it exhibits a plasmonic resonance in the mid-infrared that can be electrostatically tuned [60, 116–118]. Recent experimental works have reported that graphene enables enhanced radiative thermal coupling between polar materials in the near field [59, 119]. However, these results do not take advantage of the tunability of graphene's plasmon resonance to modulate heat flow by electrostatic tuning. Recently, a theoretical scheme was proposed to electrostatically control radiative flow in a graphene field effect device [120], however the dielectric was SiC, which is not a typical gate dielectric for graphene

and is not considered here.

In this chapter, we first reproduce the initial findings on thermal switching with graphene laid out in Ilic, Thomas, et al. [118]. We then investigate four potential gate dielectrics for back gating of graphene field effect devices to determine the best candidate for experimental implementation. Finally, we make theoretical predictions for an experimentally realizable sample.

3.3 NFHT: Graphene Membranes

The results highlighted in this section are reproduced from Ilic, Thomas, et al. [118]. To begin with a simple case, we consider two suspended graphene membranes with identical, although still tunable Fermi levels, separated by a gap distance of 100 nm. The graphene is modeled as a conductive interface with a local optical conductivity $\sigma = \sigma^{intra} + \sigma^{inter}$ given by [121]

$$\begin{aligned} \sigma^{intra}(\omega) &= \frac{2ie^2 k_B T}{\pi\hbar(\omega + i\tau^{-1})} \log\left[2\cosh\left(\frac{\mu}{2k_B T}\right)\right] \\ \sigma^{inter}(\omega) &= \frac{e^2}{4\hbar}\left[G\left(\frac{\hbar\omega}{2}\right) + i\frac{4\hbar\omega}{\pi}\int_0^\infty \frac{G(\xi) - G\left(\frac{\hbar\omega}{2}\right)}{(\hbar\omega)^2 - 4\xi^2} d\xi\right], \end{aligned} \tag{3.9}$$

where

$$G(\xi) = \frac{\sinh\left(\frac{\xi}{k_B T}\right)}{\cosh\left(\frac{\mu}{k_B T}\right) + \left(\frac{\xi}{k_B T}\right)}. \tag{3.10}$$

The tunability of the optical properties is implicit in the dependence of the optical conductivity on the Fermi level μ. A critical factor in the optical conductivity is the scattering time τ, which relates to the carrier mobility m, $\tau = m\mu/v_F^2$. This scattering time is indicative of the quality of the graphene film. For the calculations in this thesis, $\tau = 50\times10^{-15} s$ unless otherwise stated, which reasonably corresponds to the quality of graphene films grown by chemical vapor deposition [122].

The Fresnel coefficients to plug into Equation 3.7 simplify to [123]

$$\begin{aligned} r_p &= \frac{\sigma k_{z0}}{2\omega\epsilon_0 + \sigma k_{z0}} \\ r_s &= \frac{\mu_0\sigma\omega}{2k_{z0} + \mu_0\sigma\omega}. \end{aligned} \tag{3.11}$$

To quantify thermal switchability, we define the thermal conductance, $h(T) = \lim_{T_1,T_2\to T} Q(T_1,T_2)/(T_1 - T_2) = \int_0^\infty \frac{d\omega}{2\pi}\frac{\partial\Theta(\omega,T)}{\partial T}\Phi(\omega)$ and the switching ratio $\eta =$

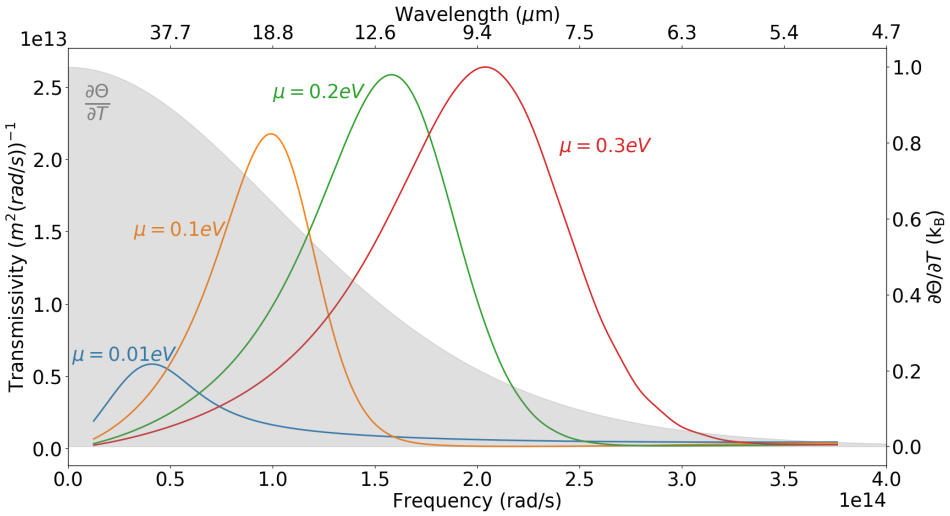

Figure 3.3: Spectral heat flux for graphene membranes at different Fermi levels for $T_1 = 277K$ and $T_2 = 77K$ at a vacuum gap distance of 100 nm. The envelope function for thermal conductance $\partial\Theta/\partial T$ is plotted in grey, which asymptotes to k_B at zero frequency.

h^{on}/h^{off}.

$$\begin{aligned} h^{on} &\equiv h(\mu_1^{on}, \mu_2^{on}) \\ h^{off} &\equiv h(\mu_1^{off}, \mu_2^{off}). \end{aligned} \tag{3.12}$$

The switching ratio acts as a figure of merit for how well the graphene membranes function as a switch, where the h is maximized in the "on-state" and minimized in the "off-state". The two components of h, the spectral transmissivity function $\Phi(\omega)$ and the new thermal envelope function $\partial\Theta/\partial T$, are shown in Figure 3.3. Being the derivative of the previous envelope function for the spectral heat flux, $\partial\Theta/\partial T$ approaches k_B at zero frequency and zero at $\omega \to \infty$.

To calculate the total thermal conductance, we integrate the transmissivity weighted by $\partial\Theta/\partial T$. In this case where the Fermi levels are kept the same, heat flux is maximized when they are ~0.2 eV and minimized when they are 0.01 eV. However, further optimization of the heat flux can be extended to cases when the Fermi levels of the top and bottom membranes are allowed to differ. Intuitively, such a configuration would allow for tuning of both Fermi levels, shifting the graphene

plasmons on and off resonance and either enhancing or reducing the total radiative heat flux.

We optimize η as function of four Fermi levels ($\mu_1^{on}, \mu_2^{on}, \mu_1^{off}, \mu_2^{off}$) using a derivative free search algorithm and the nonlinear optimization package NLopt [124, 125]. We limit the allowable Fermi levels to be between $\mu_{min} = 2k_BT \approx 0.05eV$ and $\mu_{max} = 0.6eV$. We set the lower limit in order satisfy the necessary conditions to assume the local behavior in the optical conductivity. The upper limit is largely set by what can be reasonably achieved by electrostatic gating.

The switching ratio optimization balances between three main frequency dependent factors that contribute to heat flow. First is the detuning of the plasmonic resonances. As shown in Figure 3.4, as the mobility gets larger, the plasmon resonances become sharper and the effect of detuning becomes more pronounced. Second, there is the thermal envelope $\partial\Theta/\partial T$ with the consequence that lower frequencies fundamentally carry more heat than higher ones. And finally, there is the local density of optical states (LDOS), which determines the density of modes that can contribute to heat flow. The LDOS shifts to higher frequencies and increases in magnitude with increasing Fermi level [126, 127].

The optimized switching ratio as a function of mobility for graphene membranes with a vacuum gap separation of 100 nm is shown in Figure 3.5b. There is a clear monotonic increase in switching ratio with mobility. The corresponding optimized Fermi levels are shown in Figure 3.5c. To maximize the heat flux, the Fermi levels exhibit a monotonic dependence *downwards* as mobility increases, which is due to the frequency dependence of the envelope function $\partial\Theta/\partial T$. As lower frequencies carry more heat, there is a bias for the on-state to operate through a lower frequency resonance or for the graphene membranes to have lower Fermi levels. As the mobility increases, the resonance narrows, suppressing the contribution of lower frequencies, driving the optimal Fermi levels lower. The off-state exhibits the opposite trend for the lower Fermi level. The higher Fermi level μ_2^{off} simply remains constant at μ_{max}. For the lower Fermi level μ_1^{off}, when the resonances are narrow ($m > 2000$ cm^{2}V^{-1}s^{-1}), beyond a certain threshold, the resonances are adequately offset such that no further heat flux suppression is obtained by going to yet lower Fermi levels. Instead, going to lower Fermi levels allows for the onset of interband optical transitions that contribute to added heat flow. As a result, the lower off-state Fermi level increases with mobility beyond $m > 2000$ cm^{2}V^{-1}s^{-1}.

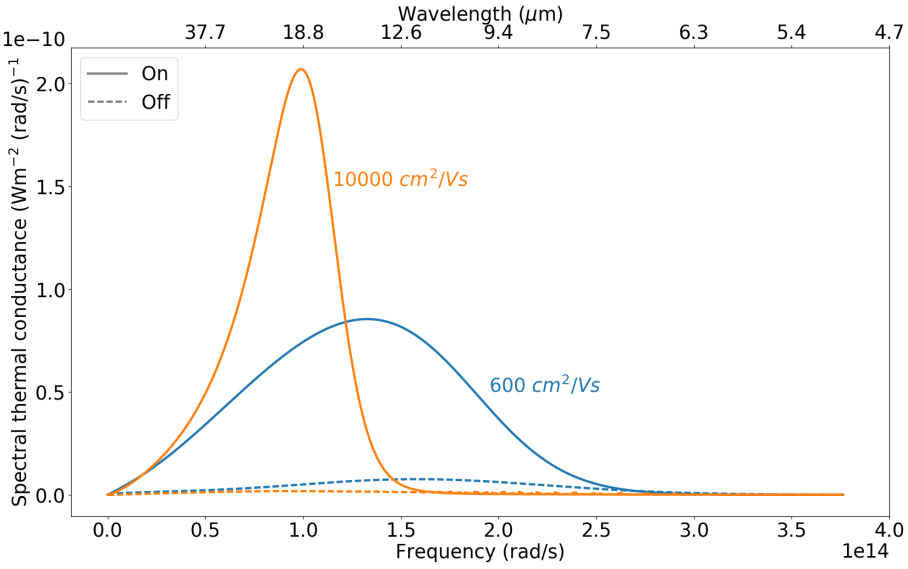

Figure 3.4: Spectral thermal conductance at mobility $m = 600$ cm^{2}V^{-1}s^{-1} and $m = 10000$ cm^{2}V^{-1}s^{-1}. At higher mobility the plasmon resonance and therefore spectral conductance is narrower.

Along with the graphene mobility, we also investigate the dependence of the vacuum gap spacing on the switching ratio for a fixed mobility of 2000 cm^{2}V^{-1}s^{-1}, shown in Figure 3.6a. There is a clear monotonic decrease in the switching ratio as the gap distance increases. The corresponding optimal Fermi levels for the on- and off-states are shown in Figure 3.6b. Interestingly, for gap distances larger than 600 nm, the off-state is bimodal, where the Fermi levels can both be minimized to μ_{min}, or they can be maximily detuned such that one Fermi level is μ_{min} and the other is μ_{max}, as indicated in Figure 3.6b. The density of states at such distances is low enough at low Fermi levels, that the overlap in the plasmon resonances is not consequential. The effect of detuning is similar in effect to operating with a lower density of heat carrying optical modes. For the on-state, as the gap distance increases, so too do the optimized Fermi levels, since the added benefit from the higher density of states outweighs the bias towards lower Fermi levels from $\partial\Theta/\partial T$.

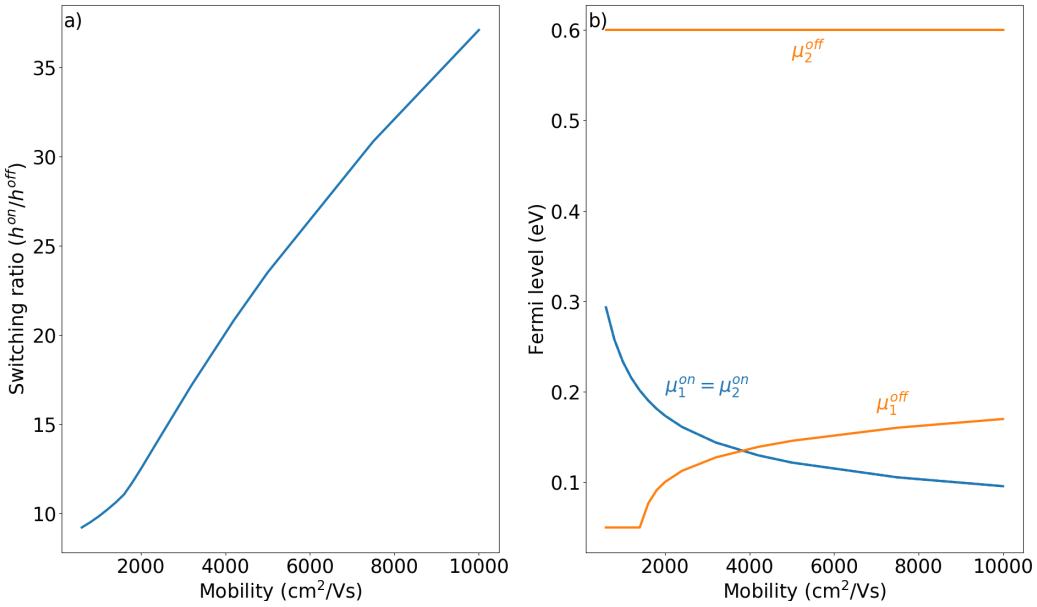

Figure 3.5: (a) Switching ratio and (b) corresponding Fermi levels as a function of mobility at a vacuum gap distance of 100 nm.

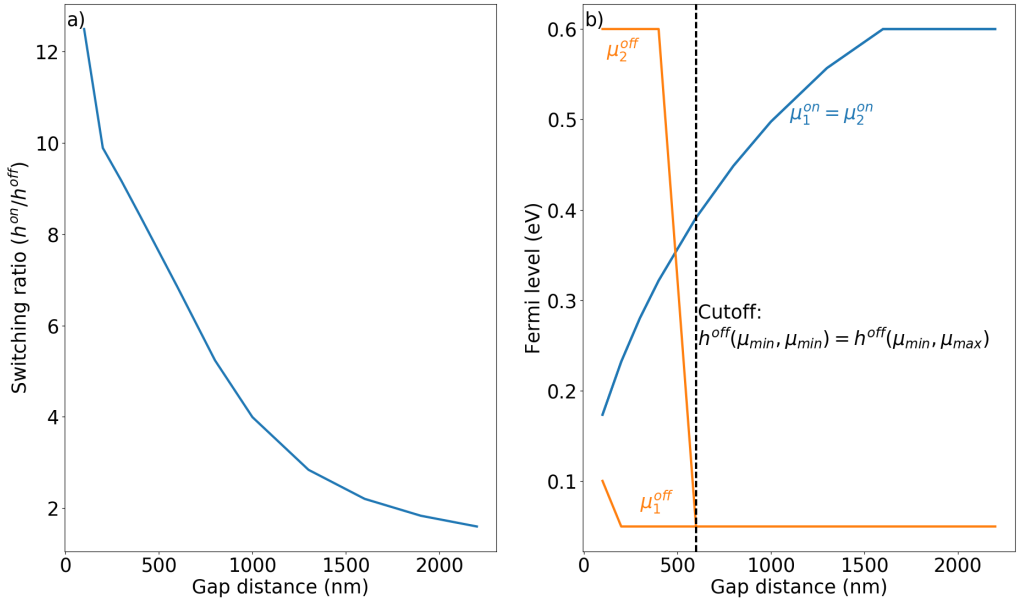

Figure 3.6: (a) Switching ratio dependence on gap distance for mobility $m = 2000$ cm^{2}V^{-1}s^{-1}. There is a strong monotonic trend downwards with vacuum gap. (b) Corresponding optimal Fermi levels. After a cutoff distance of 600 nm the off-state becomes bimodal, where the the Fermi levels can either be maximally detuned or both minimized to μ_{min}.

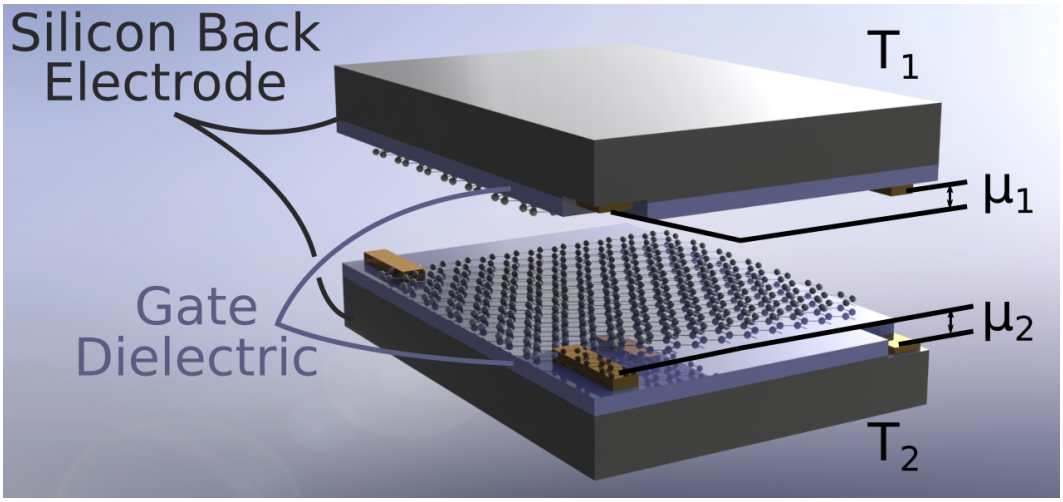

Figure 3.7: Diagram of back-gated system

3.4 NFHT in a Realistic Configuration: Back-Gated Graphene

Although this analysis provides insights for the mechanisms behind modulating radiative heat flux with graphene, this configuration of graphene membranes is not currently experimentally realizable. In this section, we extend the analysis from the previous section to graphene based, back-gated field effect devices. A basic diagram of the system configuration is shown in Figure 3.7, where the top and bottom samples are identical with a gate dielectric of thickness d and a silicon back electrode. Although there are countless configurations of dielectrics and electrodes that allow for modulation of the graphene Fermi level by elecrostatic back gating, we select for readily commercially available silicon substrates and four standard high k dielectrics that are typically used in graphene devices: Al_2O_3, HfO_2, SiN_x, and SiO_2. As in Section 3.3, the Fermi levels of the top and bottoms samples, μ_1 and μ_2 respectively, can be modified by an external bias.

We recreate the previous study in looking at optimal Fermi levels to maximize the switching ratio at different vacuum gap spacings but also at different dielectric thicknesses. Instead of also varying mobility, we pick a single carrier scattering time of $\tau = 50 \times 10^{-15} s$.

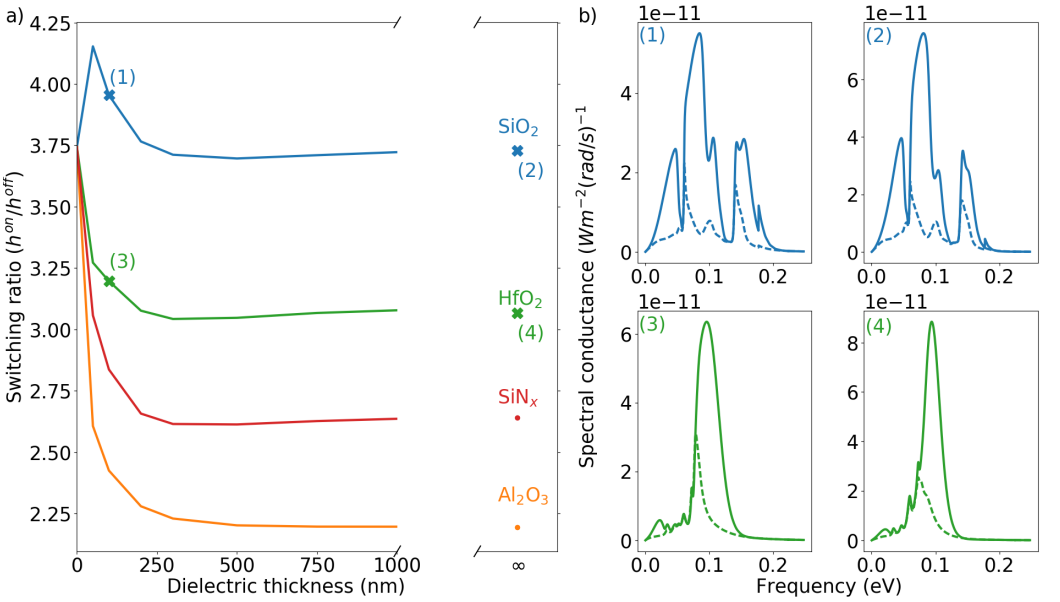

Figure 3.8: (a) Switching ratio vs dielectric thickness at vacuum gap = 100 nm. (b) Spectral heat flux at 50 nm thick dielectric films (1 and 3) and infinitely thick dielectric films (2 and 4) for SiO_2 (blue) and HfO_2 (green). At this small vacuum gap spacing fo 100 nm, the hybridized mode of the plasmon and phonon-polariton, which can be tuned with Fermi level, is the dominant radiative thermal pathway. There is little difference in the spectral heat flux with thin (50 nm) and infinitely thick dielectric layers.

The outcome of these calculations is shown in Figures 3.8, 3.9, and 3.10, where in each plot, the switching ratio dependence on dielectric thickness is plotted on the left, and the spectral thermal conductance for two different layer thicknesses of SiO_2 and HfO_2 is plotted on the right. In all cases, the thermal conductance values are plotted at the optimal Fermi levels. The main notable feature in these plots is that SiO_2 is the best dielectric for radiative thermal switching. Also, the trend in switching ratio versus dielectric thickness is opposite for low vacuum gaps $\leq$ 100 nm as opposed to high vacuum gaps $\geq$ 500 nm. For low vacuum gaps near 100 nm, the switching ratio drops and then flattens out to a steady-state value (except for the initial minor jump for SiO_2). For gap thicknesses 500 nm and greater, the switching ratio is either flat or increases with dielectric thickness.

The reason for this trend is largely because the silicon back electrode acts as a radiative thermal trap. The silicon is modeled as lossless with a zero frequency permittivity of $\epsilon = 3.4^2 = 11.56$. The evanescent plasmon and polariton modes

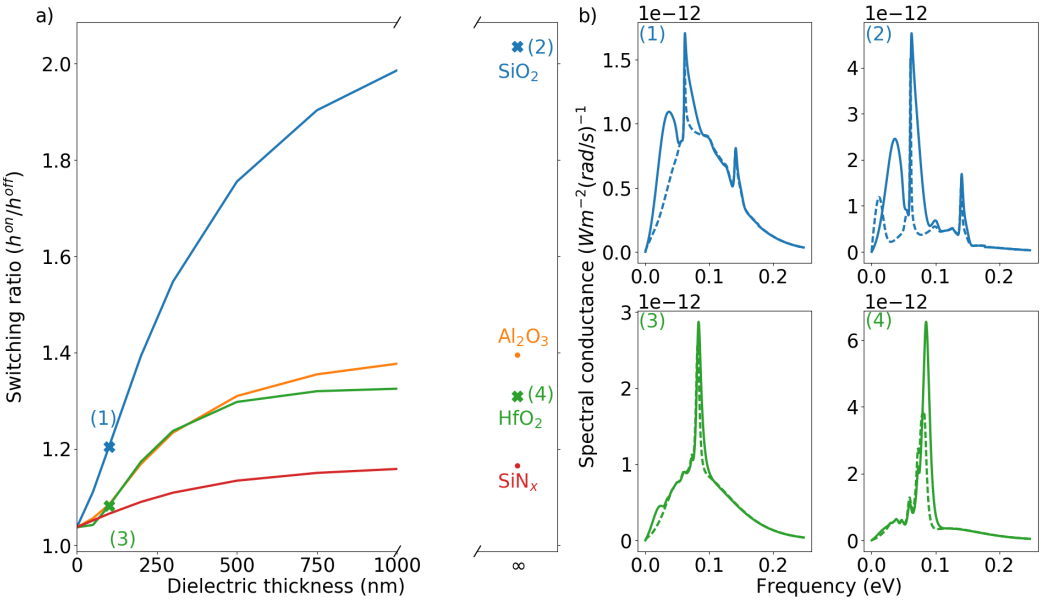

Figure 3.9: (a) Switching ratio vs dielectric thickness at vacuum gap = 500 nm. (b) Spectral heat flux at 50 nm thick dielectric films (1 and 3) and infinitely thick dielectric films (2 and 4) for SiO_2 (blue) and HfO_2 (green). The hybridized mode still contributes to tunable heat flow. However, at low dielectric thicknesses in (1) and (3), the background heat flux from the underlying silicon starts to dominate. At higher thickness in (2 and (4), this effect is less pronounced and the spectral features of the plasmon and dielectric phonon polaritons are evident.

that contribute to the radiative thermal coupling across the vacuum gap are largely trapped in the silicon and don't make it into the vacuum. This can be seen in the spectral thermal conductance plots in Figure 3.9b and 3.10b, where the narrow band spectral features like the graphene plasmon and the dielectric phonon polaritons contribute comparatively less to heat flow than the broadband, "baseline" contribution from the featureless silicon.

The influence of the silicon is much less important at small gap spacings $\leq$ 100 nm where the evanencent modes can still couple well to one another. The silicon simply lowers the radiative heat flux for the on-state and the off-state equally. As a result, at the smaller dielectric thickness of 50 nm where the silicon is closer to the graphene and more influential, the switching ratio is actually greatest. As the thickness of the dielectric layers increases, the silicon influence is less pronounced and the switching ratio flattens out. For larger vacuum gap distances, there is no such benefit to going to a thinner dielectric. Because of the large gap separation, the coupling between the graphene plasmons is reduced, and the further the silicon is from the graphene the better for thermal switching.

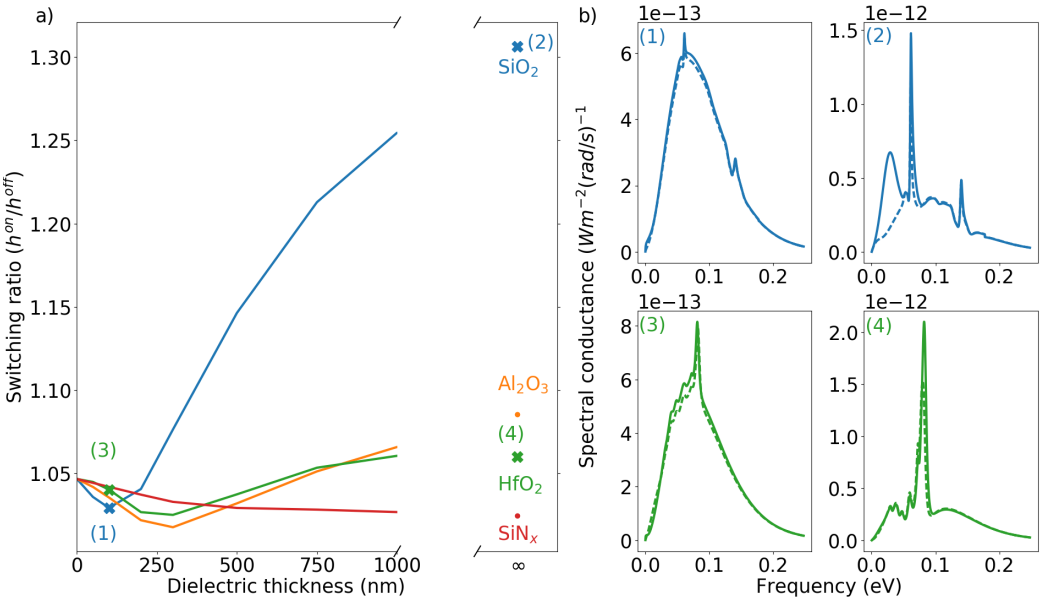

Figure 3.10: (a) Switching ratio vs dielectric thickness at vacuum gap = 1000 nm. (b) Spectral heat flux at 50 nm thick dielectric films (1 and 3) and infinitely thick dielectric films (2 and 4) for SiO_2 (blue) and HfO_2 (green). At large dielectric thicknesses, particularly for HfO_2 in (4), the heat flux is dominated by the non-tunable phonon polariton. However, for SiO_2 which has lower permittivity than HfO_2, at infinite thickness the graphene plasmon at ~0.06 eV still contributes to heat flux that can be modulated. At vacuum gap distances this large, the background heat flux from the dielectric and the silicon both dominate heat flux.

The dielectric constant is also important for comparing the dielectrics to one another. The real and imaginary parts of the complex permittivity for each dielectric are taken from [128–132] and are plotted in Figure 3.11. Just like the high dielectric constant in silicon can cause the evanescent surface modes to be localized within the substrate, so too does the real part of the permittivity for each dielectric. SiO_2 functions better than the other compounds for thermal switching particularly at large gap distances because its permittivity is so much lower at low frequencies where the graphene plasmon is pronounced.

In all cases, however, the dielectric negatively influences the switching ratio when compared to the simple graphene membrane case. The phonon polariton modes from the dielectrics allow for enhanced radiatively coupling between the top and the bottom samples, even in the "off" state. This enhanced coupling is a loss pathway

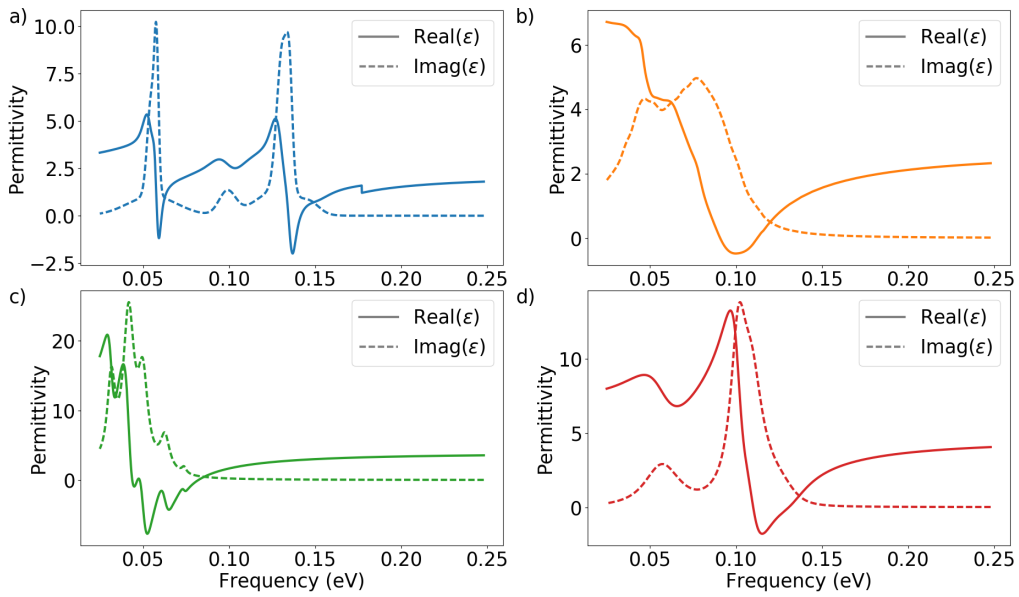

Figure 3.11: Permittivities for (a) SiO_2, (b) SiN_x, (c) HfO_2, and (d) Al_2O_3.

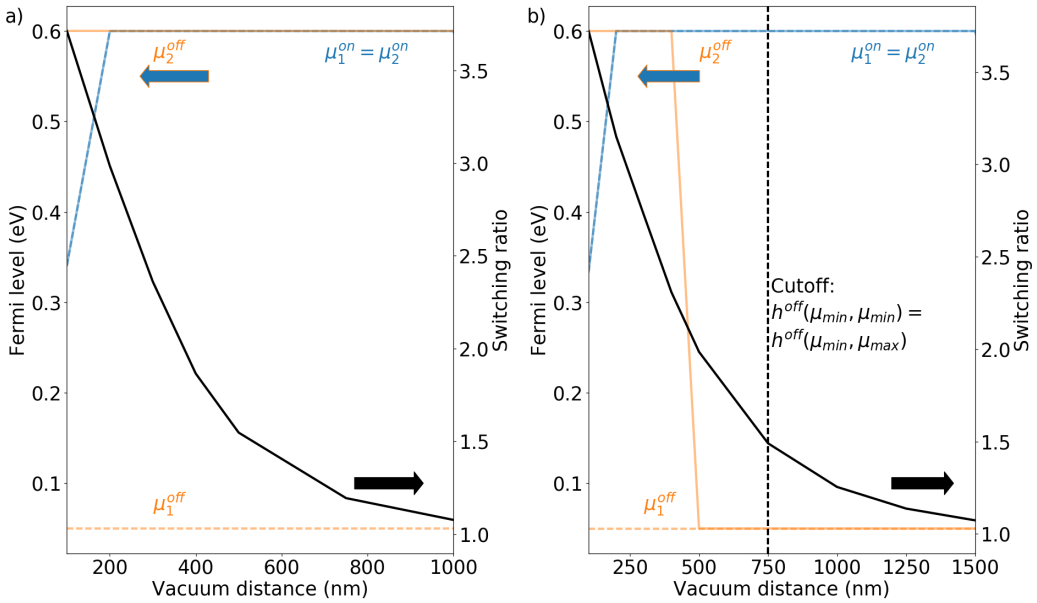

Figure 3.12: Fermi level dependence on vacuum spacing for dielectric thickness of (a) 300 nm and (b) 1000 nm with SiO_2 as the dielectric

for a thermal switch, rendering the electrostatic biasing less effective, even at short distances.

We next analyze in more detail the optimal Fermi levels for back-gated graphene as

a function of gap thickness with only SiO_2 as the dielectric. Previously we found for the graphene membrane case that the on-state Fermi levels grow to $\mu_1 = \mu_2 = \mu_{max}$ as the vacuum gap separation increases. As the membranes get further apart, increasing the density of states becomes more important for maximizing heat flux than occupying lower frequency modes. That trend is replicated here, as shown in Figure 3.12a and b, but it is much less gradual. Only for very small gap spacings $\leq$ 200 nm are the Fermi levels not maximized. One proposed reason for the trend being less gradual is the coupling between the plasmon and the SiO_2 phonon-polariton modes reduces the pressure to maximize heat flux through lower frequency modes. The spectral thermal conductance from subplots (2) in Figures 3.8b, 3.9b, and 3.10b are shown again in Figure 3.13, superimposed on the thermal conductance for just graphene membranes. The membranes have the same Fermi levels as the on-state of the case with the SiO_2 dielectric. The phonon-polaritons from the SiO_2 have the effect of splitting the plasmon among different hybrid spectral bands, and these hybrid modes are localized closer to the graphene surface. At vacuum gap distances greater than 500 nm, the hybrid modes have decayed and the plasmon and phonon-polaritons contribute to heat flux independently. However, they still operate through distinct spectral bands, where the most plasmon-like mode, which is the only one that can be modulated by biasing, occurs at ~0.06 eV. This resonance is much bluer without the hybridization to underlying dielectric. As a result, the tunable modes are pinned at lower frequencies, and only the density of states and resonance overlap need to be considered for optimizing on-state Fermi level. Maximizing these two features drives the Fermi levels to μ_{max}.

There is continued interplay between resonance overlap and density of states for the off-state. At higher gap spacing, the density of states considerations win out, and it is more beneficial to reduce Fermi level such that $\mu_1 = \mu_2 = \mu_{min}$. At lower spacings, however, the resonance coupling is more significant, and it is more beneficial for the Fermi levels to be offset with $\mu_1 = \mu_{min}$ and $\mu_2 = \mu_{max}$. In Figure 3.12a, where the dielectric is 300 nm thick, at a vacuum gap spacing larger than 1 μm, the switching ratio is close enough to one that the optimization fails and the Fermi levels are meaningless. With the dielectric layer 1000 nm thick, shown in Figure 3.12b, this point is reached at a vacuum gap of 1500 nm.

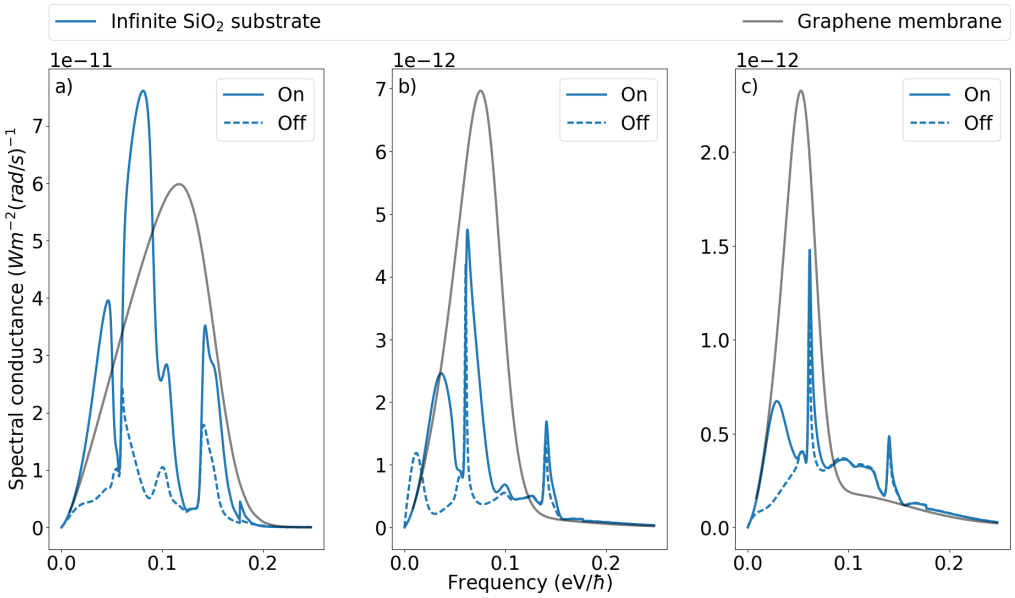

Figure 3.13: Spectral thermal conductance with and without a substrate at vacuum gap separation of (a) 100 nm (b) 500 nm and (c) 1000 nm. The phonon-polaritons from the SiO_2 split up the graphene plasmon into different spectral bands. The band that can be modulated with Fermi level even at vacuum gap distances of 1000 nm lies around 0.06 eV.

The immediate conclusion of this section is that the trade-offs for maximizing the switching ratio for realistic back-gated field effect devices are more complicated than for graphene membranes. There is the consideration of the dielectric background environment, manifest in the real part of the dielectric and silicon permittivities. There is also the fact that these dielectrics are themselves optically active, and by their own phonon polaritons, they contribute to radiative heat flux in a pathway that cannot be effectively modulated at gap distances greater than 500 nm. The hybridization between the phonon-polaritons in the dielectric and the graphene plasmon can also cause resonances to be frequency shifted. There are however some general takeways. SiO_2 is the best dielectric for near field heat switching, mainly due to the real part of the permittivity being small compared to the other dielectrics. It also is beneficial to have a thick dielectric layer if the vacuum gap is 500 nm or greater. These considerations motivate our experiment sample design, discussed in Section 3.5.

3.5 Proposed Experiment: Silica Optical Flat & Thermal Oxide on Silicon

In this section, the theoretical results from the previous section are weighed against the practical limitations of designing an experimental sample. Of the four oxides

analyzed in the previous section, SiO_2 is the best candidate gate dielectric for thermal switching. It is also best to use a thicker dielectric layer, which has the effect of lowering the heat flux in the off-state.

However, it is not immediately clear whether there is a substantial benefit for having independent control of each Fermi level. As shown in Figure 3.12b, for samples with a 1 micron thick layer of SiO_2 and at gap distances greater than 500 nm, the optimal Fermi levels μ_1 and μ_2 are equal in both the on- and off-states. There are also practical reasons why one cannot employ very thick dielectric layers. The thicker the gate dielectric, the higher the applied voltage must be to get the same change in Fermi level. The Fermi level μ of graphene on a dielectric of thickness d is related to applied voltage ΔV by $\mu \propto \sqrt{\Delta V/d}$. Hence, increasing the dielectric thickness only requires a proportional increase in applied voltage to get the same change in Fermi level. However, it is well documented for SiO_2, the thicker the film, the *worse* the breakdown strength [133]. As a result, there is an opposing need to use a "thin" dielectric.

There is an optimal thickness around 300 nm for SiO_2. As shown in Figures 3.9a and 3.10a, at higher gap spacings of 500 nm and 1000 nm, a 300 nm layer of SiO_2 already approaches $\sim 50\%$ and $\sim 30\%$, respectively, of the maximum thermal switching achievable for an infinitely thick dielectric layer. Silicon wafers with a layer of thermally grown SiO_2 are also readily commercially available. The wafers used in this thesis are p-type silicon with a 285 nm layer of thermal oxide, since at that thickness, the SiO_2 reaches a quarter wave condition and any subsequent thin films grown on top of or transferred to the wafer are easily visible. The wafers are also additionally chlorinated and annealed to help remove metal impurities and defects that can contribute to dielectric breadown. However, as is discussed in Chapter 4, these additional treatment methods are not adequate to avoid dielectric breakdown. An additional 8 nm captivation layer of Al_2O_3 is grown by atomic layer deposition (ALD). Hence, the final proposed sample consists of graphene on a substrate of silicon with a 285 nm thermal layer of SiO_2 and an 8 nm layer of ALD Al_2O_3.

The final practical consideration is that one of the two samples must be upside-down, making it difficult to apply electrical leads to bias the graphene. Because of this difficulty and also because of the added benefit of having a thick dielectric, the top sample substrate is a $\sim$3 mm thick, silica optical flat. Optical flats are polished flat with a height deviation of $\pm$ 60 nm over a circular area of diameter 12.7 mm, making

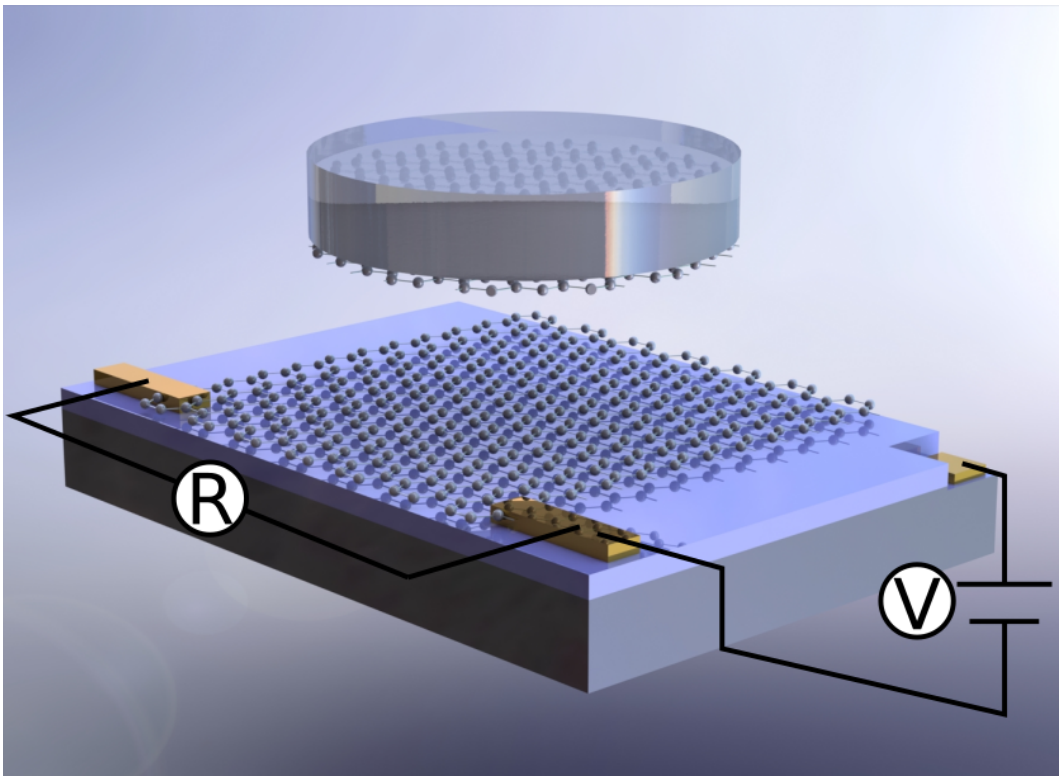

Figure 3.14: Schematic of final proposed sample

them an ideal substrate for studying near field heat transfer [27, 38]. A diagram of the complete sample is shown in Figure 3.14.

As the top substrate is so thick, the top graphene Fermi level is not controlled by external voltage and can either be floating at its intrinsic level, or it can be shorted to the graphene sheet below it. The thermal conductance for these two cases is shown in Figure 3.15 at a vacuum gap of 1 μm. The spectral thermal conductance plots are largely similar to those shown in the previous section, although in this case the Fermi levels are not necessarily optimized. Again at vacuum gap distances as high as 1 micron, the SiO_2 phonon polariton acts as a modulation loss pathway, and only the graphene plasmon can be modulated. As we learned in the previous section, for the off-state there is not a big difference when the Fermi levels are both minimized to μ_{min} or when they are separated between μ_{min} and μ_{max}. Hence, in the right plot in Figure 3.15, at low Fermi levels near μ_{min}, the thermal conductance is approximately equal when the Fermi levels are the same or when one Fermi level is pinned.

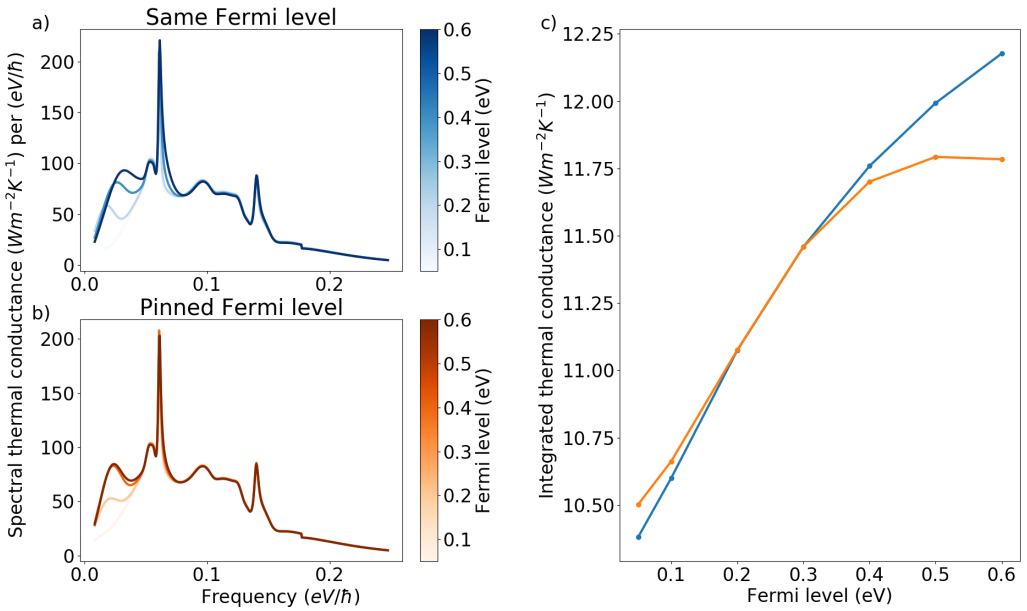

Figure 3.15: Spectral heat flux at a vacuum gap distance of 1 μm for cases (a) when fermi level of top and bottom chip are the same and (b) when the top fermi level is pinned to 0.3 eV. The lighter color implies a lower Fermi level. c) The integrated thermal conductance. The modulation is better when the Fermi levels are the same.

At high Fermi levels, however, when the switch is "on", there is a big difference between these two cases. The thermal conductance bends over for the pinned case, when the Fermi level becomes greater than the pinned value of $\mu_2 = 0.3$ eV. It is therefore much better if the Fermi levels are the same, and during the experiment, for this sample configuration, there is a benefit to shorting the top graphene sheet to the bottom. As it turns out, it is very difficult to achieve any *other* configuration, because the top and bottom samples are often touching, shorting them together. The final anticipated thermal conductance spectrum where the Fermi levels are limited to $\mu_{min} = 0.05$ eV and $\mu_{max} = 0.30$ eV, which is the likely range to which the experimental apparatus described later is limited, is shown in Figure 3.16, for a spacing of 100 nm (purple) and 1 μm (black). The switching ratio at these distances is 2.1 and 1.1, respectively. The on-state is when both Fermi levels are at $\mu_{max} = 0.3$ eV, the off-state is when the Fermi levels are at $\mu_{min} = 0.05$ eV. Even at large gap spacings we anticipate being able to demonstrate heat flux modulation.

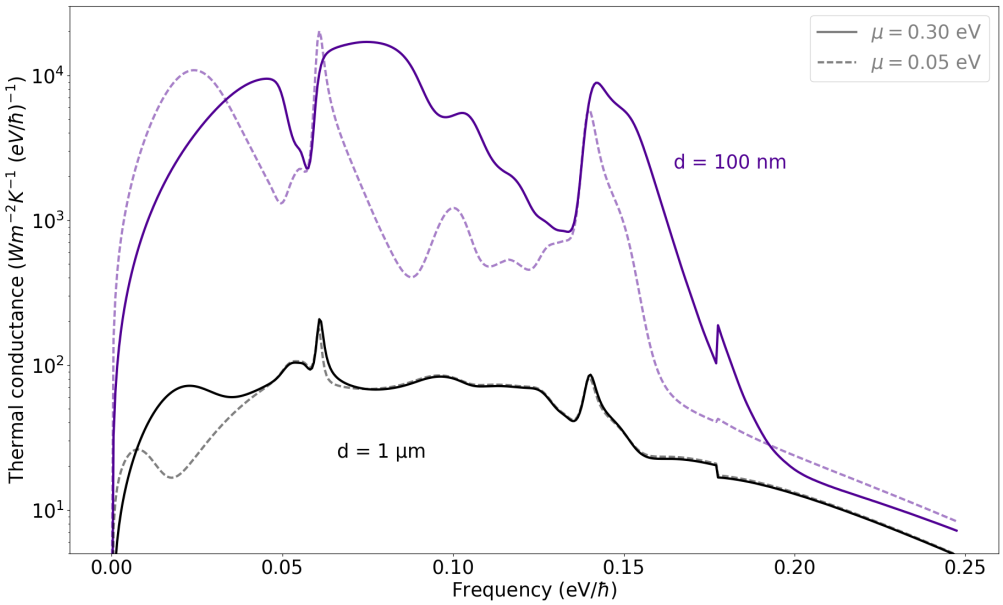

Figure 3.16: Spectral thermal conductance for vacuum gaps of $d = 100$ nm (purple) and $d = 1$ μm (black) with equal top and bottom Fermi levels of 0.3 eV (solid) and 0.05 eV (dashed).

3.6 Conclusion

In this chapter, we introduced the theory to describe the radiative transfer between graphene sheets and showed that heat flux modulation could be achieved by electrostatic gating. We identified the optimal Fermi levels for turning the thermal switch off and on. We first studied floating graphene membranes, which although not experimentally realizable are a simple system for understanding the balance between the density of states, the thermal envelope, and overlapping of plasmonic resonances. We then examined an experimentally achievable setup that uses an optically active gate dielectric, from which SiO_2 is the clear winner. Finally, we theoretically motivated an experimental sample with a bottom substrate of 285 nm of SiO_2 and 8 nm of Al_2O_3 with a Si back electrode and a top substrate of a SiO_2 optical flat. Even at large gap spacings, we anticipate this configuration would allow for an observable heat flux modulation.

Chapter 4

APPARATUS AND SAMPLE PREPARATION FOR HEAT TRANSFER MEASUREMENT

This chapter has been adapted in part from:

Nathan H. Thomas, Michelle C. Sherrott, Jeremy Broulliet, Harry A. Atwater, and Austin J. Minnich. Electronic Modulation of Near Field Radiative Transfer in Graphene Field Effect Heterostructures. *In preparation*, 2019

4.1 Introduction

Having determined the sample geometry in the previous chapter, in this chapter we are now ready to describe the experiment that can measure the predicted heat flux modulation. Near field radiative heat transfer experiments fall into one of three categories, defined largely by the geometry of the sample being investigated. In one case, the samples are "large"[1] and planar, separated from one another by physical spacers [27, 29, 31, 32, 38]. In the second case, the samples are much smaller, typically fabricated using modern lithographic techniques and are suspended above one another by piezo-actuators [28, 33, 34, 134]. Experiments in the final category employ a planar sample and a spherical atomic-force microscope tip [30, 57, 58].

Naturally, each of these experiments comes with their own set of unique trade offs. In the first case, the experimental setup can use commercial heat flux and temperature sensors and doesn't require intricate control of piezoactuators and custom resistive thermometers that are necessary for the other two classes of experiments. However, the samples must be polished sufficiently flat to allow for 100 to 1000 nm scale gaps across an area $\sim$1 cm^2. In the other cases, the sample uniformity is less important, but the sample positioning is complicated and the temperature sensors are custom Pt resistors or AFM tips. In this thesis, we investigate the electrostatic modulation of cross-plane heat transfer of large area gate-tunable samples. For that reason, we construct an instrument, building off the previous works from the first class of experiments. In this chapter, we introduce the instrument design and sample fabrication protocol.

[1] Large is a purposely vague term, but it mainly refers to samples with bulk substrates that can be manipulated with the human hand.

4.2 Instrument Layout

A diagram and photo of the instrument layout are shown in Figure 4.1. The heart of the instrument is a Janis ST-100 cryostat, which houses the sample and is connected to a Lakeshore 355 PID temperature controller. The temperature controller has two independent PIDs for precise control of two heating elements. The first is connected to the cryostat cold finger, which is kept cold with a liquid nitrogen reservoir, and acts as the heat sink for the thermal absorber. The second is connected to an insulated Kapton resistive heater, which acts as the heat source for the thermal emitter. A diagram of the cryostat and heater layout are shown in Figure 4.2a. At the base of the cryostat is the sample stage, which is screwed to the coldfinger, as shown in Figure 4.2b. The stage is designed to be removed without disturbing the graphene device, such that it can be ferried in and out of the clean room without dust getting between the top and bottom samples.

The other necessary components shown in Figure 4.1, are the DAQ9211 National Instruments microvolt meter, the Keithley 2410 source meter, and the Fluke 8808a multimeter. The DAQ9211 is used to measure thermocouple signals and the microvolt signal from the heat flux sensor. The Keithley 2410 supplies the bias to the bottom graphene sample, and the Fluke multimeter has two functionalities.

The first and primary use of the Fluke multimeter is to measure the graphene surface resistance while it is being biased. The bias at which the surface resistance is maximized is the charge neutral point (CNP), or where the graphene Fermi level is near zero. The second use is to measure the input power into the resistive heater to calibrate the heat flux sensor, as described in Section 4.3. To measure both signals independently with a single multimeter (but at separate times), we employ a computer controlled multiplexer switch box. A circuit diagram of the switch box is shown in Figure 4.3.

The box contains 8 USB-controlled relays each with three input-output leads: normally-closed (NC), normally-open (NO), and common (C). As wired, the switch

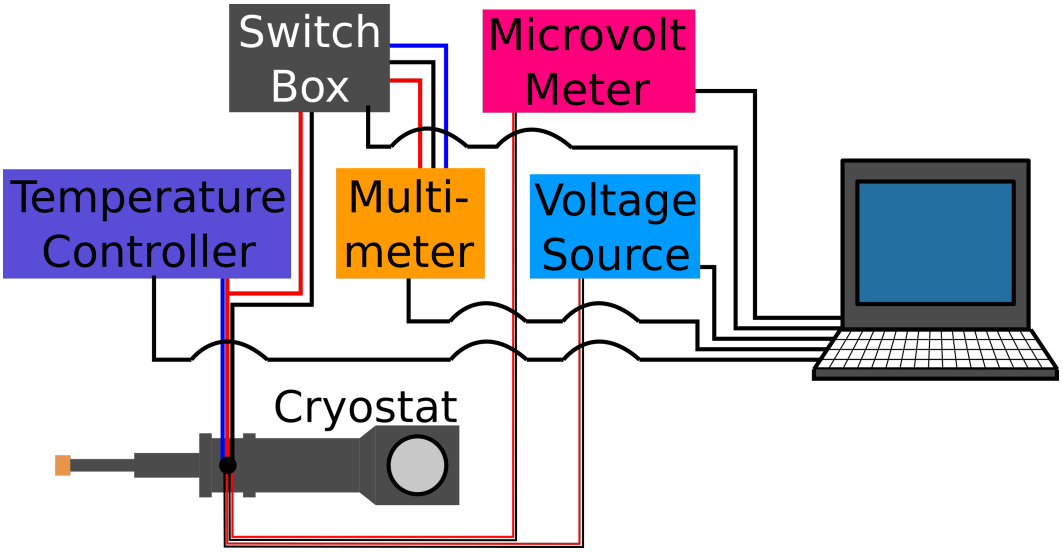

(a) Diagram of Instrument Layout

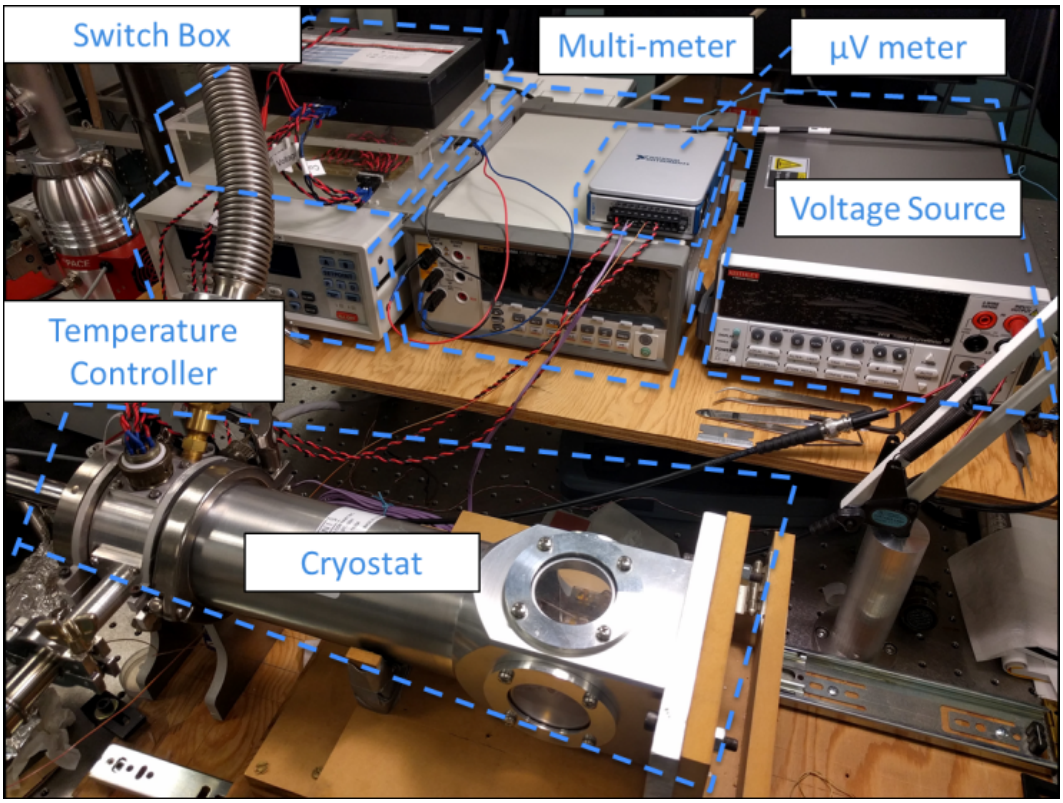

(b) Photo of Instrument Layout

Figure 4.1: Complete layout of heat transfer measurement instrument. The sample is housed inside the cryostat that is pumped to $\sim 1 \times 10^{-6}$ Torr. The multi-meter, muV meter, voltage source, and switch box are all controlled from a custom computer interface.

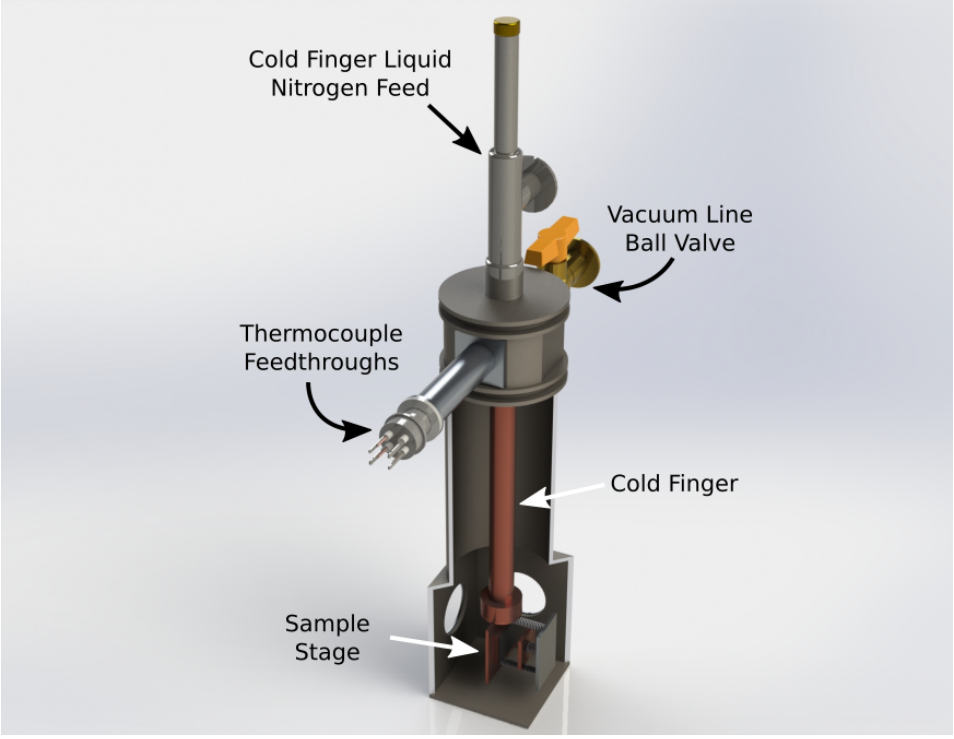

(a) Diagram of cryostat

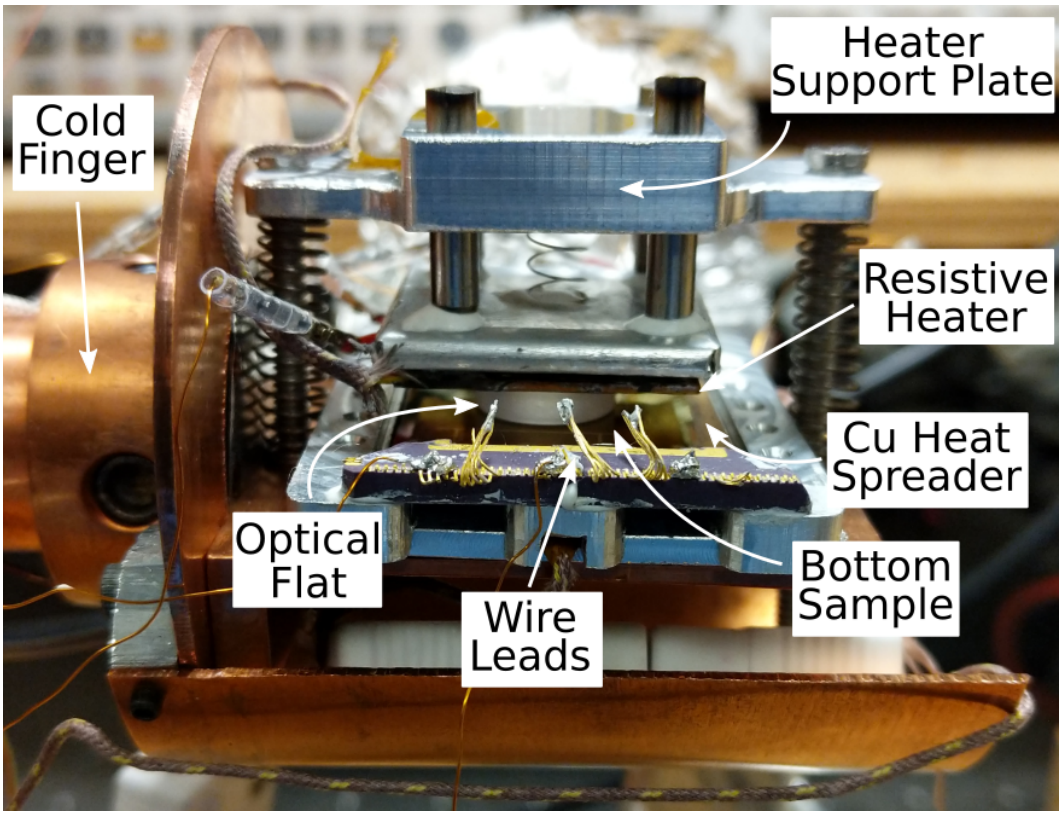

(b) Photo of Sample Stage at Base of Cryostat Coldfinger

Figure 4.2: Cryostat diagram and photo of sample stage.

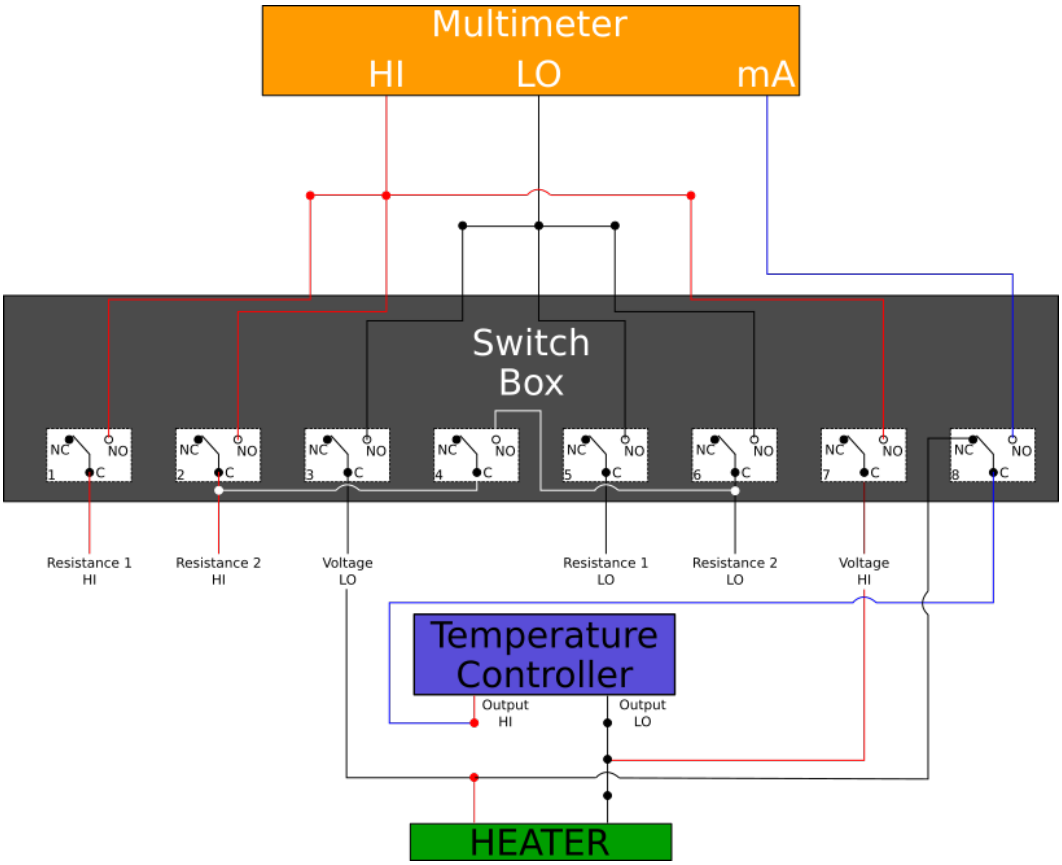

Figure 4.3: Diagram of Switch Box Circuit

box offers a way to measure three independent resistance or voltage signals and a single current measurement. The three resistance and voltage signals are labeled as Resistance 1, Resistance 2, and Voltage, but all three circuit paths go to the same HI and LO leads of the multimeter. The difference in the three signals lies only in how the multimeter is programmed. To measure the applied heating power, both the current and a voltage switches are opened as shown in Figure 4.4, where the arrows indicate the current path. The ammeter connections for the multimeter are through the LO and mA leads. The heating power applied to the resistive heater is simply the product of the current and voltage.

4.3 Heat Flux Sensor Calibration

The heat flux sensor is an Omega HFS-4 thermopile that produces a voltage response proportional to a linear thermal gradient, which is in turn proportional to the heat flux through the sensor. The sensor must be calibrated to determine the conversion factor between incident heat flux and output voltage. As the sensor voltage relates to the incident heat flux by the temperature dependent Seebeck effect and thermal

conductivity, the heat flux sensor must be calibrated at all working temperatures. The final temperature dependent calibration factors were determined over three stages. In the first stage, the temperatures were kept within 100 °C of room temperature to determine the sensor's basic functionality. In the second stage, temperatures were decreased to close to 90 K to determine the thermal leakage out of the heater. In the final stage, after leakage pathways were determined inconsequential, the sensor was calibrated across all temperatures from room temperature to 90 K.

Stage I: Prelimary Functionality

The basic way to calibrate the heat flux sensor is to accurately measure the applied thermal power into the sensor, while recording the resulting sensor voltage. By tracking the linear response of the sensor signal over different input powers, a conversion factor is determined. The thermal input power is delivered by a resistive heater, secured directly onto the sensor with Kapton tape. The temperature of the sensor is kept constant while the different input powers are applied to the heater. As mentioned above, to measure the input power, the applied current and voltage into the the heater are measured with the Fluke multimeter with the switch box configured as shown in Figure 4.4.

As the heater is in direct contact with the sensor, incremental steps in applied power require only marginal increases in heater temperature. However, these increases also cause the heatflux sensor temperature to change. The temperature of the cold finger must be reduced to compensate. A PID protocol is implemented in software to keep the sensor temperature constant to within ±2° C. After the heat flux signal has equilibrated, the mean values are recorded within a collection interval. A representative calibration experiment is shown in Figure 4.5.

The mean heat flux sensor signal values versus mean input power are plotted in Figure 4.6 over temperatures from 225 K to 300 K. The data all exhibit a strong linear trend. The slopes of the best-fit lines change with sensor temperature, as expected, due to the changing Seebeck coefficient and thermal conductivity. However, the y-intercept or the background heat flux through the sensor also changes. As the cryostat pressure is around 5×10^{-6} Torr, convective heat transport into the sensor

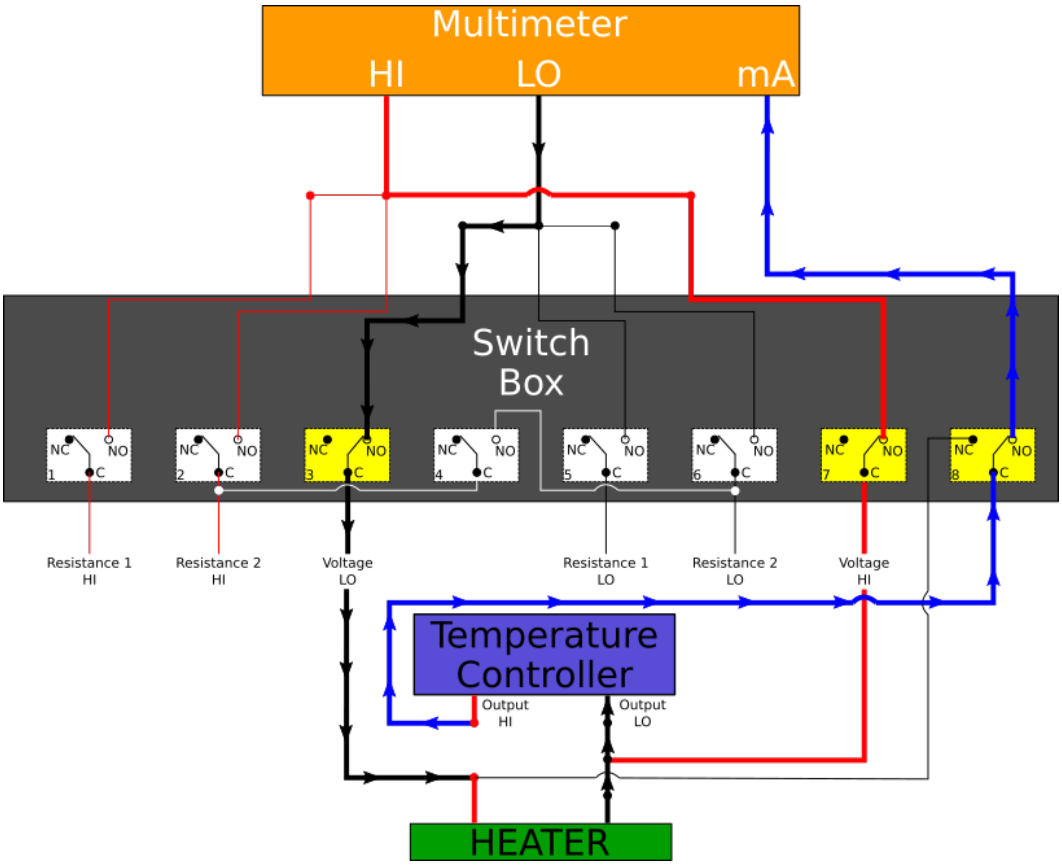

Figure 4.4: Switch box configuration for simultaneous voltage and current measurements. Current follows in the direction of the arrows.

is negligible, and the primary conductive heat pathway into the sensor is through the resistive heater. We therefore predict the large background signal is due to radiative flux into the sensor. As the sensor temperature is changing, a radiative background signal would also explain why the y-intercept of the linear fits depends on temperature.

With the slopes taken from each linear fit, each y-intercept is converted into a heat flux. A radiative model $q = a\sigma(T^4 - T_{sensor}^4)$ is then fit to these heat flux data, where the area normalized emittance a and ambient temperature T are fitting parameters. The results of the fit are shown in Figure 4.7 with $a = 0.6$ and $T = 294$ K, indicating that the cryostat is radiating heat to the heat flux sensor. To overcome this radiative

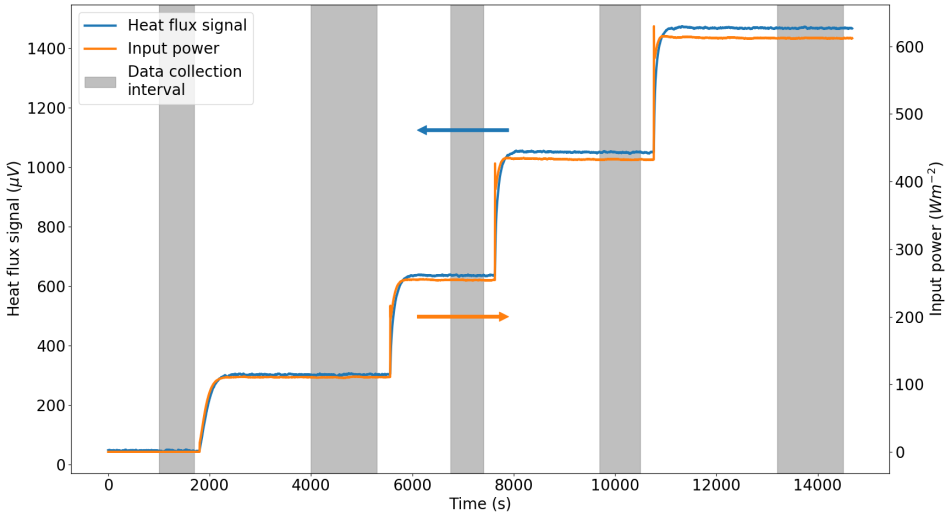

Figure 4.5: Raw heat flux voltage signal at different heater temperatures / different input powers. After the heat flux sensor signal has equilibrated, data are recorded within a defined interval (grey). Linear fits to the average of each interval are used to determine the sensor calibration factor as shown in Figure 4.6.

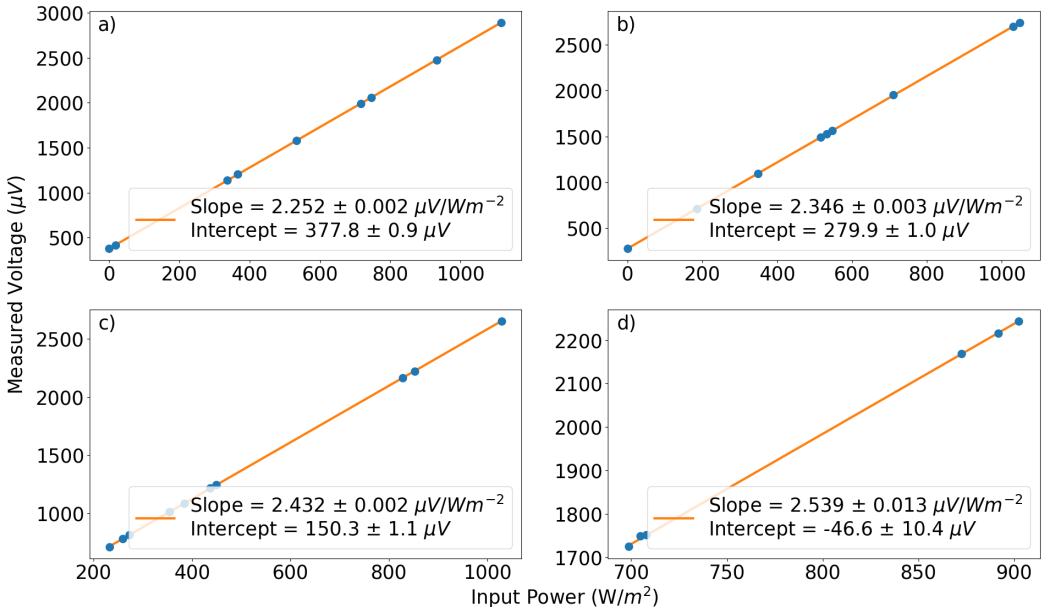

Figure 4.6: Stage I calibration: heat flux sensor signal vs input power at temperatures (a) 225 K, (b) 250 K, (c) 275 K, and (d) 300 K.

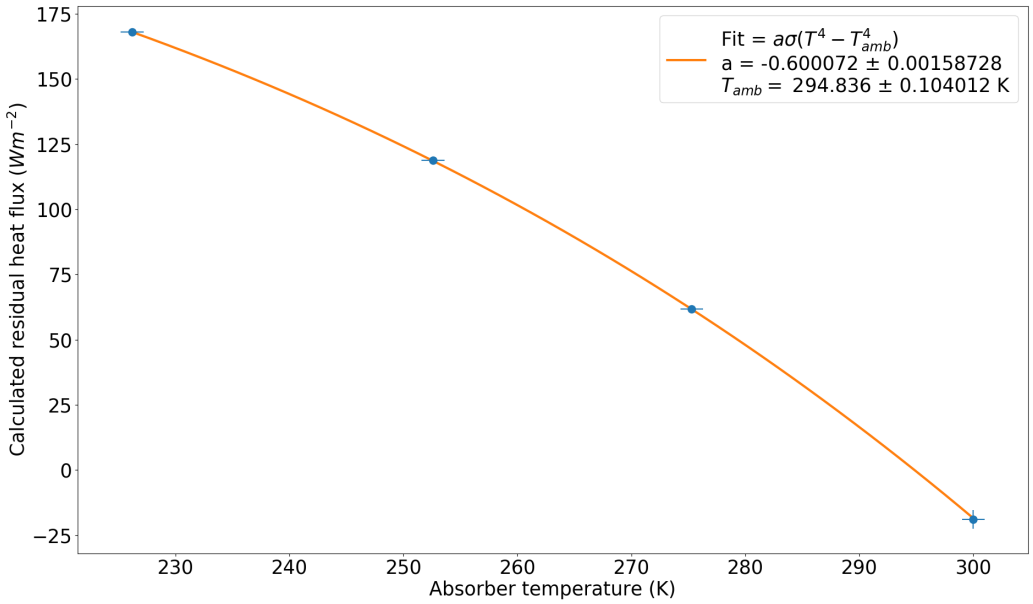

Figure 4.7: Far-field radiative fit to the y-intercept background heat flux values. The background heat flux is predominately radiative, where the cryostat is radiating to the sensor.

background signal, we design a radiation shield from a 2.75" diameter copper pipe, machined smooth for a reflective finish. The shield is a clam-shell configuration, allowing easy access to the sample stage. A photo demonstrating the clam-shell functionality is shown in Figure 4.8. The calibration experiments are then repeated with the radiation shield, the results of which are shown in Figure 4.9. Initially, the background signal is reduced by about a factor of 9. Over time, however, the copper oxidizes, lowering the effectiveness of the radiation shield. Various copper oxides have much higher thermal emittance than metallic copper. The inside of the radiation shield is therefore coated with aluminum foil, which is nearly as effective as the original reflective copper.

In the radiative model for the heat flux experiments with the radiation shield, the fit to the ambient temperature is nearly 307 K, which is over 10°C higher than the recorded ambient temperature of the laboratory, which is around 294 K. This discrepancy is indicative of two things. The first is that the purely radiative model isn't perfect. Having limited the incident radiation with the Cu shield, there are likely other conductive sources of heat flux. The second is that the sensor is not necessarily

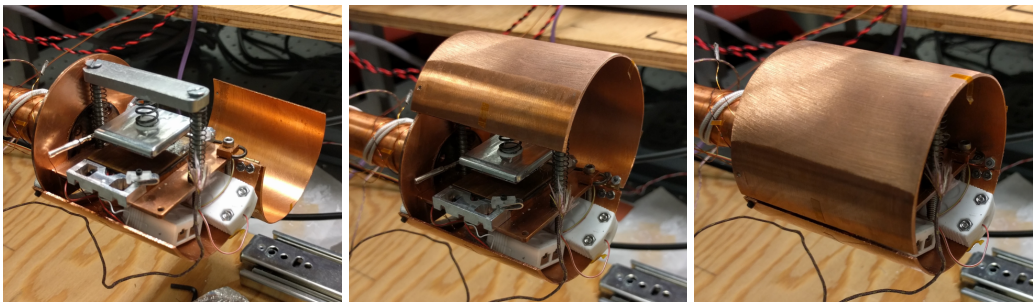

(a) Open (b) Half-open (c) Closed

Figure 4.8: Radiation shield. The clamshell configuration allows for easy access to the sample holder.

at equilibrium. The sensor signal asymptotically approaches its equilibrium value, as evidenced in the temperature decay experiments in Section 4.3. It can take many hours for the sensor signal to reach its steady-state value. As it is not feasible to wait that long (there is a finite reservoir of liquid nitrogen for example), over the course of the experiment, the signal drifts. This drift is characterized initially in Section 4.4 and again in more detail in Chapter 5. Here, as these background signals are quite small, the signal drift has a proportionally large effect on the final measured value. As a result, even though the radiative fit shows qualitative agreement with the measured data, the more important features are the monotonic trend downwards with temperature and the remarkably reduced background signal over the experiments without the radiation shield. These facts point to the background signal still being spurious heat flows into the sensor, (through lead wires, thermocouples, or even radiation) as opposed to sensor instability. In fact, these experiments are repeated in Section 4.4, where a linear model is preferred over a much larger temperature range.

Stage II: Determine Thermal Leakage out of the Heater Support

Having corrected for the radiative background and validated the functionality of the heat flux sensor, we can calibrate the sensor down to liquid nitrogen temperatures. At these temperatures, Kapton tape is inadequate for making sure the heater remains in adequate contact with the heat flux sensor. The heater is pressed onto the sensor using two different methods instead. In the first, the heater is secured with epoxy to the spring-loaded support that is ultimately used in the final experiment (see Figure 4.2b) and screwed down onto the sensor. In the second, the heater is pressed in place with two simple set screws. These support systems for the heater invariably

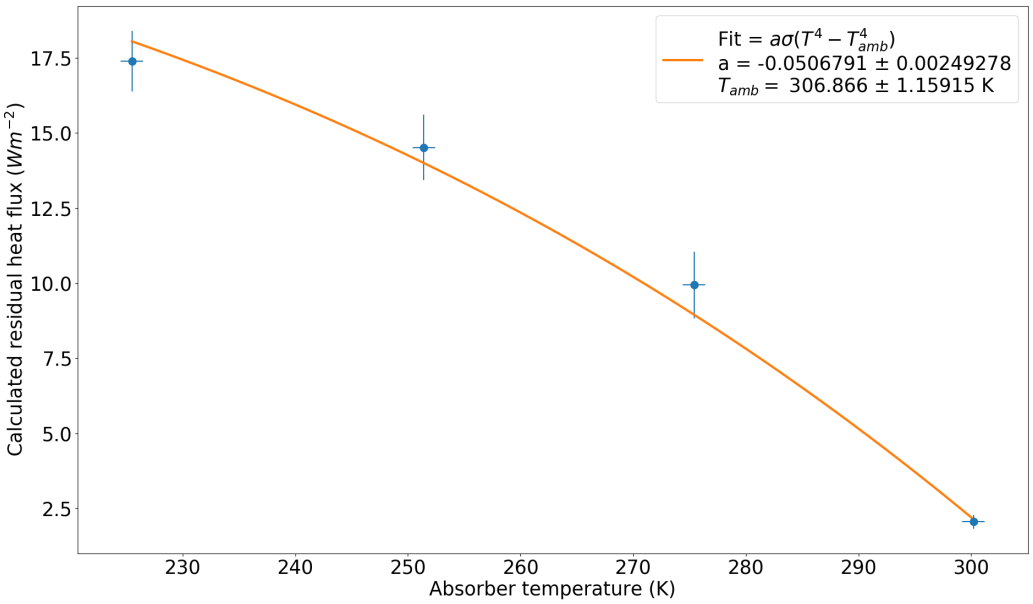

Figure 4.9: Stage I Calibration: With Radiation Shield

provide pathways for thermal leakage. As modeling all sources of thermal leakage is unreliable, in this section we introduce a simple thermal resistor model to determine the ratio of the heating power directed into the heat flux sensor to that diverted away from it.

The experiment has two steps: one where the heater is firmly placed on the heat flux sensor, and the other where the heater is suspended above it. After the cryostat reaches high vacuum, the coldfinger is cooled with liquid nitrogen, while the heater temperature is continuously monitored. By comparing the temperature decay rates of the heater in each step, we relate the ratio of heat lost to heat directed into the sensor.

A thermal resistance model is shown Figs. 4.10, where the resistance through the leakage pathway and through the heat flux sensor is denoted by $R_{leakage}$ and R_{hfs}, respectively.

In both cases, the temperature of the heater as a function of time is

$$C\frac{dT_h}{dt} = Q(t), \tag{4.1}$$

where C and T_h are the thermal capacitance and temperature of the heating element, respectively, and Q is the time dependent heat flux. In the case where the heater is

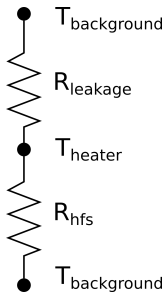

Figure 4.10: Resistor model for heater calibration experiments. When heater is suspended above the heat flux sensor, then $R_{hfs} \rightarrow \infty$.

in contact with the heater, we get the first order ODE,

$$C\frac{dT_h}{dt} = \frac{T_h - T_b}{R_{leak}} + \frac{T_h - T_b}{R_{hfs}} = (T_h - T_b)\frac{R_{leak} + R_{hfs}}{R_{hfs}R_{leak}}. \tag{4.2}$$

Using the adjoint method, we arrive at a solution for the heater temperature,

$$T_h(t) = T_h(0)e^{-\frac{t}{c_1}} + \frac{1}{c_1}\int_0^t dt' e^{\frac{t'-t}{c_1}} T_b(t'), \tag{4.3}$$

where

$$c_1 = C\frac{R_{hfs}R_{leak}}{R_{leak} + R_{hfs}}. \tag{4.4}$$

For the case where the heater is suspended, R_{hfs} is infinite, and

$$c_1 \rightarrow c_2 = CR_{leak}. \tag{4.5}$$

By comparing c_1 and c_2, we ultimately get the ratio of the thermal resistances,

$$\frac{R_{leak}}{R_{hfs}} = \frac{c_2}{c_1} - 1. \tag{4.6}$$

We then fit Equation 4.3 to the measured temperature data, where c_1 or c_2 are the only fitting parameters. Plots showing the fit for c_1 over three temperature ranges from 290 K to 250 K, 250 K to 180 K, and from 180 K to 77 K are shown in Figure. 4.11a-c, respectively. The fits reproduce the measured results well, but further analysis is still necessary. In the case in Figure 4.11b, in the temperature range of $250K$ to $180K$, the heater temperature actually tracks *less than* the background temperature.

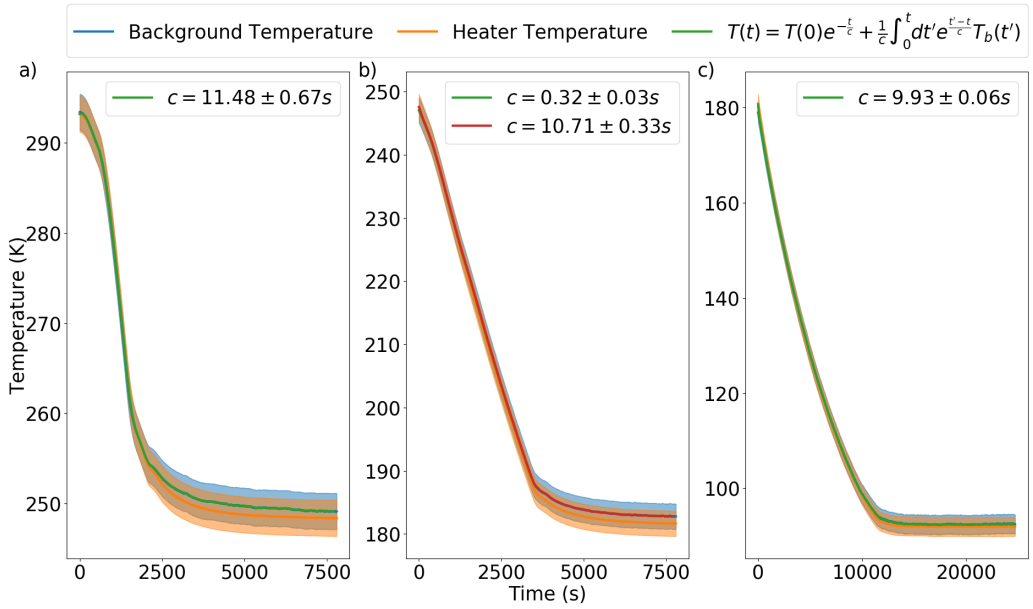

Figure 4.11: Temperature decay and model fit for heater in contact with heat flux sensor for temperature ranges (a) 290 K - 250 K (b) 250 K - 180 K and (c) 180 K - 77 K

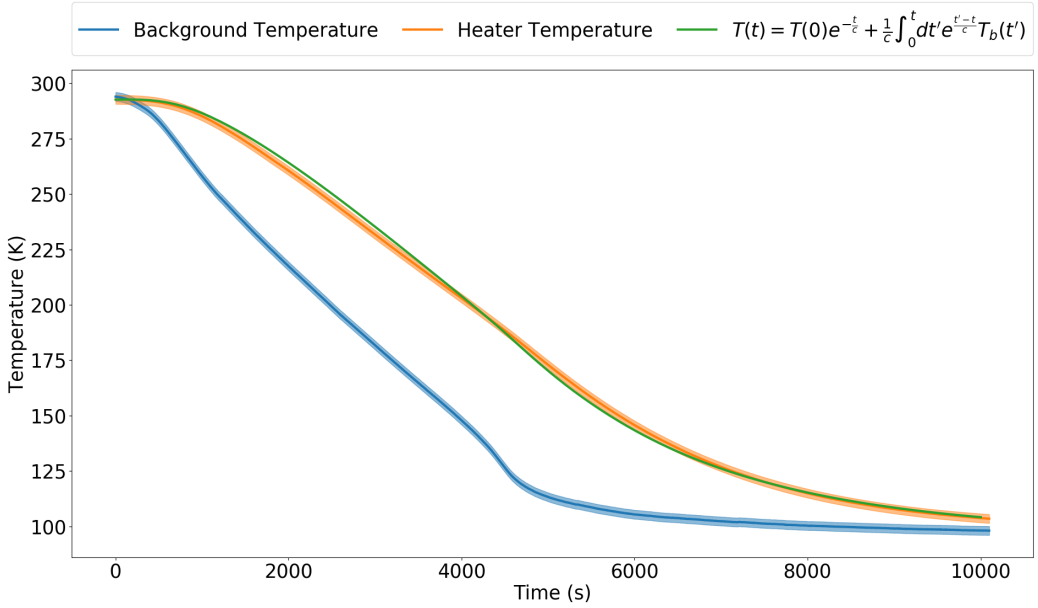

Figure 4.12: Temperature decay and model fit for heater suspended above heat flux sensor for complete temperature range 290 K - 77 K.

This is simply due to the measurement sensitivity of the thermocouples. However, it has problematic consequences for the fit. In Eq. 4.3, the temperature of the heater is bounded from below by the background temperature in the limit $c \to 0$. Because the measured heater temperature is less than that of the background, the fitting algorithm approaches the $c = 0$ condition. If we take the mean of the fits from the other two temperature ranges, we see that it also adequately models the measured data, indicated by the red curve. Hence, we take the parameter c_1 to be the mean of the fitting parameters from the first and third temperature range, $c_1 = 10.7 \pm 0.3s$.

In the case where the heater is suspended above the sensor, data are taken in a single run over the entire range from 290 K to 77 K with a fit of $c_2 = 1753 \pm 1$. Hence, we find the ratio of the leakage thermal resistance to the thermal resistance of the heat flux sensor to be 164 ± 5. Only $0.61 \pm 0.02\%$ of heat is lost and the remainder is directed into the heat flux sensor.

Stage III: Characterization at Relevant Liquid Nitrogen Temperatures

Although the thermal leakage out of the heater is minimal, the final sensor calibration is conducted where the heater is actually removed from the support plate. In this configuration, where even less heat is lost, the heater is instead pressed to the heat flux sensor with two set screws. Two ceramic washers and a glass slide epoxied to the heater separate the heater from the screws and act as an additional thermal barrier. When the heater is suspended, it is held up by two wires, with the screws loosened but still pressing against the heater. With tests conducted in this way, the equilibrium temperature of the suspended heater after cooling remains approximately 125 K, while the heat flux sensor temperature is 90 K. The thermal resistance is so high between the heater and the ambient cold that the equilibrium temperature remains nearly 30 °C above the surrounding sensor temperature. The small source of background heat into the heater that can account for the temperature difference is discussed in Section 4.4.

Having established a negligible amount of heat is lost from the heater, we are now in position to re-calibrate the heat flux sensor at relevant temperatures, replicating the methods outline in Stage I in Section 4.3. The heater is again pressed firmly on the heat flux sensor, which is kept at constant temperature, to within ±2 °C, and the input power into the heater is recorded over five different temperatures. The resulting data are shown in Figure 4.13 at all five temperatures. The summary of the fits is shown in Table 4.1. The y-intercept values represent a background “DC”

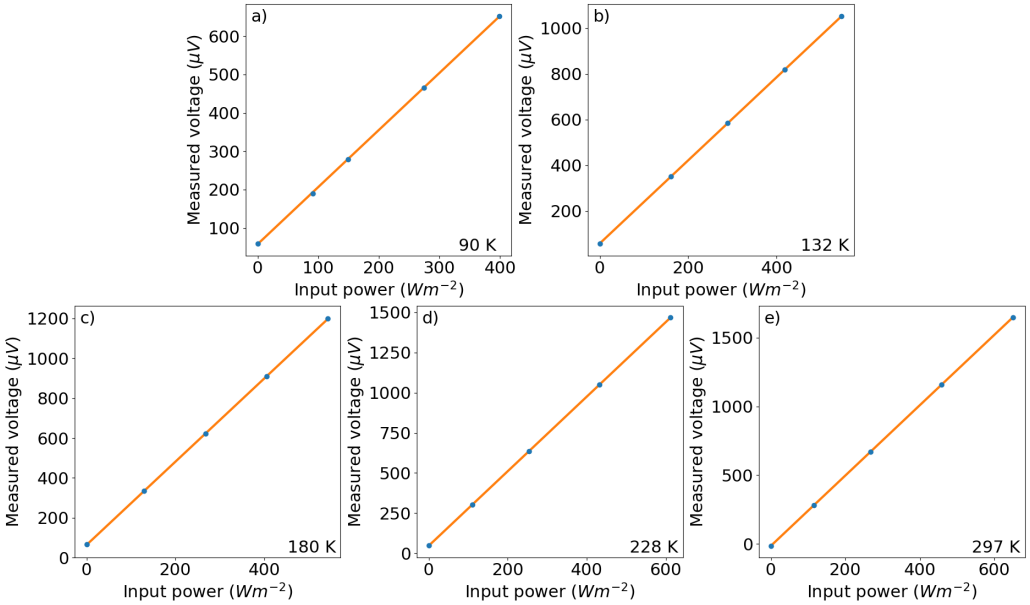

Figure 4.13: All calibration plots for heat flux sensor at different temperatures area normalized to the area of the heat flux sensor

Heat Flux Sensor Temperature (K)	Slope ($\mu V/Wm^{-2}$)	Y-Intercept (μV)
90	1.487(6)	58(1)
132	1.817(1)	58.6(3)
180	2.087(4)	64(1)
228	2.321(1)	46.8(4)
297	2.561(1)	-14.8(2)

Table 4.1: Fitting data from all calibration plots

heat flux into the sensor that needs to be appropriately considered in the final heat flux measurements.

4.4 Background Heat Flux

The non-zero y-intercept values from the calibration fits indicate there is a small background heat flux signal that must be addressed when converting the heat flux sensor voltage signal to a heat flux value. As shown in the diagram in Figures 4.14a and b, we divide this background "DC" heat flux into two pathways, one in which the heat flows directly into the sensor, and the other where the heat flows through

the heater. As the entire assembly is radiation shielded, we attribute these small heat flows to flux through connecting lead and thermocouple wires.

The heat that flows through the heater and into the sensor ultimately also flows through the sample itself and should *not* be subtracted from the heat flux signal. The heat that flows directly into the sensor, however, does not flow through the sample and should be subtracted. We carefully measure the background heat flux signal for these two cases, where the heater is firmly pressed against the heat flux sensor and when the heater is suspended above the sensor. In the former case, heat flowing directly into the sensor and indirectly through the heater are both measured. In the latter case, only the heat directly into the sensor is measured. The results of the measurements are shown in Figure 4.15. Both curves show a monotonic decrease in background heat flow as the sensor gets warmer. The area beneath blue curve represents the heat flowing directly into the sensor, and the area between the two curves, shown in orange, represents the heat only flowing through the heater.

The breakdown strength of SiO_2 improves as temperature decreases, so all subsequent heat flux measurements where the graphene is biased are conducted at low temperature, where the cryostat cold finger is kept at 77 K and the heat flux sensor is between 86 K and 91 K. The background heat flux flowing into the sensor at these temperatures is 20 Wm^{-2} area normalized to the heat flux sensor. This corresponds to a reduction in the heat flux sensor signal of $28 \pm 5\ \mu V$. The uncertainty is due to the signal drift of the heat flux sensor, mentioned previously in Section 4.3. As the temperature of the heat flux sensor asymptotically approaches its equilibrium value, so too does the heat flux sensor signal. As shown in Figures 4.12, this equilibration takes many hours. Each data point in Figure 4.15 is collected after the sensor signal has flattened out, but the signal has been found to continue to drift by close to 5 μV. This signal drift is also addressed in Chapter 5.

4.5 Sample Fabrication

With the apparatus properly calibrated, we now turn our focus to fabricating gate-tunable graphene samples, for which there are three stages. The substrates are prepared and cleaned; the graphene is transferred to the substrate; and then the

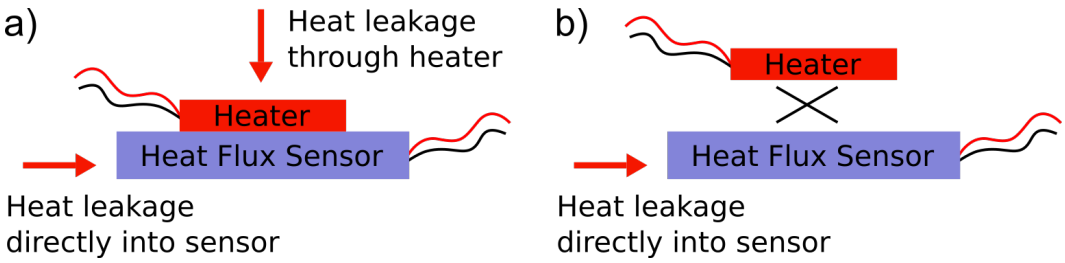

Figure 4.14: Diagram of thermal leakage pathways. a) Heat flux sensor is pressed directly onto the heat flux sensor, allowing for two paths of heat flow into the sensor, one direct and one indirect through the heater. b) The heater is elevated above the sensor, and heat only flows into the sensor directly. The heat that flows through the heater ultimately also flows through the sample, meaning that heat flow should *not* be subtracted from the end heat flux signal. Heat that flows directly into the sensor does not flow through the sample and should be subtracted.

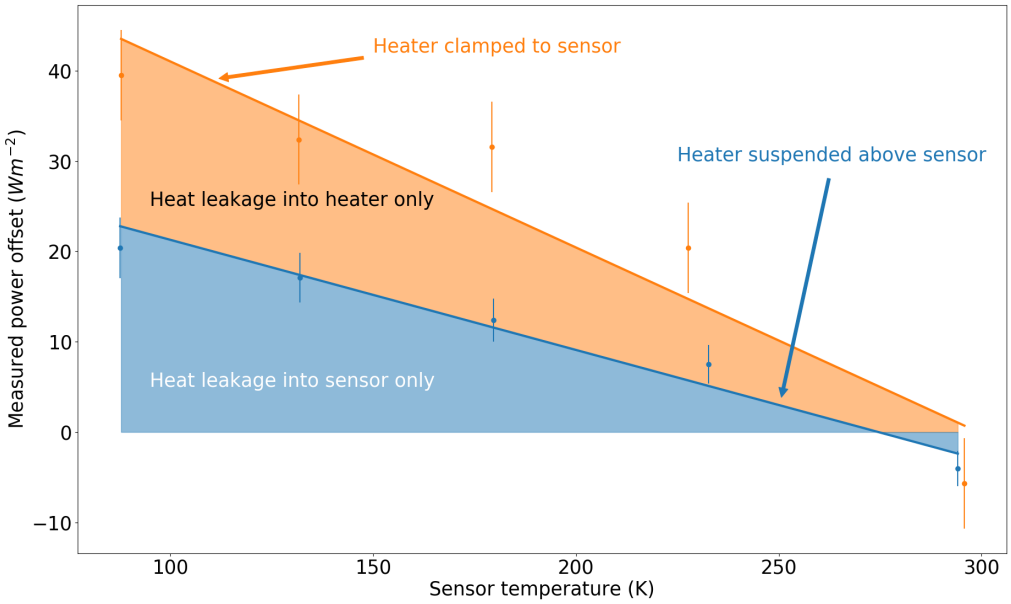

Figure 4.15: Background heat flux signal at zero input power area normalized to the area of the heat flux sensor

bonding contacts and vacuum spacers are made by electron beam lithography and electron beam deposition.

Substrate Characterization, Preparation, & Cleaning

A chief difficulty in near field heat transfer experiments, particularly between planar samples, is to keep them flat and equidistant from one another over the entire measurement area, while also maintaining a separation distance of 100 nm to 1000 nm. This obstacle is why often high precision flat optics are used [27, 31, 38]. However, wafers and particularly oxidized wafers with a layer of thermally grown SiO_2 experience bow, and can warp up to 30 μm over the wafer. Naturally, the smaller the cleaved pieces, the less grievous the absolute deflection. To estimate the surface profile of the thermal oxide wafer, we use profilometry over different parts of the sample surface. As shown in Figure 4.16, the wafer topography is quite inhomogeneous. Profiles taken in the "East-West" direction show the wafer bending downwards at the edges in a concave down shape. However, in the "North-South" direction, the wafer appears much flatter or even concave up. Such inhomogeneity is expected in thermal oxide wafers. Often additional processing is needed like annealing at high temperature in forming gas or depositing a strained layer on the backside to pull the wafer flat [29, 59]. However, for fear of damaging the sensitive dielectric layer, such processes are not pursued in this thesis.

Other than flatness, we identify two other main criteria for a suitable bottom substrate. The first is that the breakdown strength of the gate-dielectric must be high enough to withstand voltages of upwards of 100 V. The second is that the substrate must be free of dust or contaminates, such that no spurious particles lie in between the top and bottom samples, further offsetting the vacuum gap. The graphene samples investigated here are quite large, 15 mm $\times$ 20 mm, and the dielectric must be free of pin holes as well as remain dust-free over that entire area.

We next investigate the dielectric breakdown of thermal oxide wafers grown on silicon from three sources. The first two are from collaborators within the Light Material Interactions - Energy Frontier Research Center, and the third is commercially purchased. For each wafer, a piece is cleaved, approximately the size of the final sample, and a gold top electrode is deposited on the surface. To avoid potentially shorting around the side of the wafer, the edges are masked before deposition

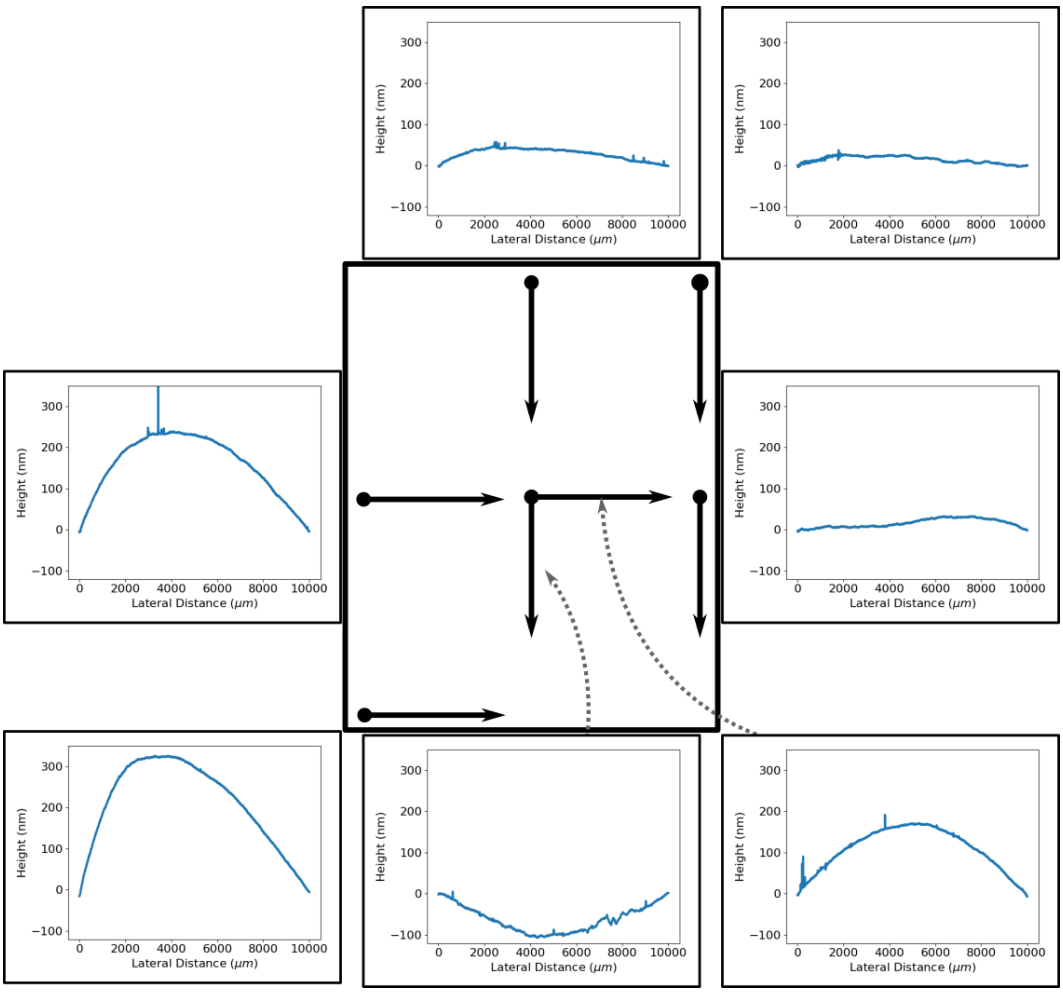

Figure 4.16: Wafer profiles at different points on the wafer. The profiles begin at each black dot and proceed in the direction of the arrow. Unless indicated by the grey arrows, the profilometry plots are positioned adjacent to the their respective start locations. In the "East-West" direction, the wafer bows concave down. In the "North-South" direction, the wafer is much flatter or even concave up. The wafer inhomogeneity cannot be corrected for fear of damaging the layer of SiO_2.

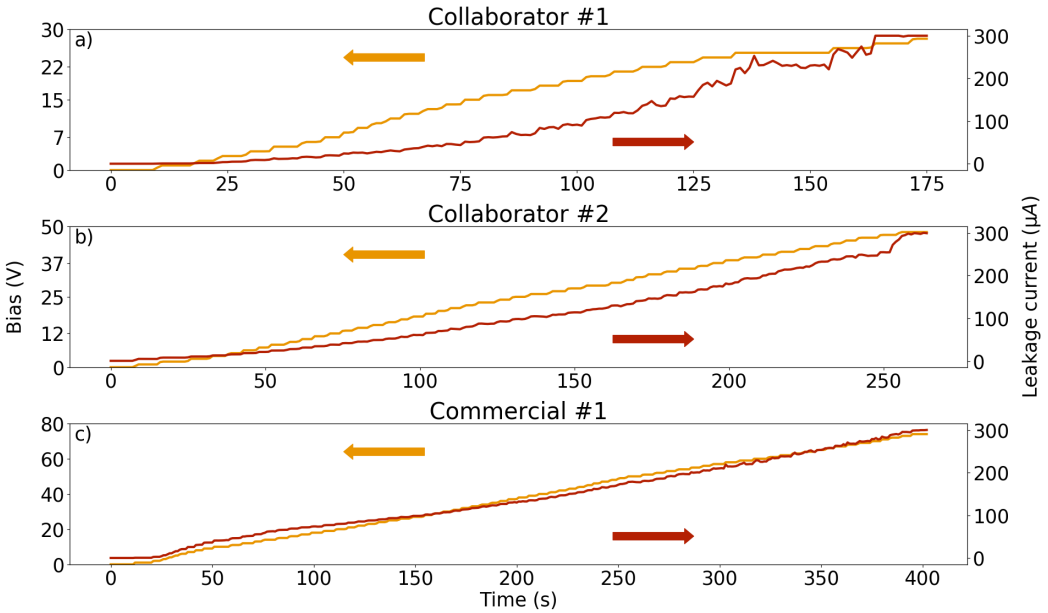

Figure 4.17: Initial thermal oxide wafer tests from three wafer sources. It is best for the leakage current to remain below 1 μA at 100 V bias. In all three cases, the leakage current is too high by over two orders of magnitude.

with Kapton tape. Wire leads are bonded to the top Au and bottom silicon electrodes. The bare silicon is exposed by scratching through the oxide with a diamond scribe. Shown in Figure 4.17, for all three wafers, the leakage current through the wafer is measured in time as a voltage is applied across the oxide.

A satisfactory gate dielectric would allow for peak bias over 100 V with leakage current below 1 μA. As is evident in all three of these tests, the dielectric quality is not adequate to support large area samples. The leakage currents are simply too high. There are two reasons often associated with high leakage currents in capacitive devices like these. The first is that the deposited top electrode is covering a pinhole through the dielectric, and there is a direct short to the bottom electrode. The second is that the dielectric is actually breaking down, and impurities are acting as nucleation sites for growing failure points, through which the current can penetrate the dielectric. The impurity concentration can be reduced by additional processing like additional annealing in forming gas and chlorination. However, to reduce the number of pinholes, they simply need to be filled with an additional captivation layer. For the next oxide wafer tests, we use a different commercial substrate that includes these extra processing steps, and we also grow an additional 8 nm captivation layer

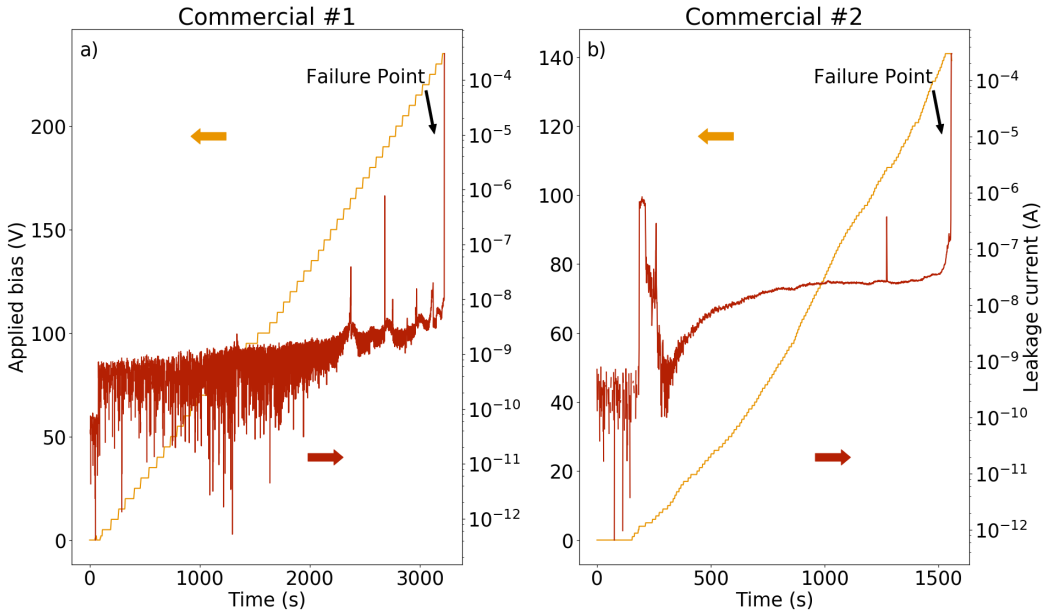

Figure 4.18: Test of gate dielectric layer with captivation layer of Al_2O_3 with two commercial sources. Dielectric breakdown occurs at the failure point where the current jumps over 3 orders of magnitude. For both commercial suppliers with the added layer of Al_2O_3, the breakdown voltage exceeds 100 V.

of Al_2O_3 by atomic layer deposition (ALD). A similar study is repeated, comparing the new commercial wafers to the old commercial wafers, both with the additional captivation layer. In these experiments, the top electrode is a layer of graphene instead of Au. As shown in Figure 4.18, there is a clear performance improvement with the added captivation layer. The leakage currents at high voltages are in the nA regime instead of 100s of microvolts, and the breakdown voltage failure point is well in excess of 100 V. Hence, all thermal oxide wafers receive an additional 8 nm layer of ALD Al_2O_3.

The ALD machine is located outside the clean room, and dust is a constant battle in near field heat transfer measurements. After deposition of Al_2O_3, all subsequent fabrication processes are conducted in a clean room, and the wafers are cleaned by the following a rigorous protocol.

1. As the thermal oxide alone is not sufficient as a gate-dielectric, grow 8 nm of Al_2O_3 on wafer by atomic layer deposition.

2. Scribe wafer into pieces 24.5 mm x 31.75 mm in size. Then sonicate pieces in isopropyl alchohol for ten minutes and blow dry

3. Clean in oxygen plasma at 150W for 60 minutes

4. Soak overnight in piranha solution. This is as much to remove organic material as it is to chemically treat the substrate surface. The piranha helps the graphene film to better adhere to the substrate during the transfer process.

Transfer Protocol

Techniques for transferring CVD graphene from the Cu foil, on which it is grown, to a separate substrate are well established, even for large area samples [135]. However, these techniques generally employ either a spoon or a wafer to pick up the graphene from the Cu etchant bath and move it to a series of water baths. The samples in this thesis need to be 15 mm x 20 mm in size, which was found to be too large to use a spoon, and using a wafer, which requires constant transferring of the graphene film on and off the wafer surface caused undue wear and tear. In this section, we detail a protocol to transfer large area graphene films onto a substrate with minimal contact that requires only a modified separatory funnel as shown in Fig. 4.19.

1. Fill up funnel with ferric chloride copper etchant, then angle funnel to easily place copper foil on the liquid surface. A photo showing the floating copper foil is shown in Figure 4.20.

2. While the funnel is still angled, open the stopcock to drain some of the etchant to be saved for later use. Ferric chloride can be reused a number of times before it becomes ineffective.

3. Then *slowly* add DI water through the snorkel. As the water mixes into the solution, the ferric chloride falls to the bottom of the funnel, causing turbulence which can disturb the graphene. Keeping the funnel angled was found to minimize the disturbance.

4. Iteratively add DI water and empty the funnel until the sample has been adequately washed. The whole cleaning procedure takes about 45 minutes to one hour.

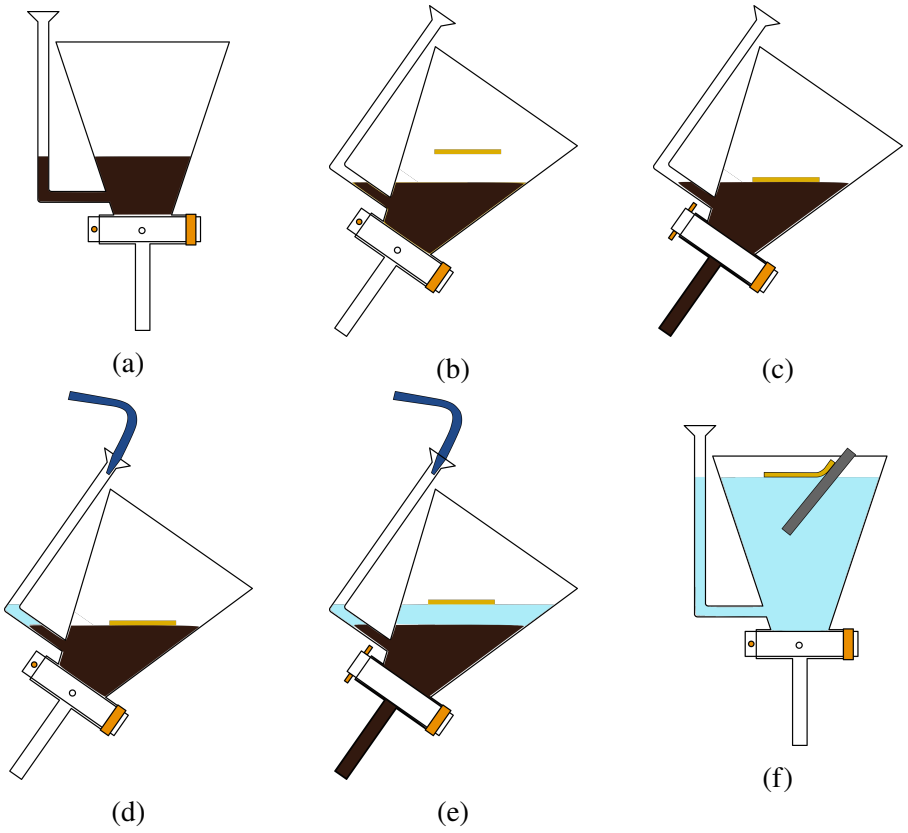

Figure 4.19: Technique for transferring graphene from Cu foil to a substrate. (a) Fill funnel with Cu etchant. (b) Tilt funnel and drop Cu foil onto etchant surface. (c) After etchaing, open stopcock to drain etchant partially. (d) Displace etchange with DI water. (e) Open stopcock again to drain etchant/water mixture. Repeat steps d and e until only DI water remains in funnel. (f) With clean substrate, pull floating graphene from water surface.

5. Using a clean substrate sample (see cleaning procedure), pick up the float graphene film and place on a luke warm hot plot to dry overnight.

The graphene transfer process is identical for transferring to the thermal oxide wafer or to the optical flat. Once transferred to the the optical flat, the top sample requires no further processing other than removing the layer of PMMA by soaking in acetone. For the bottom sample, however, after graphene has been transferred to the thermal oxide, additional bonding constants and silica posts must be deposited.

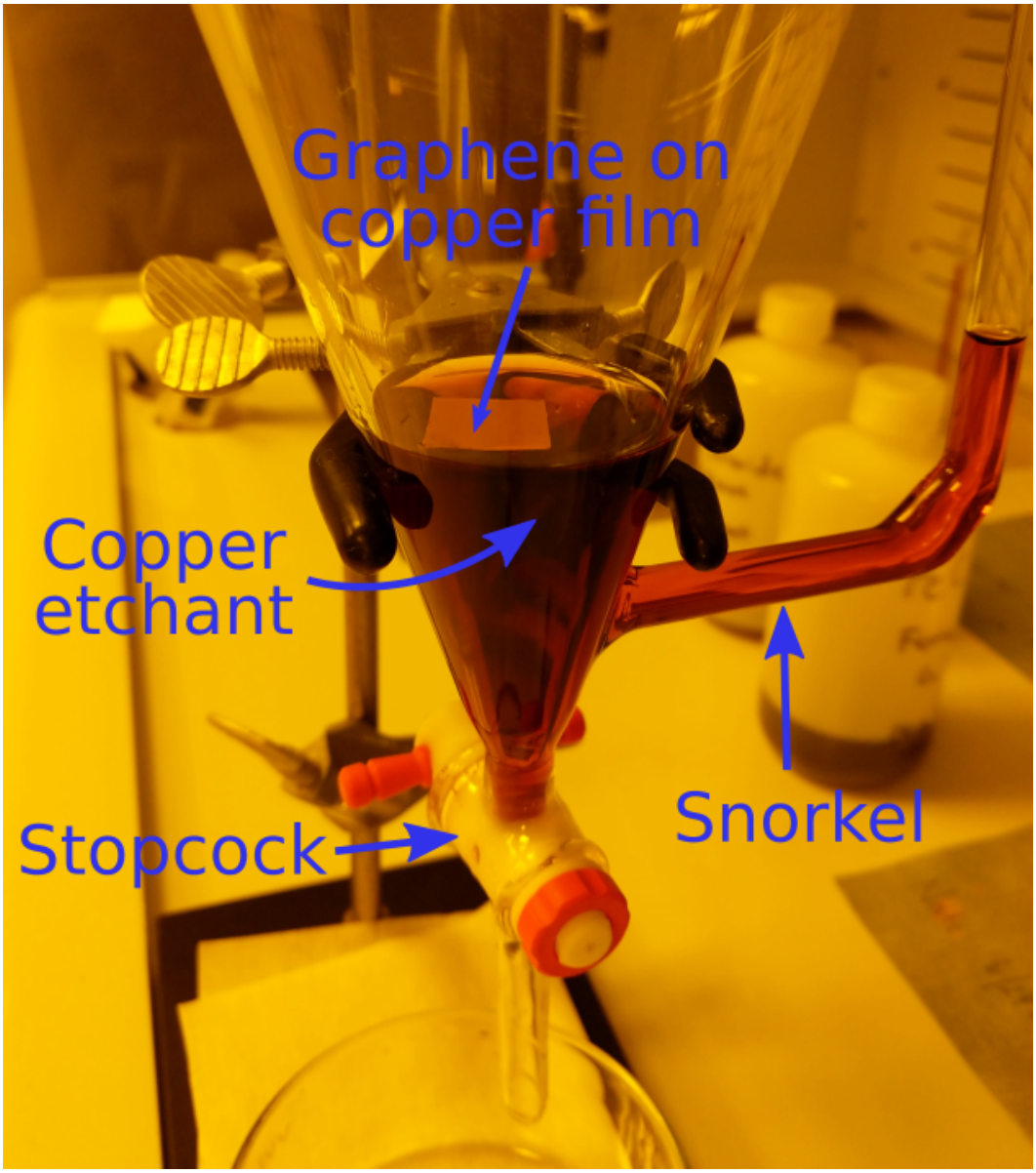

Figure 4.20: Photo of graphene on copper foil floating in copper etchant. After the copper is etched away, the funnel is drained partially by opening the stopcock, and DI water is dispensed through the snorkel.

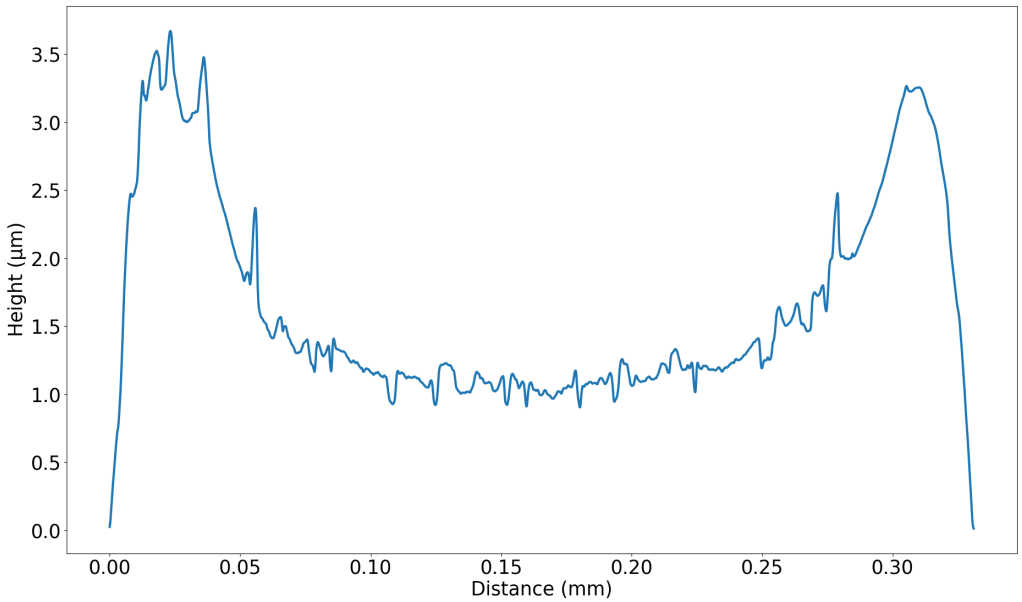

Figure 4.21: Profile of bead ring

Vacuum Spacers and Bonding Contacts

Dispersing polystyrene nanobeads on the sample surface is one standard method for separating the top and bottom samples in near field heat transfer experiments [27, 38]. The beads have low thermal conductivity and allow for negligible levels of conductive thermal leakage. They are initially suspended in a concentrated solution, which requires being diluted many times. However, it was found in this thesis that the beads tend to agglomerate and form a "coffee ring" pattern even after substantial dilution. A cross section profile of one of the rings, shown in Figure 4.21, indicates clear ridges that can extend over 3 μm high, while the beads are only 100 nm in diameter. As the water droplet in which they are suspended evaporates, flow from the interior to the edge of the drop pulls the beads to the edge [136]. Hence, the beads accumulate in certain areas on the sample surface and are not dispersed uniformly. The spacer heights are therefore much higher and more inhomogeneous than desired.

Deposited pillars of SiO_2 or resist are a second technique for separating the top and bottom samples [29, 32, 59]. Typically, these posts are leftover from etched resist or if they are made of SiO_2, micromachined or etched from a layer grown by chemical vapor deposition. It was found in this thesis that the resist thickness fluctuates over

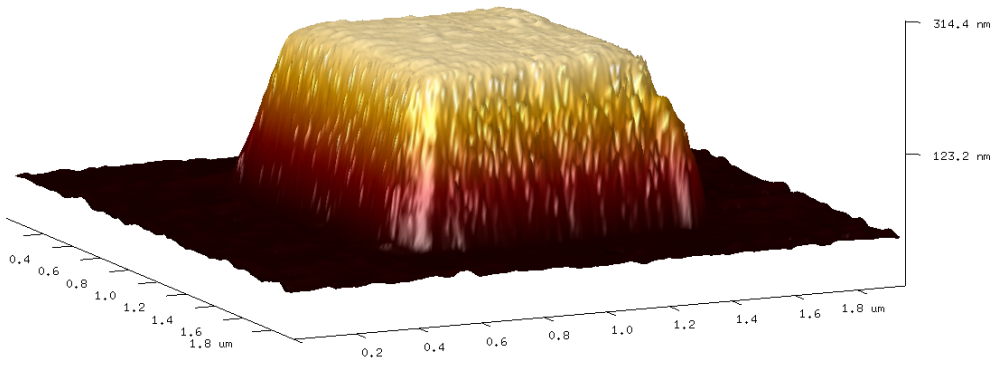

Figure 4.22: Single Post of SiO_2 by electron beam lithography and electron beam deposition

the wafer after spin-coating, so pillars of resist could potentially vary in height across the sample. And subtracting fabrication techniques for creating posts of SiO_2 that require etching of the oxide pose potential risk for the graphene and the underlying gate dielectric. As a result, posts of SiO_2 are grown here additively by standard electron beam lithography followed by electron beam deposition. A 3D rendering by atomic force microscopy of a test sample post is shown in Figure 4.22. In this case, the post measures to be about 250 nm tall, and future growth times were reduced proportionally. Profilometry confirmed subsequent posts are 207 ± 3 nm. Gold bonding contacts were fabricated in a preceeding step also by electron beam lithography.

4.6 Conclusion

In this chapter, the development of an apparatus to measure heat flux modulation by applied bias was discussed, followed by the fabrication protocol to construct the sample recommended from our theoretical discussion in Chapter 3. Critical to measurement accuracy is the precise calibration of the heat flux sensor as well as the careful tracking of all background heat flows in and out of the heat flux sensor. An adequate methodology to create a gate dielectric of sufficient breakdown strength was developed with a new technique to transfer graphene to larger substrates. These two advancements allowed us to create robust, large samples that can be used to measure near field heat flux modulation with this setup. Analysis of four samples is discussed in Chapter 5.

Chapter 5

REALIZATION OF ELECTROSTATIC MODULATION OF HEAT TRANSFER

This chapter has been adapted in part from:

Nathan H. Thomas, Michelle C. Sherrott, Jeremy Broulliet, Harry A. Atwater, and Austin J. Minnich. Electronic Modulation of Near Field Radiative Transfer in Graphene Field Effect Heterostructures. *In preparation*, 2019

5.1 Introduction

Chapter 3 covers the theoretical underpinnings of the experiment and the sample to measure heat flux modulation with changing graphene Fermi level. Chapter 4 focuses on the apparatus with which to demonstrate it. In this chapter, we report the experimental modulation of radiative heat flow by external gating of a graphene field effect heterostructure. As mentioned in Chapter 3, the top is a graphene-coated silica optical flat, and the bottom consists of graphene transferred to a silicon substrate with a gate dielectric of 285 nm of thermal oxide and an 8 nm captivation layer of Al_2O_3. A rendering of the sample configuration is shown again in Figure 5.1. The bias is imposed across the bottom substrate, while the heat flux is simultaneously measured.

5.2 Heat Flux Modulation in Time

To perform the experiment, once the sample is loaded onto the sample stage and the cryostat is pumped down to a pressure of 1×10^{-6} Torr, the temperature of the cold finger is cooled with liquid nitrogen. The equilibrium temperature of the base sample reaches between 86 K and 91 K. After the base reaches equilibrium, the heater is set to a predetermined value that is limited by an upper threshold of the heater input power. The maximum temperature is therefore dependent on the cooling power into the cold finger or more specifically the liquid nitrogen flow rate. Once the peak temperature gradient is achieved and the heat flux sensor has equilibrated, the voltage ramp is applied. For all samples tested here, we find that after a few

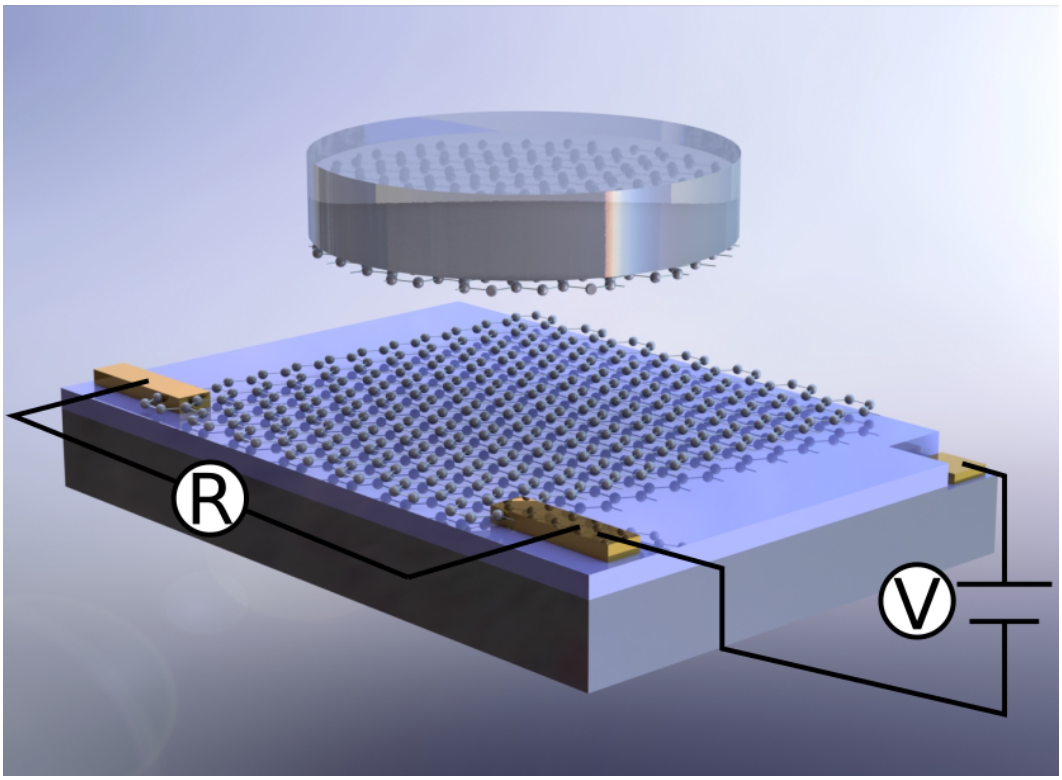

Figure 5.1: Schematic of sample. The bias is imposed across the bottom sample.

ramping cycles the gate dielectric breaks down, limiting the amount of data that can be obtained for each sample.

Figures 5.2a-c show the measured heat flux versus time for three separate samples S1, S2, and S3. The heater-base temperature difference is 111 °C for S1 and is 180 °C for S2 and S3, which is why the heat flux values for S1 are substantially lower. For each sample, we observe a reversible change in the measured heat flux as the bias is ramped up and down. The magnitude of the modulation is around 0.5%, 0.3%, 0.2%, respectively. For samples S2 and S3, this effect is observed for multiple cycles. As a non-negligible thermal capacitance exists, there is a time delay from when the bias is applied and when the heat flux change is observed. For each sample, this delay is about 3 minutes. All samples are first ramped down to -100 V, which results in an observable change in heat flux. For S2, the bias is ramped twice before sample failure. For S3, three cycles are possible, and the third ramp cycle is to a positive bias of +95 V.

A similar magnitude of heat flux change is observed for the positive bias as the negative biases. This result is expected because the graphene is slightly p-type with the charge neutral point found to be slightly positive, between +5 V and +15 V. As a

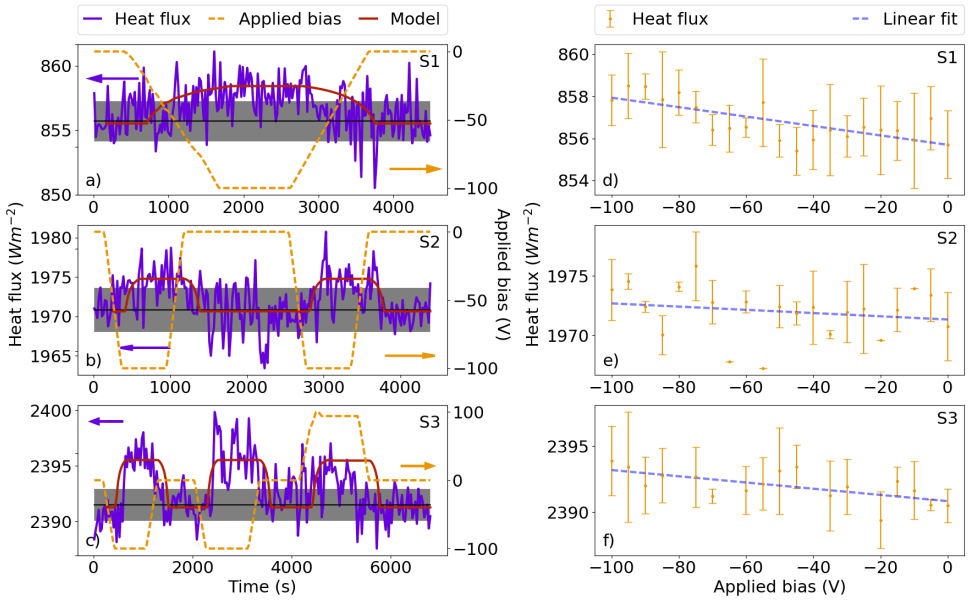

Figure 5.2: (a-c) Heat flux (purple), applied bias (orange dotted), and thermal model (red) versus time for three samples S1, S2, and S3, respectively. The black and grey lines indicate the mean and standard deviation of the signal at zero bias. d-f) Heat flux versus the applied bias using data from Figures 2 a-c. The linear fit (blue dotted lines) indicate the greatest heat flux change is demonstrated in S3, for which the modulation is 24 ± 7 mWm^{-2}.

negative bias is applied, the hole concentration increases, the Fermi level decreases, and the radiative thermal conductance increases. Applying a positive bias of +95 V versus a negative bias of -100 V results in a a Fermi level of 0.29 eV instead of -0.32 eV, which is not sufficiently different in magnitude for a measurable change in heat flux considering the signal noise.

From these data, we compute the heat flux versus electrostatic bias, shown in in Figs. 5.2d-f, for samples S1-S3, respectively. In each case, a linear fit is applied and a modest slope is visible, with the largest modulation exhibited in S3 with a slope of 24 ± 7 mWm^{-2} per V bias.

To interpret these measurements and to further verify that they originate from electrostatic tuning of the Fermi level, we construct a thermal model. The heat flux measured in the experiment as a function of time consists of radiative flux and parasitic conductive losses:

$$Q_{tot}(t-\tau) = G(T_1 - T_2) + Q_{rad}(\mu, d, T_1, T_2). \tag{5.1}$$

The time lag τ between the start of the voltage ramp and when the heat flux sensor registers the flux change is an adjustable parameter, which as mentioned before is about 3 minutes for all samples. The first term on the right accounts for the physical contact of the top and bottom surfaces with a conductance G. The second term, Q_{rad}, is the radiative heat flux between the planar surfaces from Equation 3.7. Since the top and bottoms samples are likely in physical contact, it is assumed that the top and bottom graphene sheets are shorted such that $\mu_1 = \mu_2 = \mu$. There ultimately 5 parameters to determine: μ, T_1, T_2, d, and G. To obtain the Fermi level, μ, we use a parallel-plate capacitor model and the measured applied bias after having found the graphene charge neutral point V_{cnp}. The charge neutral point is the voltage at which the graphene carrier concentration is minimized and the surface resistance is maximized (see Figures 5.3d-f). The surface charge density of the graphene n relates to the applied voltage V by $n = c|V - V_{cnp}|$, where $c = \epsilon/l$ is the area normalized capacitance for a parallel-plate capacitor, and ϵ and l are dielectric constant and thickness, respectively[1]. The graphene Fermi level μ is proportional to $\sqrt{n}$. As a result, the Fermi level relates to the applied voltage by $\mu \propto \sqrt{|V - V_{cnp}|}$.

The temperatures of the heat flux sensor and the heater are measured in the experiment. To determine the temperatures of the graphene surfaces, T_1, and T_2, we employ a thermal resistor model using our knowledge of the heat flux. To first approximation, we assume that the thermal resistance between top and bottom samples is much greater than that between the bottom sample and the copper heat spreader. As the bottom sample substrate is silicon, which has a comparatively high thermal conductivity, the bottom graphene surface temperature is approximately equal to that of the heat flux sensor. For the top sample, we determine the temperature drop across the optical flat by computing the thermal resistance with the thermal conductivity of silica and the optical flat dimensions.

Shown in Figures 5.3a-c, we use optical interferometric measurements to estimate the gap distance d. The measurements are taken at multiple points around the optical flat to determine uniformity in the vacuum gap. These results are tabulated

[1] As the graphene band structure is symmetric, we do not make a distinction between p-type and n-type carriers, as that simply calls for a sign change in Fermi level

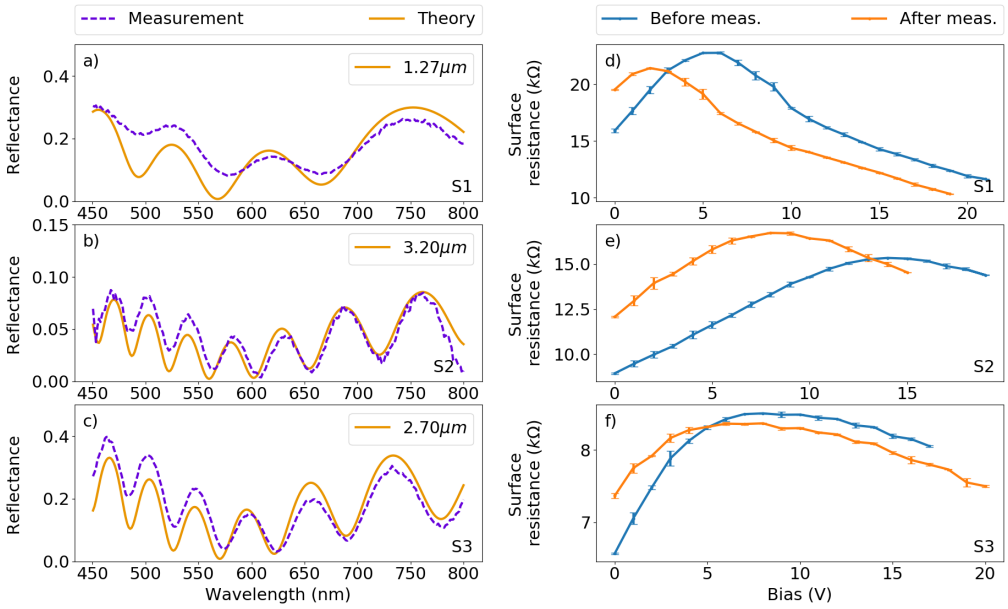

Figure 5.3: Measurements of model parameters for samples S1, S2, and S3, respectively. (a-c) Interferometric measurements for sample gap spacing. A transfer matrix model with a variable gap spacing and amplitude is fit to the measured signal. (d-f) Measurements of graphene surface resistance versus applied bias. The peak in the surface resistance is the charge neutral point where the graphene Fermi level is near zero.

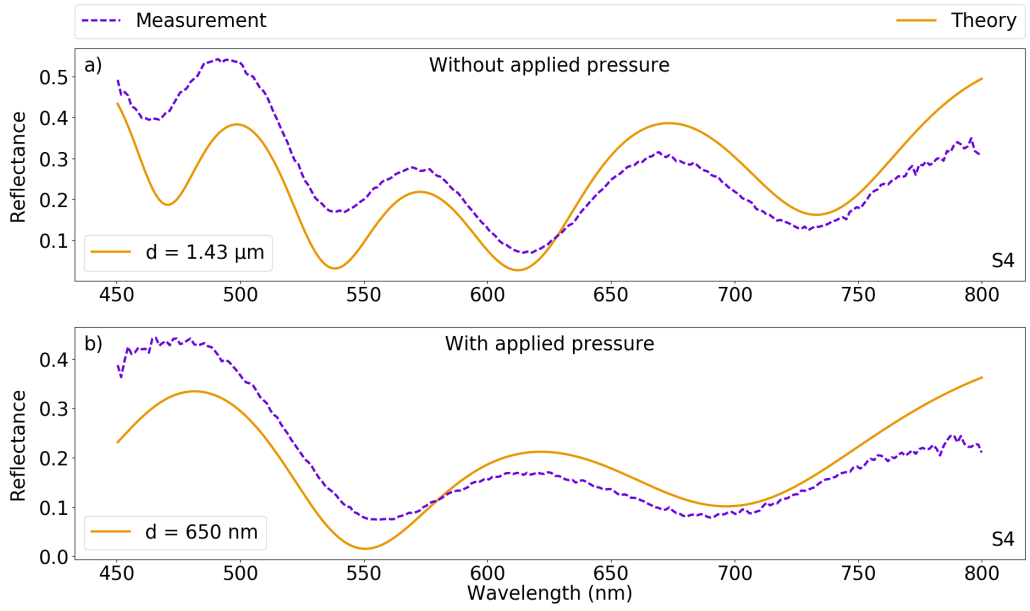

Figure 5.4: Effect of applying pressure. By pressing down on the optical flat during measurement, the gap spacing decreases by over 50%. As the sample is compressed during the heat flux measurements and the interferometric measurements are taken without such added pressure, the measured values of d in Table 5.1 serve as an upper bound.

	S1	S2	S3	S4
#1	5.63 μm	3.20μm	2.46μm	1.43μm
#2	1.28 μm	4.08μm	2.70μm	0.65μm*
#3	3.74 μm	3.45μm	2.31μm	

Table 5.1: Vacuum gap distances for each sample. The sample S1-3, the points were taken at different points around the optical flat. For sample S4, the samples were taken when pressure was applied (indicated by the *), and when no pressure was applied.

in Table 5.1. The distance is quite variable for S1, indicating there is likely a piece of dust beneath the optical flat, causing it to be cantilevered. For S3 the spacings are uniform and close to the distance that gives the appropriate level of heat flux modulation. However, for S2 the gap spacing as measured are about 1 μm larger than expected. During the heat flux measurement, the spring loaded heater presses the optical flat to the underlying substrate, and in an analogous experiment by simply pressing on the sample with tweezers, applying pressure was found to reduce the spacing by upwards of 50%, as shown for Sample S4 in Figure 5.4. As a result, the gap spacing measurements only provide an upper limit on the gap spacing at a particular point on the sample since the spacing is highly dependent on applied pressure.

We conduct a separate heat flux measurement without spacers to estimate the value of the parasitic conductance G, shown in Figure 5.5. Although there is some non-linearity in the heat flux data, a linear fit indicates an upper limit on G to be 17.32 $\mathrm{Wm^{-2}K^{-1}}$. The interface conductance is often found to be an order of magnitude higher between interfaces with applied thermal grease, indicating there is substantial spatial separation here between the top and bottom samples [32]. We attribute the separation to wafer bow and surface residue remaining from sample processing.

As these measurements for d and G only provide an estimate, the final values for each sample are obtained in two independent fitting procedures. First, d is determined from the measured heat flux change because the absolute heat flux change is only a function of gap distance (see Figure 5.6). Second, G is obtained by computing the discrepancy between the measured total heat flux and calculated radiative fluxes for the given gap distance. This discrepancy was found to be 731 ± 9, 1590 ± 30, and 2011 ± 20 $\mathrm{Wm^{-2}}$ for samples S1-S3, respectively, indicating that parasitic

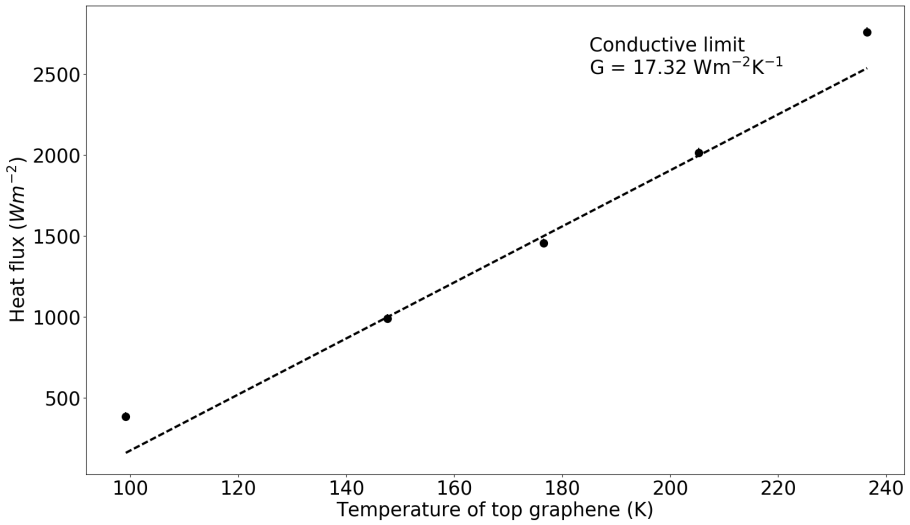

Figure 5.5: Heat flux versus temperature on sample without SiO_2 spacers. Upper limit of heat transfer coefficient for the samples studied here is 17.32 $Wm^{-2}K^{-1}$.

conduction is responsible for 85 ± 1, 81 ± 1, and 84.1 ± 0.6 %, respectively, of the total heat flux. The final parameter values for are tabulated in Table 5.3.

Mentioned briefly in Section. 4.4, the heat flux signal is found to exhibit a linear drift at the tail end of the asymptotic signal equilibration. To account for this drift, we fit a line to the raw heat flux signal at all times when zero bias is applied and then subtract off the slope × time, as shown in Figure 5.7. This effectively rotates the heat flux values down about time $t = 0$, and as a result reduces the final heat flux values by 8 Wm^{-2} for sample S1 and 5 Wm^{-2} for samples S2 and S3.

We next assess the measurement uncertainty and the ratio of signal to noise. First, we isolate the parts of the data that constitute the heat flux baseline at zero bias and the heat flux signal while under bias, shown in Figure 5.8a-c. The heat flux data under bias are collected after the signal has equilibrated up until the start of the voltage ramp back to zero. The data for the third voltage cycle of sample S3 are not included as the dielectric has started to break down. For each interval, we plot the

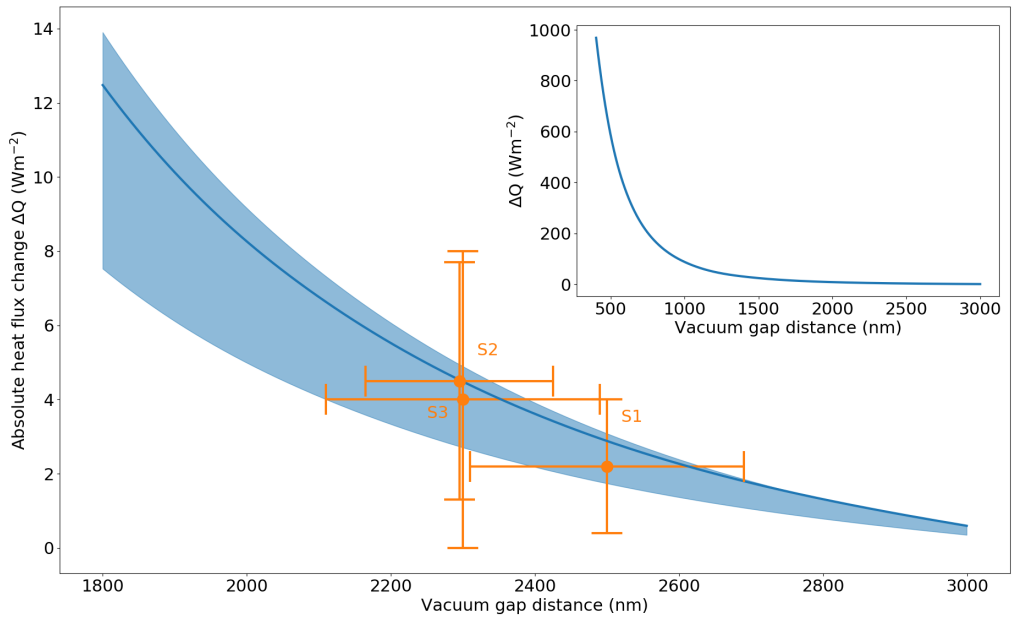

Figure 5.6: Heat flux change due to Fermi level change versus vacuum gap distance. The Fermi level sweeps between 0.05 eV to 0.30 eV (blue line), where the shaded region outlines the heat flux change accounting for the uncertainty in the Fermi level of ±0.05 eV. The vertical error bars for each sample indicate the uncertainty in heat flux measurement, and the horizontal error bars indicate the uncertainty in the solved distance d. The inset shows the heat flux change at distances from 400 nm to 3 μm.

signal to noise ratio

$$SNR = \frac{\overline{HF(-100\ V)} - \overline{HF(0\ V)}}{\sqrt{\sigma^2_{HF(-100\ V)} + \sigma^2_{HF(0\ V)}}} \tag{5.2}$$

in Figure 5.8d. In all cases, the signal to noise ratio is greater than one, indicating the heat flux modulation depth is greater than one standard deviation.

Having established the uncertainty in the measured heat flux change for each sample, $\sigma_{\Delta Q} = \sqrt{\sigma^2_{HF(-100\ V)} + \sigma^2_{HF(0\ V)}}$, we can further propagate errors to estimate the uncertainty in the fitted vacuum gap distance d. As stated in Equation 5.1, the radiative heat flux Q_{rad} is a function of four variables, d, μ, T_1, T_2. The measured heat flux change ΔQ due to the applied bias is

$$\Delta Q = Q_{rad}(d, \mu_1, T_1, T_2) - Q_{rad}(d, \mu_2, T_1, T_2), \tag{5.3}$$

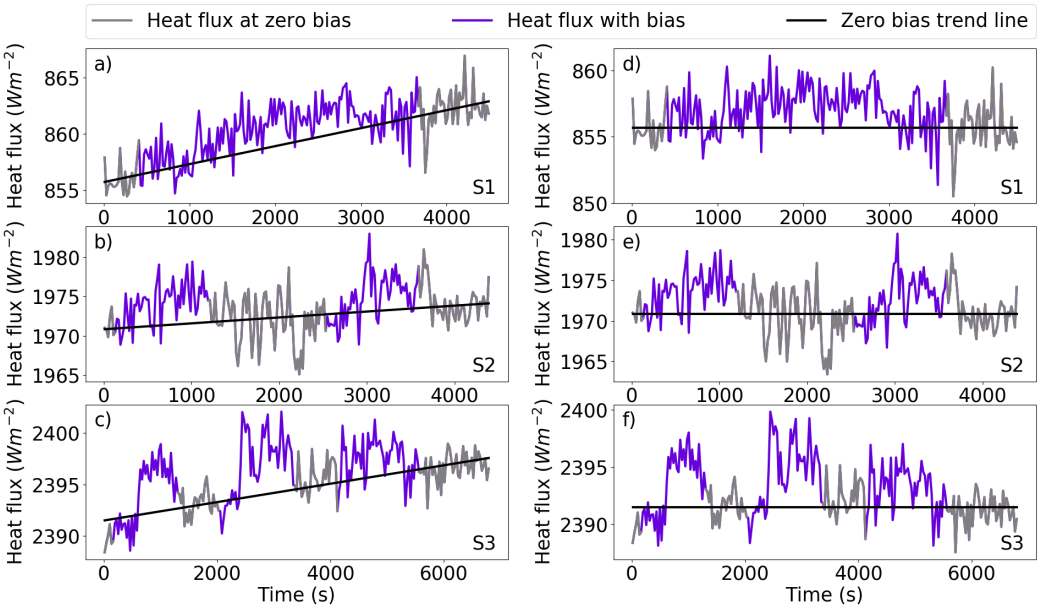

Figure 5.7: Signal drift correction for S1-S3 top to bottom respectively. The raw data are shown on the left. A line is fit to the subset shown in gray at which zero bias is applied. The drift is removed by then subtracting off the slope×time from the entire data set.

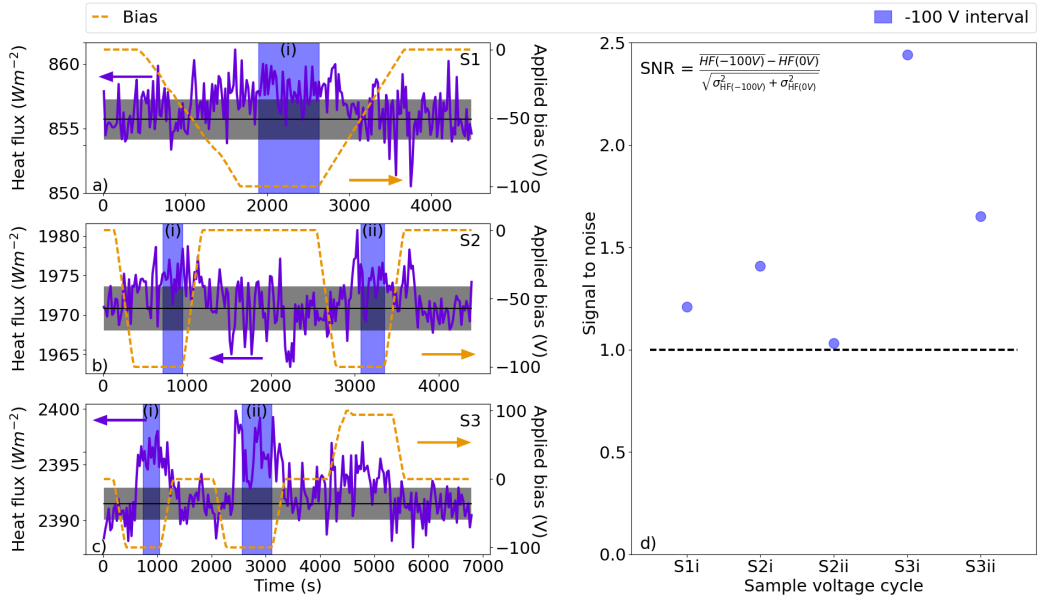

Figure 5.8: Signal to noise ratio for each sample and voltage cycle. (a - c) Heat flux measurements under bias for samples S1-S3, respectively. The collected signal data are indicated in the blue intervals. The zero bias baseline is shown in grey. As S3 begins to breakdown during the third voltage cycle, that cycle is not included in this analysis. (d) The signal to noise ratio for the 5 collection intervals.

	S1i	S2i	S2ii	S3i	S3ii
d (μm)	2.5	2.3	2.3	2.3	2.3
σ_d (nm)	190	130	190	80	130

Table 5.2: Vacuum gap distance and uncertainty for each sample and each voltage cycle. The final cycle for S3 is excluded as the dielectric has started to break down.

where μ_1 and μ_2 are the Fermi levels for the sample under a bias of -100 V and under zero bias, respectively. The uncertainty in the heat flux change $\sigma_{\Delta Q_{rad}}$ is therefore

$$\sigma_{\Delta Q_{rad}} = \sqrt{\sum_n \left(\frac{\partial \Delta Q_{rad}}{\partial n}\right)^2 \sigma_n^2}, \tag{5.4}$$

where $n \in [d, \mu_1, \mu_2, T_1, T_2]$. Therefore, the uncertainty in the vacuum distance is

$$\sigma_d = \sqrt{\frac{\sigma_{\Delta Q_{rad}}^2 - \sum_{n \neq d} \left(\frac{\partial \Delta Q_{rad}}{\partial n}\right)^2 \sigma_n^2}{\left(\frac{\partial \Delta Q_{rad}}{\partial d}\right)^2}}, \tag{5.5}$$

where $n \in [\mu_1, \mu_2, T_1, T_2]$. As the transmissivity function Φ is only weakly dependent on temperature, we can approximate the partial derivative with respect to temperature as

$$\left(\frac{\partial \Delta Q_{rad}}{\partial T_{1,2}}\right)^2 = \left(\int \frac{\omega}{2\pi} \frac{\partial \Theta(T,\omega)}{\partial T}\Big|_{T_1,T_2} [\Phi(\omega, \mu_1, d) - \Phi(\omega, \mu_2, d)] \right)^2. \tag{5.6}$$

The other partial derivatives we compute numerically from a 2-D lookup table generated with Equations 3.6, 3.7, and 3.8. The uncertainty in each of the Fermi levels, σ_{μ_1} and σ_{μ_2}, is 0.05 eV, and the uncertainty in each of the temperature values T_1 and T_2 is 2 K. Computing each of these partial derivatives numerically, we get the uncertainty in the distance values d, shown in Table 5.2.

Having accounted for all modeling parameters and systematic trends in the heat flux measurements, one final effect must be considered before comparing the model with the measurements. As the graphene samples have large area, around 15 mm $\times$ 20 mm, the graphene may short to the underlying silicon through a pinhole in the thermal oxide. Although we added an additional 8 nm layer of Al_2O_3 by atomic layer deposition (ALD) to reduce this possibility, any impurities within the dielectric or additional surface blemishes can act as nucleation sites for dielectric breakdown.

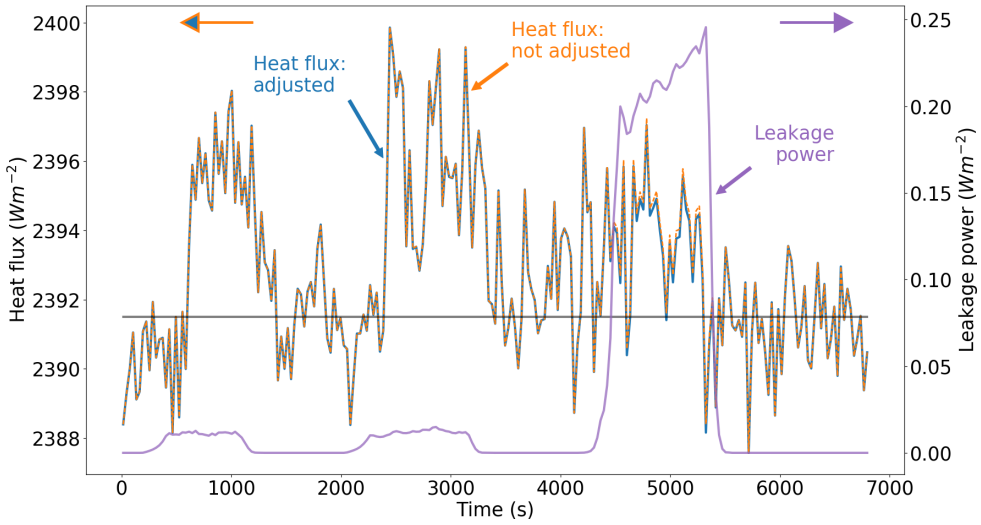

Figure 5.9: Leakage power over time. The final jump in leakage power corresponds to when the sample was forward biased to 95 V. In this case, the leakage power is 20 times larger than in the previous two times, however the change in heat flux is not significantly different from the previous -100 V cases considering the signal noise.

As the dielectric breaks down, current flows and Joule heating occurs, potentially contributing to the measured heat flux. To mitigate this Joule heating contribution, we continually monitor the leakage current to ensure that it does not exceed 350 nA for these three samples, yielding a maximum Joule heating power of 0.26 Wm^{-2}. The observed heat flux change is about 5 Wm^{-2} in all cases, or nearly 20 times higher than the injected Joule heat. For each measurement, we subtract the area normalized injected power $P = IV$. We also confirm independently that the injected Joule heat is not the cause of the modulated signal. As shown in Figure 5.9, for S3, the leakage power was approximately 20 times higher for the positive bias case to +95 V versus the two previous cases to -100 V. If the injected Joule heating were the source of the heat flux change, then the modulation for the +95 V case would have been 20× higher than in the -100 V case but as shown in Fig. 5.2 the heat flux change was nearly identical.

The model predictions are plotted in Figs. 5.2a-c and agree well with the measured heat flux. For samples S1-S3, the fitted values for G are 6.6 ± 0.2, 8.9 ± 0.2, and 11.3 ± 0.2 $\mathrm{Wm}^{-2}\mathrm{K}^{-1}$, respectively, and for d are 2.5 ± 0.2, 2.3 ± 0.2, and 2.3 ± 0.13

	S1	S2	S3	S4
G ($Wm^{-2}K^{-1}$)	6.59	8.88	11.20	5.10
d (μm)	2.5	2.3	2.3	0.56
T_1 (K)	197	270	269	-
T_2 (K)	86	91	90	-
CNP (V)	5	15	7	-

Table 5.3: Fitting parameters for the model in Equation 5.1. The temperatures are taken from measurement, accounting for the thermal resistance of the optical flat. The charge neutral point (CNP) is the voltage at which the graphene surface resistance is maximized and the Fermi level is near zero.

microns, respectively. These values are tabulated in Table 5.3 along with heater and sample base temperatures, T_1 and T_2 respectively. The thermal conductance value indicates non-negligible physical contact between the optical flat and the bottom substrate. The fitted value for vacuum gap separation indicate a vacuum gap commensurate with previous near field heat transfer experiments [38]. After the initial time delay, the heat flux increases to its steady-state value, and then decreases to the equilibrium value, following the measured heat flux. During the final, third voltage ramp for S3, there is a slight deviation from the model at later stages when the peak voltage of +95 V was applied. We attribute this discrepancy to the sample dielectric beginning to break down, indicated by the rise in leakage power, shown in Figure 5.9, which decreases the electric field effect and subsequently lowers the Fermi level compared to that used in the model.

With the model and the fitted gap distances, we can also estimate the absolute radiative heat flux between the two surfaces. Subtracting the conductive contribution, we find the radiative heat flux for S1 is 125 ± 9 Wm^{-2}, exceeding the black body limit of 84 ± 4 Wm^{-2} by 50 ± 10%. For samples S2 and S3, the thermal emitter is 80 K hotter than for S1, and the radiative heat flux is 385 ± 26 Wm^{-2} and 381 ± 18 Wm^{-2} for S2 and S3, respectively. Sample S2 exceeds the black body limit of 299 ± 9 Wm^{-2} by 29 ± 7%, and sample S3 exceeds the black body limit of 295 ± 9 Wm^{-2} by 29 ± 9%. These results confirm that the radiative transport is in the near-field regime.

5.3 Heat Flux Modulation vs Temperature

Measurements of heat flux in time are useful for determining the cyclic nature of the heat flux modulation, however they are conducted only at a single set of temperatures for T_1 and T_2. To examine modulation trends with temperature, we next present the

heat flux versus hot side temperature for sample S4 for two different biases, as shown in Fig 5.10a. The heat flux is first measured at zero bias and then at -35 V. Additional measurements at temperature below the third point at 175 K were not possible due to dielectric breakdown as the leakage current exceeded 2 μA. For all measurements, the cold side temperature T_2 is again held between 86 K and 91 K. We again interpret these results using the model described previously, where here we fit for G, d, and μ.

In this case, the charge neutral point could not be found under forward bias, as dielectric breakdown occurred at smaller biases than for the previous samples. Weak dielectric breakdown strength is also why the applied negative bias is limited to -35 V. While the Fermi level is therefore a fitting parameter, the previous three samples do provide an approximate range for the charge neutral point (see Figure 5.3). The highest V_{cnp} was 15 V for S2, which corresponds to a zero bias Fermi level of -0.12 eV. Here, for S4, the best fit zero bias Fermi level is -0.20 eV, or $V_{cnp} \sim 40$ V, which although higher, is sufficiently close to the V_{cnp} values of the previous three samples. Using the fitting parameters from the zero bias data, we then apply a zero-parameter fit for the measurement under bias, accounting for the change in Fermi level. The model shows good agreement with the measured heat flux.

In Figure 5.10b, the data are normalized to the dotted blue fit. Point to point variation in both signals is evident, but there is also a clear trend that heat flux in the biased case is greater than that in the zero bias case by around 3-5%. At 175 K, where both the biased and zero bias case were measured and a more direct comparison is possible, the heat flux change is 4 ± 3%.

5.4 Conclusion

Although the modulation reported here is small, as expected due to the micron-scale gap spacing, improvements to the experimental setup should allow for modulation values approaching 100%. First, the gate dielectric must exhibit high breakdown strength approaching that of bulk SiO_2 while also exhibiting warping less than 100 nm over the substrate area. These qualities would allow for larger changes in bias, and hence Fermi level, and a smaller vacuum gap. Typical methods to alter wafer bow and warp like applying a back-layer of oxide [29] or annealing at high temperature [59] are not possible due to potential damage to the dielectric that

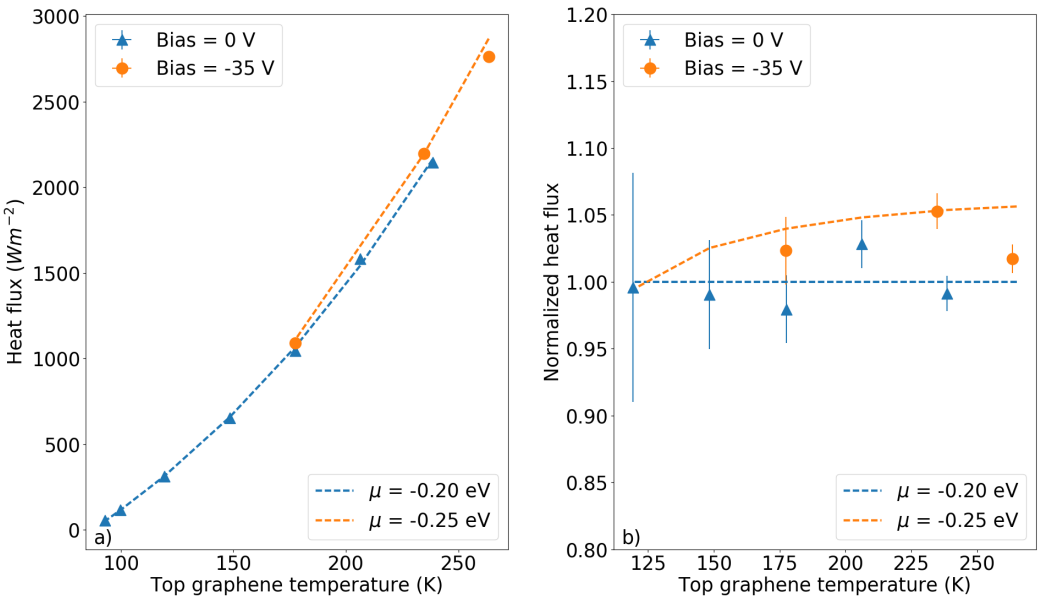

Figure 5.10: a) Measured heat flux versus temperature for sample S4 for 0 V (blue triangles) and -35 V (orange cicles). The blue dotted line is a fit of Eq. 5.1 to the blue data points, for which d = 560 nm, G = 5.07 Wm^{-2}, and $\mu = -0.20\ eV$. The orange line is a zero parameter fit, using the these values and a Fermi level of $\mu = -0.25\ eV$ corresponding to the -35 V bias. b) Normalized heat flux versus temperature for the two biases. The heat flux under bias is around 5% greater than the zero bias case.

leads to breakdown. We found the wafers could not be flipped due to the risk of scratching the surface and creating additional pinholes. Hence, experiments with smaller emitter areas are advantageous as they lead to reduced effects of warp and a lower probability of shorting through a pinhole.

We also found that typical methods to remove organic residue from the graphene following transfer were not suitable as they would also strip the graphene. The additional processing of creating the array of SiO_2 pillars and Au bonding contacts had the side effect of adding additional resist residue to the surface that could not be removed. We attribute this added residue as well as wafer surface warp as to why the vacuum gap spacing is large ($> 2\ \mu m$ in most cases). Recent advances in nano-manipulation of wafers would remove the need for added processing, and they report gap spacing well below 200 nm [35, 134]. By eliminating all conductive losses and reducing the gap spacing to 100 nm, biasing to -100 V as in these experiments would result in a heat flux modulation of 100%. However, even reducing the gap to 500 nm without any change in the interface conductance would lead to modulation of 45%.

In summary, we reported the observation of the modulation of near-field thermal

radiation by electrostatic gating of graphene devices. The maximum measured modulation was 4 ± 3% and the maximum measured modulation rate was 24 ± 7 mWm^{-2} per V bias. This work demonstrates that two-dimensional materials can be used to electrostatically control near-field radiative transfer and provides a path for realizing thermal switches with modulation depth approaching 100%.

Chapter 6

CONCLUSION AND OUTLOOK

In this thesis, we investigated avenues for controlling the radiative flow of heat by both passive and active means. In the passive case, where the radiative properties remain unchanged after fabrication, we designed, fabricated, and tested a semiconductor dielectric selective surface with ultra-low thermal emittance for photothermal energy conversion of non-concentrated sunlight.

Modern methods for using sunlight for thermal applications often require geometric concentrators. These concentrators require potentially large and valuable areas of land, and as they cannot focus diffusely scattered sunlight, they are also limited in their efficiency. To reach temperatures close to 400°C, relevant for many industrial processes, with non-concentrated sunlight requires a selective absorber with high solar absorptance and ultra-low thermal emittance, for which a semiconductor-dielectric tandem is well suited.

In this thesis, we integrated Ge and CaF_2 into a multilayer stack that maintained 74% solar absorptance after multiple field tests and 5% thermal emittance. We demonstrated peak temperature of 225 °C in the field, with the vacuum chamber window absorbing nearly half of the incident radiation. With a standard 92% transmissive window, we predict a steady-state temperature of 280 °C. From simulation, we also determined the temperature dependent thermal emittance approaches 13%, indicating the importance of measuring selective surfaces at operating conditions. Alternative, calorimetric techniques to measure temperature dependent solar absorptance and thermal emittance have also been developed [82].

Although a peak temperature over 300 °C was not realized, this work validates employing low bandgap semiconductors for solar thermal absorption, particularly when geometric concentration is not feasible. To enhance future performance and higher stagnation temperatures, improved deposition of infrared transparent dielectrics films is critical. Techniques like ion-assisted electron beam deposition have been shown to create dense films of CaF_2, for example [137]. Also, as temperatures rise, material stability will be an important factor. Mixing of Si and Ge could potentially lead to higher operational temperatures. Amorphous silicon has been shown to be stable up to 500 °C [71, 138, 139]. Although mixing amorphous Si

with amorphous Ge will increase the band gap and potentially lower solar absorptance, the altered and possibility spatially varying refractive index can allow for enhanced anti-reflection. Further enhancement to temperature stability, could also be realized be depositing crystalline layers of Ge under optimal conditions [140]. Such improvements would extend semiconductor materials for use in photothermal conversion of non-concentrated sunlight for small-scale process heat.

To better compare selective solar thermal technologies to one another in the long run, standard evaluation procedures like those in place for solar cells, should be implemented. Although off-angle FTIR spectra like those used in this thesis are necessary for visualizing optical properties, measuring the temperature dependent solar absorptance and hemispherically averaged thermal emittance offers complete sample characterization. Temperature stability of these two values will ultimately determine implementation flat panel solar thermal absorbers for industrial process heat. As the optical properties for selective surfaces improve, continued thermal testing will be necessary in order to predict projected lifetime.

In the active case of controlling thermal radiation, we demonstrated for the first time the modulation of near-field radiative heat flow by electrostatic biasing of a graphene field effect device over multiple voltage cycles. We observed a reversible change in heat flux over multiple ramping cycles as well as the heat flux modulation over multiple temperatures. The maximum measured modulation was 4 ± 3% and the maximum measured modulation rate was 24 ± 7 $\mathrm{mWm^{-2}}$ per V bias. Modern heat switches often require mechanical components that are slow and prone to failure. These results can potentially lead to high-speed, solid-state thermal switches.

The modulation depth from these experiments was around 4 $\mathrm{Wm^{-2}}$, limited by the large gap spacing between the top and bottom samples due to wafer warp and resist residue. These obstacles can be surpassed with different substrate materials and an alternative sample geometry. To continue using large scale graphene samples for large signal response, a geometry like that used in Ghashami et al. with fused silica wafers would work well [134]. As the top and bottom substrates are independently suspended, silica post fabrication would not be necessary. Moreover, if the metallic leads were pre-fabricated on the substrate before graphene transfer, then no lithography on the graphene would be necessary. More aggressive resist developers could be used, which would reduce the amount surface residue. As the top and bottom substrates would also be independently actuated, the graphene-to-graphene contact resistance could be a metric to determine sample contact, ensuring zero parasitic

conductive heat flow through the heterostructure.

To use a silica wafer as the substrate, however, a back electrode and a gate dielectric would need to deposited. Deposited SiO_2 alone does not function well on its own as a gate dielectric as there are too many pinholes and impurities. Additional captivation layers grown by ALD of high dielectric materials like HfO_2 and Al_2O_3 are likely necessary. Deposited films tend to be rougher than the underlying polished substrate. As the graphene mobility drops when transferred to a rough surface, continual care for the surface roughness will need to be maintained.

There are considerable advantages in going to smaller scale. The likelihood of encountering a pinhole in the dielectric goes down with the graphene area. Also, the wafer bow and warp is less pronounced with a smaller substrate. As a result, miniature versions of the heterostructures studied in this thesis with active area on the order of 1 mm^2 would be well suited for future thermal modulation studies. Additional care should be given to the sample holder design, as the spring-loaded resistive heater used in this thesis is likely too bulky for smaller, more fragile heterostructures. Custom resisitive temperature sensors for measuring the top and bottom temperatures will also provide flexibility in sample design. In this thesis, we found it prohibitively difficult to find a commercial sensor that is both small operates near liquid nitrogen temperatures.

Nanofabricated samples and an experimental setup like those in Song et al. which were used to measure near field radiative heat transfer between a film and a coated mesa would also work well [110]. Although these structures are not scalable to much greater than 100's of μm on a side, the reported gap distances are so low that enhanced heat flux modulation is likely. In these systems, the mesa is already coated with deposited layers of Au or SiO_2. Graphene could potentially be transferred to such a mesa with pre-fabricated metallic leads.

In cases where the dielectric would need to be fabricated, atomic layer deposition of oxides will be necessary for fabrication of a high quality gate dielectric layer. Distributed layers of alternating dielectrics can produce additional hyperbolic bands that contribute to heat flux [141]. Theoretical work similar to that in Chapter 3 in this thesis will be necessary to determine optimal layer thicknesses.

An additional area to pursue would be switching speed. Due to the large thermal capacitance and the delicate gate-dielectrics in this thesis, the heat flux change and voltage ramp rate were quite slow. One advantage radiative thermal switches that

function by external bias have over other technologies is their potential to operate very quickly. Graphene based optical modulators have been shown to function in the GHz regime [142, 143]. However, to measure heat flux variation that fast will require temperature measurement devices with low thermal load. Lock-in techniques to isolate the signal from noise could also prove useful.

Ultimately, the switching ratio will be the biggest factor in implementing radiative thermal modulators. Using patterned resonators could provide enhanced modulation depths beyond what is possible with simple planar structures [118]. Although difficult, developing new dielectrics and patterned structures could greatly enhance radiative thermal switching.

Appendix A

TRANSFER MATRIX METHOD

We start with modeling the reflection and transmission of light at a single interface, like that shown in Fig. with the interface at $z = z_0$. Maxwell's Equations in SI units are

$$\nabla \cdot \boldsymbol{D} = \rho_f, \quad \nabla \cdot \boldsymbol{B} = 0, \quad \nabla \times \boldsymbol{E} = -\frac{\partial \boldsymbol{B}}{\partial t}, \quad \nabla \times \boldsymbol{H} = \left(\boldsymbol{J}_f + \frac{\partial \boldsymbol{D}}{\partial t}\right), \tag{A.1}$$

where $\boldsymbol{D} = \epsilon\epsilon_0\boldsymbol{E}$, $\boldsymbol{B} = \mu\mu_0\boldsymbol{H}$, and we assume ohmic materials such that $\boldsymbol{J}_f = \sigma\boldsymbol{E}$, where σ is the conductivity. In the above relation, ϵ_0 and μ_0 are the permittivity and permeability of free space; ϵ and μ are the relative permittivity and permeability, respectively. As is the case for most dielectrics, we assume the relative permeability to be 1, and the charde density ρ_f to be 0. The permittivity is a uniaxial tensor defined below. Hence, the final two equations above (the Maxwell-Faraday Law and Ampère's Law) reduce to

$$\nabla \times \boldsymbol{E} = -\frac{\partial \boldsymbol{B}}{\partial t}, \quad \nabla \times \boldsymbol{B} = \mu\mu 0 \overleftrightarrow{\boldsymbol{\epsilon}} \epsilon_0 \frac{\partial \boldsymbol{E}}{\partial t}. \tag{A.2}$$

More concisely,

$$\nabla \times \boldsymbol{E} = -\frac{\partial \boldsymbol{B}}{\partial t}, \quad \nabla \times \boldsymbol{B} = \frac{\mu \overleftrightarrow{\boldsymbol{\epsilon}}}{c^2} \frac{\partial \boldsymbol{E}}{\partial t}. \tag{A.3}$$

For our system, we consider a uniaxial relative permittivity tensor:

$$\overleftrightarrow{\boldsymbol{\epsilon}} = \begin{pmatrix} \epsilon_{xx} & 0 & 0 \\ 0 & \epsilon_{xx} & 0 \\ 0 & 0 & \epsilon_{zz} \end{pmatrix} \tag{A.4}$$

We assume harmonic solutions to the **E** and **B** fields in both time and space, such that

$$\boldsymbol{E}(\boldsymbol{r}, t) = \left(E_x\hat{\boldsymbol{x}} + E_y\hat{\boldsymbol{y}} + E_z\hat{\boldsymbol{z}}\right) e^{i\boldsymbol{k}\cdot\boldsymbol{r} - i\omega t} \tag{A.5}$$

$$\boldsymbol{B}(\boldsymbol{r}, t) = \left(B_x\hat{\boldsymbol{x}} + B_y\hat{\boldsymbol{y}} + B_z\hat{\boldsymbol{z}}\right) e^{i\boldsymbol{k}\cdot\boldsymbol{r} - i\omega t}. \tag{A.6}$$

Note on notation: Often a source of confusion in derivations like this is that the variables for field amplitudes E_x, E_y, E_z and B_x, B_y, B_z are used for both the *invariant* amplitude in the plane wave form of the field like $\boldsymbol{E}(\boldsymbol{r}, t) = (E_x\hat{\boldsymbol{x}} + E_y\hat{\boldsymbol{y}} + E_z\hat{\boldsymbol{z}})\, e^{i\boldsymbol{k}\cdot\boldsymbol{r} - i\omega t}$,

as well as for the *function* of space and time like $\boldsymbol{E}(\boldsymbol{r},t) = E_x(\boldsymbol{r},t)\hat{\boldsymbol{x}} + E_y(\boldsymbol{r},t)\hat{\boldsymbol{y}} + E_z(\boldsymbol{r},t)\hat{\boldsymbol{z}}$. To avoid such confusion, in this thesis the script form of the letter represents the function component of the field, and the plain text letter represents the invariant field amplitude. Hence,

$$\begin{aligned}\boldsymbol{E}(\boldsymbol{r},t) &= \left(E_x\hat{\boldsymbol{x}} + E_y\hat{\boldsymbol{y}} + E_z\hat{\boldsymbol{z}}\right)\ e^{i\boldsymbol{k}\cdot\boldsymbol{r}-i\omega t} = \left(\mathcal{E}_x(\boldsymbol{r},t)\,\hat{\boldsymbol{x}} + \mathcal{E}_y(\boldsymbol{r},t)\,\hat{\boldsymbol{y}} + \mathcal{E}_z(\boldsymbol{r},t)\,\hat{\boldsymbol{z}}\right)\\ \boldsymbol{B}(\boldsymbol{r},t) &= \left(B_x\hat{\boldsymbol{x}} + B_y\hat{\boldsymbol{y}} + B_z\hat{\boldsymbol{z}}\right)\ e^{i\boldsymbol{k}\cdot\boldsymbol{r}-i\omega t} = \left(\mathcal{B}_x(\boldsymbol{r},t)\,\hat{\boldsymbol{x}} + \mathcal{B}_y(\boldsymbol{r},t)\,\hat{\boldsymbol{y}} + \mathcal{B}_z(\boldsymbol{r},t)\,\hat{\boldsymbol{z}}\right).\end{aligned} \tag{A.7}$$

This is important when calculating derivatives because $\forall\ i, j \in [x, y, z]$,

$$\frac{\partial}{\partial i}E_j = 0 = \frac{\partial}{\partial i}B_j, \tag{A.8}$$

however

$$\frac{\partial}{\partial i}\mathcal{E}_j \neq 0 \neq \frac{\partial}{\partial i}\mathcal{B}_j. \tag{A.9}$$

A.1 TM Polarized Light - Single Interface

In the coordinate system indicated in Fig. xx, the transverse magnetic polarized light is defined where $B_x = B_z = 0$ and $E_y = 0$. We rewrite the fields as a superposition of forward and backforward propagating components. Moreover, the in-plane components $\left(k_x, k_y\right)$ of the wave-vector $\boldsymbol{k}$ are unchanged by reflection and refraction. Hence, the fields can be rewritten as

$$\begin{aligned}\boldsymbol{B}(\boldsymbol{r},t) &= B_y\hat{\boldsymbol{y}}e^{i\boldsymbol{k}\cdot\boldsymbol{r}-i\omega t}\\ &= \left(B_y e^{ik_z z} + B'_y e^{-ik_z z}\right)\hat{\boldsymbol{y}}e^{i(k_x x+k_y y)-i\omega t}\end{aligned} \tag{A.10}$$

$$\begin{aligned}\boldsymbol{E}(\boldsymbol{r},t) &= \left(E_x\hat{\boldsymbol{x}} + E_z\hat{\boldsymbol{z}}\right)\ e^{i\boldsymbol{k}\cdot\boldsymbol{r}-i\omega t}\\ &= \left[\left(E_x\hat{\boldsymbol{x}} + E_z\hat{\boldsymbol{z}}\right)e^{ik_z z} + \left(E'_x\hat{\boldsymbol{x}} + E'_z\hat{\boldsymbol{z}}\right)e^{-ik_z z}\right]e^{i(k_x x+k_y y)-i\omega t}.\end{aligned} \tag{A.11}$$

Apply and Simplify Maxwell's Equations

Applying the second equation in Eq.A.3 (Ampère's Law) and taking the curl of the $\boldsymbol{B}$ field, we get

$$\nabla\times\boldsymbol{B}(\boldsymbol{r},t) = \begin{vmatrix}\hat{\boldsymbol{x}} & \hat{\boldsymbol{y}} & \hat{\boldsymbol{z}}\\ \frac{\partial}{\partial x} & \frac{\partial}{\partial y} & \frac{\partial}{\partial z}\\ \boldsymbol{B}(\boldsymbol{r},t)\cdot\hat{\boldsymbol{x}} & \boldsymbol{B}(\boldsymbol{r},t)\cdot\hat{\boldsymbol{y}} & \boldsymbol{B}(\boldsymbol{r},t)\cdot\hat{\boldsymbol{z}}\end{vmatrix} \tag{A.12}$$

$$\nabla\times\boldsymbol{B}(\boldsymbol{r},t) = \begin{vmatrix}\hat{\boldsymbol{x}} & \hat{\boldsymbol{y}} & \hat{\boldsymbol{z}}\\ \frac{\partial}{\partial x} & \frac{\partial}{\partial y} & \frac{\partial}{\partial z}\\ 0 & \left(B_y e^{ik_z z} + B'_y e^{-ik_z z}\right)e^{i(k_x x+k_y y)-i\omega t} & 0\end{vmatrix} \tag{A.13}$$

$$\begin{aligned}\nabla \times \boldsymbol{B}(\boldsymbol{r},t) = \hat{\boldsymbol{x}}&\left(-\frac{\partial}{\partial z}\left(B_y e^{ik_z z} + B'_y e^{-ik_z z}\right) e^{i(k_x x + k_y y) - i\omega t}\right) \\ &+ \hat{\boldsymbol{z}}\left(\frac{\partial}{\partial x}\left(B_y e^{ik_z z} + B'_y e^{-ik_z z}\right) e^{i(k_x x + k_y y) - i\omega t}\right)\end{aligned} \tag{A.14}$$

$$\begin{aligned}\nabla \times \boldsymbol{B}(\boldsymbol{r},t) = \hat{\boldsymbol{x}}&\left(-ik_z B_y e^{ik_z z} + ik_z B'_y e^{-ik_z z}\right) e^{i(k_x x + k_y y) - i\omega t} \\ &+ \hat{\boldsymbol{z}}\left(ik_x\left(B_y e^{ik_z z} + B'_y e^{-ik_z z}\right) e^{i(k_x x + k_y y) - i\omega t}\right).\end{aligned} \tag{A.15}$$

Given the harmonic nature of the E field, the other side of Eq. A.3 is

$$\begin{aligned}\frac{\overleftrightarrow{\epsilon}\mu}{c^2}\frac{\partial \boldsymbol{E}}{\partial t} &= -i\omega\frac{\overleftrightarrow{\epsilon}\mu}{c^2}\boldsymbol{E} \\ &= -i\omega\frac{\overleftrightarrow{\epsilon}\mu}{c^2}\left[\left(E_x\hat{\boldsymbol{x}} + E_z\hat{\boldsymbol{z}}\right)e^{ik_z z} + \left(E'_x\hat{\boldsymbol{x}} + E'_z\hat{\boldsymbol{z}}\right)e^{-ik_z z}\right]e^{i(k_x x + k_y y) - i\omega t} \\ &= -i\omega\frac{\overleftrightarrow{\epsilon}\mu}{c^2}\left[\hat{\boldsymbol{x}}\left(E_x e^{ik_z z} + E'_x e^{-ik_z z}\right)\right. \\ &\qquad \left. + \hat{\boldsymbol{z}}\left(E_z e^{ik_z z} + E'_z e^{-ik_z z}\right)\right]e^{i(k_x x + k_y y) - i\omega t}\end{aligned} \tag{A.16}$$

$$\begin{aligned}\frac{\overleftrightarrow{\epsilon}\mu}{c^2}\frac{\partial \boldsymbol{E}}{\partial t} = -i\omega\frac{\mu}{c^2}&\left[\hat{\boldsymbol{x}}\epsilon_{xx}\left(E_x e^{ik_z z} + E'_x e^{-ik_z z}\right)\right. \\ &\left. + \hat{\boldsymbol{z}}\epsilon_{zz}\left(E_z e^{ik_z z} + E'_z e^{-ik_z z}\right)\right]e^{i(k_x x + k_y y) - i\omega t}.\end{aligned} \tag{A.17}$$

Equating the vector components of Equations A.15 and A.17, we get for $\hat{\boldsymbol{x}}$ component:

$$\left(-ik_z B_y e^{ik_z z} + ik_z B'_y e^{-ik_z z}\right) = -i\omega\frac{\epsilon_{xx}\mu}{c^2}\left(E_x e^{ik_z z} + E'_x e^{-ik_z z}\right) \tag{A.18}$$

and for $\hat{\boldsymbol{z}}$ component:

$$\left(ik_x\left(B_y e^{ik_z z} + B'_y e^{-ik_z z}\right)\right) = -i\omega\frac{\epsilon_{zz}\mu}{c^2}\left(E_z e^{ik_z z} + E'_z e^{-ik_z z}\right). \tag{A.19}$$

Since the functions, $e^{ik_z z}$ and $e^{-ik_z z}$ are orthogonal, we get the final relations:

$$\begin{aligned}k_z B_y &= \frac{\omega\epsilon_{xx}\mu}{c^2}E_x \\ k_z B'_y &= \frac{-\omega\epsilon_{xx}\mu}{c^2}E'_x \\ k_x B_y &= \frac{-\omega\epsilon_{zz}\mu}{c^2}E_z \\ k_x B'_y &= \frac{-\omega\epsilon_{zz}\mu}{c^2}E'_z.\end{aligned} \tag{A.20}$$

Boundary Conditions

The boundary conditions are that the component of the $\boldsymbol{E}$ field parallel to the incident surface is continuous at the surface, and the discontinuity in the parallel component of the $\boldsymbol{B}$ field relates to the surface current. Given the the surface at the position $z = z0$:

$$\begin{aligned} \boldsymbol{E}(z0)^{(1)} \cdot \hat{\boldsymbol{x}} - \boldsymbol{E}(z0)^{(2)} \cdot \hat{\boldsymbol{x}} &= 0 \\ \frac{1}{\mu^{(1)}\mu_0}\boldsymbol{B}(z0)^{(1)}_{||} - \frac{1}{\mu^{(2)}\mu_0}\boldsymbol{B}(z0)^{(2)}_{||} &= \boldsymbol{J}_f \times \hat{\boldsymbol{n}}, \end{aligned} \tag{A.21}$$

where $\hat{\boldsymbol{n}}$ is the surface normal, $\hat{\boldsymbol{n}} = -\hat{\boldsymbol{z}}$.

Boundary Condition I

The parallel ($\hat{\boldsymbol{x}}$) component of the electric field is

$$\boldsymbol{E}(z0)^{(1)} \cdot \hat{\boldsymbol{x}} = \left(E_x^{(1)} e^{ik_z^{(1)} z0} + E_x'^{(1)} e^{-ik_z^{(1)} z0}\right) e^{i(k_x x + k_y y) - i\omega t}. \tag{A.22}$$

So the critical relation that results from the first boundary condition is

$$E_x^{(1)} e^{ik_z^{(1)} z0} + E_x'^{(1)} e^{-ik_z^{(1)} z0} = E_x^{(2)} e^{ik_z^{(1)} z0} + E_x'^{(1)} e^{-ik_z^{(2)} z0}. \tag{A.23}$$

Boundary Condition II

Since the $\boldsymbol{B}$ field is entirely parallel to the interface, the first term in the second half of Eq. A.21 becomes

$$\begin{aligned} \frac{1}{\mu^{(1)}}\boldsymbol{B}(z0)^{(1)} - \frac{1}{\mu^{(2)}}\boldsymbol{B}(z0)^{(2)} &= -\mu_0\sigma \boldsymbol{E} \times \hat{\boldsymbol{z}} \\ &= -\mu_0\sigma \Bigg[\hat{\boldsymbol{x}} \left(E_x e^{ik_z z} + E_x' e^{-ik_z z}\right) \\ &\qquad + \hat{\boldsymbol{z}} \left(E_z e^{ik_z z} + E_z' e^{-ik_z z}\right) \Bigg] e^{i(k_x x + k_y y) - i\omega t} \times \hat{\boldsymbol{z}} \\ &= \mu_0\sigma \left[\hat{\boldsymbol{z}} \times \hat{\boldsymbol{x}} \left(E_x e^{ik_z z} + E_x' e^{-ik_z z}\right)\right] e^{i(k_x x + k_y y) - i\omega t} \\ &= \mu_0\sigma \left[\hat{\boldsymbol{y}} \left(E_x e^{ik_z z} + E_x' e^{-ik_z z}\right)\right] e^{i(k_x x + k_y y) - i\omega t}. \end{aligned} \tag{A.24}$$

After canceling the exponential terms containing k_x, k_y, and ω, which are invariant along the interface, we end up with the boundary condition,

$$\begin{aligned} \left(\frac{1}{\mu^{(1)}} B_y^{(1)} e^{ik_z^{(1)} z0} + \frac{1}{\mu^{(1)}} B_y'^{(1)} e^{-ik_z^{(1)} z0}\right) - \left(\frac{1}{\mu^{(2)}} B_y^{(2)} e^{ik_z^{(2)} z0} + \frac{1}{\mu^{(2)}} B_y'^{(2)} e^{-ik_z^{(2)} z0}\right) \\ = \mu_0\sigma \left(E_x^{(1)} e^{ik_z^{(1)} z0} + E_x'^{(1)} e^{-ik_z^{(1)} z0}\right). \end{aligned} \tag{A.25}$$

Substituting the terms in Eq. A.20, we get

$$\frac{\omega\epsilon_{xx}^{(1)}}{c^2 k_z^{(1)}} E_x^{(1)} e^{ik_z^{(1)} z0} - \frac{\omega\epsilon_{xx}^{(1)}}{c^2 k_z^{(1)}} E_x'^{(1)} e^{-ik_z^{(1)} z0} - \frac{\omega\epsilon_{xx}^{(2)}}{c^2 k_z^{(2)}} E_x^{(2)} e^{ik_z^{(2)} z0} + \frac{\omega\epsilon_{xx}^{(2)}}{c^2 k_z^{(2)}} E_x'^{(2)} e^{-ik_z^{(2)} z0} = \mu_0\sigma \left(E_x^{(1)} e^{ik_z^{(1)} z0} + E_x'^{(1)} e^{-ik_z^{(1)} z0} \right). \tag{A.26}$$

Simplifying, we get

$$\left(\frac{\epsilon_{xx}^{(1)}}{k_z^{(1)}} - \frac{\sigma\mu_0 c^2}{\omega} \right) E_x^{(1)} e^{ik_z^{(1)} z0} - \left(\frac{\epsilon_{xx}^{(1)}}{k_z^{(1)}} + \frac{\sigma\mu_0 c^2}{\omega} \right) E_x'^{(1)} e^{-ik_z^{(1)} z0} = \frac{\epsilon_{xx}^{(2)}}{k_z^{(2)}} E_x^{(2)} e^{ik_z^{(2)} z0} - \frac{\epsilon_{xx}^{(2)}}{k_z^{(2)}} E_x'^{(2)} e^{-ik_z^{(2)} z0}. \tag{A.27}$$

The definition of c is $c^2 = 1/(\epsilon_0\mu_0)$. Hence, we can simplify Eq. A.27 further and get the main relation from the second boundary condition for TM polarized light at a conductive interface

$$\left(\frac{\epsilon_{xx}^{(1)}}{k_z^{(1)}} - \frac{\sigma}{\omega\epsilon_0} \right) E_x^{(1)} e^{ik_z^{(1)} z0} - \left(\frac{\epsilon_{xx}^{(1)}}{k_z^{(1)}} + \frac{\sigma}{\omega\epsilon_0} \right) E_x'^{(1)} e^{-ik_z^{(1)} z0} = \frac{\epsilon_{xx}^{(2)}}{k_z^{(2)}} E_x^{(2)} e^{ik_z^{(2)} z0} - \frac{\epsilon_{xx}^{(2)}}{k_z^{(2)}} E_x'^{(2)} e^{-ik_z^{(2)} z0}. \tag{A.28}$$

Matrix Formulation

Combining the two critical relations, Eqs. A.23 & A.28 into a single matrix equation results in

$$\begin{bmatrix} e^{ik_z^{(1)} z0} & e^{-ik_z^{(1)} z0} \\ \left(\frac{\epsilon_{xx}^{(1)}}{k_z^{(1)}} - \frac{\sigma}{\omega\epsilon_0} \right) e^{ik_z^{(1)} z0} & -\left(\frac{\epsilon_{xx}^{(1)}}{k_z^{(1)}} + \frac{\sigma}{\omega\epsilon_0} \right) e^{-ik_z^{(1)} z0} \end{bmatrix} \begin{bmatrix} E_x^{(1)} \\ E_x'^{(1)} \end{bmatrix} = \begin{bmatrix} e^{ik_z^{(2)} z0} & e^{-ik_z^{(2)} z0} \\ \frac{\epsilon_{xx}^{(2)}}{k_z^{(2)}} e^{ik_z^{(2)} z0} & -\frac{\epsilon_{xx}^{(2)}}{k_z^{(2)}} e^{ik_z^{(2)} z0} e^{-ik_z^{(2)} z0} \end{bmatrix} \begin{bmatrix} E_x^{(2)} \\ E_x'^{(2)} \end{bmatrix} \tag{A.29}$$

or more concisely,

$$M^{(1)}(z_0, \sigma) \begin{bmatrix} E_x^{(1)} \\ E_x'^{(1)} \end{bmatrix} = M^{(2)}(z_0, \sigma = 0) \begin{bmatrix} E_x^{(2)} \\ E_x'^{(2)} \end{bmatrix}, \tag{A.30}$$

where for layer j,

$$M^j(z, \sigma) = \begin{bmatrix} e^{ik_z^{(j)} z} & e^{-ik_z^{(j)} z} \\ \left(\frac{\epsilon_{xx}^{(j)}}{k_z^{(j)}} - \frac{\sigma}{\omega\epsilon_0} \right) e^{ik_z^{(j)} z} & -\left(\frac{\epsilon_{xx}^{(j)}}{k_z^{(j)}} + \frac{\sigma}{\omega\epsilon_0} \right) e^{-ik_z^{(j)} z} \end{bmatrix}. \tag{A.31}$$

In this system with a single interface, there can be no backwards propagating field in medium 2 because there is no interface off of which the field can reflect. Hence, $E_x'^{(2)} = 0$. We now define the remaining fields in terms of reflection and transmission coefficients, also referred to as the Fresnel coefficients. Because the light is TM polarized, such reflection and transmission coefficients are best defined in terms of the magnetic field amplitude: $H_y'^{(1)} = rH_y^{(1)}$ and $H_y^{(2)} = tH_y^{(1)}$. Using the relations in Eq.A.20, we can define the Fresnel coefficients in terms of the electric fields, $E_x'^{(1)} = -rE_x^{(1)}$ and $E_x^{(2)} = t\frac{\epsilon_{xx}^{(1)}}{\epsilon_{xx}^{(2)}}\frac{k_z^{(2)}}{k_z^{(1)}}E_x^{(1)}$. Substituting these relations into Eq. A.29, we get the final matrix equation,

$$\begin{aligned}&\begin{bmatrix} e^{ik_z^{(1)}z0} & e^{-ik_z^{(1)}z0} \\ \left(\frac{\epsilon_{xx}^{(1)}}{k_z^{(1)}} - \frac{\sigma}{\omega\epsilon_0}\right)e^{ik_z^{(1)}z0} & -\left(\frac{\epsilon_{xx}^{(1)}}{k_z^{(1)}} + \frac{\sigma}{\omega\epsilon_0}\right)e^{-ik_z^{(1)}z0} \end{bmatrix}\begin{bmatrix} 1 \\ -r \end{bmatrix} \\ &= \begin{bmatrix} e^{ik_z^{(2)}z0} & e^{-ik_z^{(2)}z0} \\ \frac{\epsilon_{xx}^{(2)}}{k_z^{(2)}}e^{ik_z^{(2)}z0} & -\frac{\epsilon_{xx}^{(2)}}{k_z^{(2)}}e^{ik_z^{(2)}z0}e^{-ik_z^{(2)}z0} \end{bmatrix}\begin{bmatrix} t\frac{\epsilon_{xx}^{(1)}}{\epsilon_{xx}^{(2)}}\frac{k_z^{(2)}}{k_z^{(1)}} \\ 0 \end{bmatrix}.\end{aligned} \tag{A.32}$$

Solving for r and t, we get the standard Fresnel relations:

$$r_{TM} = e^{2ik_{z_1}z0}\frac{\epsilon_{xx}^{(2)}k_z^{(1)} - \epsilon_{xx}^{(1)}k_z^{(2)} + \frac{\sigma k_z^{(1)}k_z^{(2)}}{\omega\epsilon_0}}{\epsilon_{xx}^{(2)}k_z^{(1)} + \epsilon_{xx}^{(1)}k_z^{(2)} + \frac{\sigma k_z^{(1)}k_z^{(2)}}{\omega\epsilon_0}} \tag{A.33}$$

and

$$t_{TM} = e^{i(k_z^{(1)} - k_z^{(2)})z0}\frac{2\epsilon_{xx}^{(2)}k_z^{(1)}}{\epsilon_{xx}^{(2)}k_z^{(1)} + \epsilon_{xx}^{(1)}k_z^{(2)} + \frac{\sigma k_z^{(2)}k_z^{(1)}}{\epsilon_0\omega}}. \tag{A.34}$$

A.2 TE Polarized Light - Single Interface

The derivation in this section follows closely that from Sec. A.1, however the incident fields are different. For TE Polarized light, all vector components of the electric field are zero except for that parallel to the interface.

$$\boldsymbol{E}(\boldsymbol{r},t) = E_y\hat{\boldsymbol{y}}e^{\boldsymbol{k}\cdot\boldsymbol{r}-i\omega t} = \left(E_y e^{ik_z z} + E_y' e^{-ik_z z}\right)\hat{\boldsymbol{y}}e^{i(k_x x + k_y y)-i\omega t} \tag{A.35}$$

$$\begin{aligned}\boldsymbol{B}(\boldsymbol{r},t) = (B_x\hat{\boldsymbol{x}} + B_z\hat{\boldsymbol{z}})\ e^{i\boldsymbol{k}\cdot\boldsymbol{r}-i\omega t} = \Big[&(B_x\hat{\boldsymbol{x}} + B_z\hat{\boldsymbol{z}})\,e^{ik_z z} \\ &+ \left(B_x'\hat{\boldsymbol{x}} + B_z'\hat{\boldsymbol{z}}\right)e^{-ik_z z}\Big]e^{i(k_x x + k_y y)-i\omega t}.\end{aligned} \tag{A.36}$$

Apply and Simplify Maxwell's Equations (Again)

For TM light, the relevant equation was Ampére's Law. For TE light, we instead focus on the Maxwell-Faraday Law

$$\nabla \times \boldsymbol{E} = -\frac{\partial \boldsymbol{B}}{\partial t}. \tag{A.37}$$

Again, the B field is harmonic in time, so the right side of the Maxwell-Faraday Law becomes

$$\begin{aligned}\frac{\partial}{\partial t}\boldsymbol{B} &= i\omega \boldsymbol{B} \\ &= i\omega \left[\left(B_x \hat{\boldsymbol{x}} + B_z \hat{\boldsymbol{z}}\right) e^{ik_z z} + \left(B'_x \hat{\boldsymbol{x}} + B'_z \hat{\boldsymbol{z}}\right) e^{-ik_z z} \right] e^{i(k_x x + k_y y) - i\omega t} \\ &= i\omega \left[\hat{\boldsymbol{x}} \left(B_x e^{ik_z z} + B'_x e^{-ik_z z} \right) + \hat{\boldsymbol{z}} \left(B_z e^{ik_z z} + B'_z e^{-ik_z z} \right) \right] e^{i(k_x x + k_y y) - i\omega t}.\end{aligned} \tag{A.38}$$

On the left side, taking the curl of the E field we get

$$\begin{aligned}\nabla \times \boldsymbol{E}(\boldsymbol{r}, t) = \hat{\boldsymbol{x}} &\left(-\frac{\partial}{\partial z} \left(E_y e^{ik_z z} + E'_y e^{-ik_z z} \right) e^{i(k_x x + k_y y) - i\omega t} \right) \\ &+ \hat{\boldsymbol{z}} \left(\frac{\partial}{\partial x} \left(E_y e^{ik_z z} + E'_y e^{-ik_z z} \right) e^{i(k_x x + k_y y) - i\omega t} \right)\end{aligned} \tag{A.39}$$

$$\begin{aligned}\nabla \times \boldsymbol{E}(\boldsymbol{r}, t) = \hat{\boldsymbol{x}} &\left(-ik_z E_y e^{ik_z z} + ik_z E'_y e^{-ik_z z} \right) e^{i(k_x x + k_y y) - i\omega t} \\ &+ \hat{\boldsymbol{z}} \left(ik_x \left(E_y e^{ik_z z} + E'_y e^{-ik_z z} \right) e^{i(k_x x + k_y y) - i\omega t} \right).\end{aligned} \tag{A.40}$$

Equating the two sides and selecting for each vector component we get the following:

For $\hat{\boldsymbol{x}}$:

$$i\omega \left(B_x e^{ik_z z} + B'_x e^{-ik_z z} \right) = \left(-ik_z E_y e^{ik_z z} + ik_z E'_y e^{-ik_z z} \right) \tag{A.41}$$

For $\hat{\boldsymbol{z}}$:

$$i\omega \left(B_z e^{ik_z z} + B'_z e^{-ik_z z} \right) = ik_x \left(E_y e^{ik_z z} + E'_y e^{-ik_z z} \right). \tag{A.42}$$

Hence, we have the relations:

$$\begin{aligned}\omega B_x &= -k_z E_y \\ \omega B'_x &= k_z E'_y \\ \omega B_z &= k_x E_y \\ \omega B'_z &= k_x E'_y.\end{aligned} \tag{A.43}$$

Boundary Conditions

The boundary conditions are the same for TE light as they are for TM light, however the components parallel and normal to the interface are different. Now the y-component of the E field is parallel to the interface

$$\begin{aligned} \boldsymbol{E}(z0)^{(1)} \cdot \hat{\boldsymbol{y}} - \boldsymbol{E}(z0)^{(2)} \cdot \hat{\boldsymbol{y}} &= 0 \\ \frac{1}{\mu^{(1)}\mu_0}\boldsymbol{B}(z0)^{(1)}_{||} - \frac{1}{\mu^{(2)}\mu_0}\boldsymbol{B}(z0)^{(2)}_{||} &= \boldsymbol{J}_f \times \hat{\boldsymbol{n}}, \end{aligned} \tag{A.44}$$

where $\hat{\boldsymbol{n}}$ is the surface normal, $\hat{\boldsymbol{n}} = -\hat{\boldsymbol{z}}$.

Boundary Condition I

Relating parallel components of the E field is relatively straightforward.

$$\boldsymbol{E}(z0)^{(1)} \cdot \hat{\boldsymbol{y}} = \left(E_y^{(1)} e^{ik_z^{(1)} z0} + E_y'^{(1)} e^{-ik_z^{(1)} z0}\right) e^{i(k_x x + k_y y) - i\omega t} \tag{A.45}$$

$$E_y^{(1)} e^{ik_z^{(1)} z0} + E_y'^{(1)} e^{-ik_z^{(1)} z0} = E_y^{(2)} e^{ik_z^{(2)} z0} + E_y'^{(2)} e^{-ik_z^{(2)} z0}. \tag{A.46}$$

Boundary Condition II

As before, the surface current is related to the electric field by the surface conductivity $\boldsymbol{J_f} = \sigma \boldsymbol{E}$, so the second boundary condition becomes

$$\frac{1}{\mu^{(1)}}\boldsymbol{B}(z0)^{(1)}_{||} - \frac{1}{\mu^{(2)}}\boldsymbol{B}(z0)^{(2)}_{||} = -\sigma\mu_0 \boldsymbol{E} \times \hat{\boldsymbol{z}}. \tag{A.47}$$

The parallel component of the B field is the x component.

$$\boldsymbol{B}(z0)^{(1)}_{||} = \hat{\boldsymbol{x}} \left(B_x^{(1)} e^{ik_z^{(1)} z} + B_x'^{(1)} e^{-ik_z^{(1)} z}\right) e^{i(k_x x + k_y y) - i\omega t}. \tag{A.48}$$

The expression for $-\boldsymbol{E} \times \hat{\boldsymbol{z}}$ is

$$\begin{aligned} -\boldsymbol{E} \times \hat{\boldsymbol{z}} &= \left(E_y e^{ik_z z} + E_y' e^{-ik_z z}\right) (-\hat{\boldsymbol{y}} \times \hat{\boldsymbol{z}})\, e^{i(k_x x + k_y y) - i\omega t} \\ &= \left(E_y e^{ik_z z} + E_y' e^{-ik_z z}\right) (-\hat{\boldsymbol{x}})\, e^{i(k_x x + k_y y) - i\omega t}. \end{aligned} \tag{A.49}$$

Combining Eqs. A.47, A.48, and A.49, we get

$$\begin{aligned} \left(\frac{1}{\mu^{(1)}} B_x^{(1)} e^{ik_z^{(1)} z0} + \frac{1}{\mu^{(1)}} B_x'^{(1)} e^{-ik_z^{(1)} z0}\right) - \left(\frac{1}{\mu^{(2)}} B_x^{(2)} e^{ik_z^{(2)} z0} + \frac{1}{\mu^{(2)}} B_x'^{(2)} e^{-ik_z^{(2)} z0}\right) \\ = -\sigma\mu_0 \left(E_y^{(1)} e^{ik_z^{(1)} z0} + E_y'^{(1)} e^{-ik_z^{(1)} z0}\right). \end{aligned} \tag{A.50}$$

Substituting the amplitude relations in Eq. A.43, we get

$$-\frac{k_z^{(1)}}{\omega\mu^{(1)}}E_y^{(1)}e^{ik_z^{(1)}z0}+\frac{k_z^{(1)}}{\omega\mu^{(1)}}E_y'^{(1)}e^{-ik_z^{(1)}z0}=-\frac{k_z^{(2)}}{\omega\mu^{(2)}}E_y^{(2)}e^{ik_z^{(2)}z0}+\frac{k_z^{(2)}}{\omega\mu^{(2)}}E_y'^{(2)}e^{-ik_z^{(2)}z0} - \sigma\mu_0\left(E_y^{(1)}e^{ik_z^{(1)}z0}+E_y'^{(1)}e^{-ik_z^{(1)}z0}\right), \tag{A.51}$$

which simplifies to

$$\left(-\frac{k_z^{(1)}}{\mu^{(1)}}+\sigma\omega\mu_0\right)E_y^{(1)}e^{ik_z^{(1)}z0}+\left(\frac{k_z^{(1)}}{\mu^{(1)}}+\sigma\omega\mu_0\right)E_y'^{(1)}e^{-ik_z^{(1)}z0} = -\frac{k_z^{(2)}}{\mu^{(2)}}E_y^{(2)}e^{ik_z^{(2)}z0}+\frac{k_z^{(2)}}{\mu^{(2)}}E_y'^{(2)}e^{-ik_z^{(2)}z0}. \tag{A.52}$$

Matrix Formalism

Combining the results from applying the two boundary conditions, Eqs. A.46 and A.52 into a single matrix equation gives

$$\begin{bmatrix} e^{ik_z^{(1)}z0} & e^{-ik_z^{(1)}z0} \\ \left(-\frac{k_z^{(1)}}{\mu^{(1)}}+\sigma\omega\mu_0\right)e^{ik_z^{(1)}z0} & \left(\frac{k_z^{(1)}}{\mu^{(1)}}+\sigma\omega\mu_0\right)e^{-ik_z^{(1)}z0} \end{bmatrix}\begin{bmatrix} E_y^{(1)} \\ E_y'^{(1)} \end{bmatrix} = \begin{bmatrix} e^{ik_z^{(2)}z0} & e^{-ik_z^{(2)}z0} \\ -\frac{k_z^{(2)}}{\mu^{(2)}}e^{ik_z^{(2)}z0} & \frac{k_z^{(2)}}{\mu^{(2)}}e^{-ik_z^{(2)}z0} \end{bmatrix}\begin{bmatrix} E_y^{(2)} \\ E_y'^{(2)} \end{bmatrix}, \tag{A.53}$$

or more concisely,

$$M^{(1)}(z0,\sigma)\begin{bmatrix} E_y^{(1)} \\ E_y'^{(1)} \end{bmatrix} = M^{(1)}(z0,\sigma=0)\begin{bmatrix} E_y^{(2)} \\ E_y'^{(2)} \end{bmatrix}, \tag{A.54}$$

where

$$M^{(j)}(z,\sigma) = \begin{bmatrix} e^{ik_z^{(j)}z} & e^{-ik_z^{(j)}z} \\ \left(-\frac{k_z^{(j)}}{\mu^{(j)}}+\sigma\omega\mu_0\right)e^{ik_z^{(j)}z0} & \left(\frac{k_z^{(j)}}{\mu^{(j)}}+\sigma\omega\mu_0\right)e^{-ik_z^{(j)}z0} \end{bmatrix}. \tag{A.55}$$

For TE Light, it is easiest to define the Fresnel coefficients in terms of the E field, $E_y'^{(1)} = rE_y^{(1)}$ and $E_y^{(2)} = tE_y^{(1)}$. Hence the matrix equation becomes

$$M^{(1)}(z0,\sigma)\begin{bmatrix} 1 \\ r \end{bmatrix} = M^{(2)}(z0,\sigma=0)\begin{bmatrix} t \\ 0 \end{bmatrix}. \tag{A.56}$$

Again, we can solve for r and t explicitly with a matrix inversion step and get

$$r_{TE} = e^{2ik_z^{(1)}z0}\frac{\mu^{(2)}k_z^{(1)}-\mu^{(1)}k_z^{(2)}-\sigma\mu^{(1)}\mu^{(2)}\mu_0\omega}{\mu^{(2)}k_z^{(1)}+\mu^{(1)}k_z^{(2)}+\sigma\mu^{(1)}\mu^{(2)}\mu_0\omega} \tag{A.57}$$

and

$$t_{TE} = e^{i(k_z^{(1)} - k_z^{(2)})z0} \frac{2k_z^{(1)}\mu^{(2)}}{\mu^{(1)}k_z^{(2)} + \mu^{(2)}k_z^{(1)} + \sigma\mu^{(1)}\mu^{(2)}\mu_0\omega}. \tag{A.58}$$

A.3 Multilayered Systems

The matrix formalisms for both TM and TE light allow for straightforward generalization to multilayered structures, particularly because the formalisms results in very similar matrix equations. At a general interface at position z, the field amplitudes for TM light are related by Eq. A.30

$$M^{(1)}(z,\sigma)\begin{bmatrix} E_x^{(1)} \\ E_x'^{(1)} \end{bmatrix} = M^{(2)}(z,\sigma=0)\begin{bmatrix} E_x^{(2)} \\ E_x'^{(2)} \end{bmatrix}, \tag{A.59}$$

where for layer j,

$$M^{j}(z,\sigma) = \begin{bmatrix} e^{ik_z^{(j)}z} & e^{-ik_z^{(j)}z} \\ \left(\frac{\epsilon_{xx}^{(j)}}{k_z^{(j)}} - \frac{\sigma}{\omega\epsilon_0}\right)e^{ik_z^{(j)}z} & -\left(\frac{\epsilon_{xx}^{(j)}}{k_z^{(j)}} + \frac{\sigma}{\omega\epsilon_0}\right)e^{-ik_z^{(j)}z} \end{bmatrix}. \tag{A.60}$$

The Fresnel coefficients for TM light are subsequently defined as $E_x'^{(1)} = -rE_x^{(1)}$ and $E_x^{(2)} = t\frac{\epsilon_{xx}^{(1)}}{\epsilon_{xx}^{(2)}}\frac{k_z^{(2)}}{k_z^{(1)}}E_x^{(1)}$. For TE Light the field amplitudes are related by a similar equation, Eq. A.54,

$$M^{(1)}(z0,\sigma)\begin{bmatrix} E_y^{(1)} \\ E_y'^{(1)} \end{bmatrix} = M^{(1)}(z0,\sigma=0)\begin{bmatrix} E_y^{(2)} \\ E_y'^{(2)} \end{bmatrix}, \tag{A.61}$$

where

$$M^{(j)}(z,\sigma) = \begin{bmatrix} e^{ik_z^{(j)}z} & e^{-ik_z^{(j)}z} \\ \left(-\frac{k_z^{(j)}}{\mu^{(j)}} + \sigma\omega\mu_0\right)e^{ik_z^{(j)}z0} & \left(\frac{k_z^{(j)}}{\mu^{(j)}} + \sigma\omega\mu_0\right)e^{-ik_z^{(j)}z0} \end{bmatrix}, \tag{A.62}$$

and the Fresnel coefficients are defined as $E_y'^{(1)} = rE_y^{(1)}$ and $E_y^{(2)} = tE_y^{(1)}$.

Four Layered Example

Let's take an example with four layers and three interfaces, where the top interface is graphene, and hence has a nonzero surface conductivity.

At the first interface at $z = z0$ for TM(TE) light, we have

$$M^{(1)}(z0,\sigma)\begin{bmatrix} E_{x(y)}^{(1)} \\ E_{x(y)}'^{(1)} \end{bmatrix} = M^{(2)}(z0,0)\begin{bmatrix} E_{x(y)}^{(2)} \\ E_{x(y)}'^{(2)} \end{bmatrix}. \tag{A.63}$$

At the second interface at position $z = z1$, we have

$$M^{(2)}(z1, 0)\begin{bmatrix} E^{(2)}_{x(y)} \\ E'^{(2)}_{x(y)} \end{bmatrix} = M^{(3)}(z1, 0)\begin{bmatrix} E^{(3)}_{x(y)} \\ E'^{(3)}_{x(y)} \end{bmatrix}, \tag{A.64}$$

and at the final interface, we have

$$M^{(3)}(z2, 0)\begin{bmatrix} E^{(3)}_{x(y)} \\ E'^{(3)}_{x(y)} \end{bmatrix} = M^{(4)}(z2, 0)\begin{bmatrix} E^{(4)}_{x(y)} \\ E'^{(4)}_{x(y)} \end{bmatrix}. \tag{A.65}$$

To calculate the Fresnel coefficients, like before we relate the field amplitudes in the substrate (medium 4), to the incident field amplitudes (in medium 1):
For TM light:

$$\begin{bmatrix} 1 \\ -r \end{bmatrix} = M \begin{bmatrix} t\frac{\epsilon^{(1)}_{xx}}{\epsilon^{(4}_{xx}}\frac{k^{(4}_z}{k^{(1)}_z} \\ 0 \end{bmatrix}. \tag{A.66}$$

For TE light:

$$\begin{bmatrix} 1 \\ r \end{bmatrix} = M \begin{bmatrix} t \\ 0 \end{bmatrix}, \tag{A.67}$$

where

$$\begin{aligned} M = M^{(1)}(z0, \sigma)^{-1} M^{(2)}(z0, 0)\, M^{(2)}(z1, 0)^{-1} \\ M^{(3)}(z1, 0)\, M^{(3)}(z2, 0)^{-1}\, M^{(4)}(z2, 0)\,. \end{aligned} \tag{A.68}$$

As a final result, the Fresnel coefficients in terms of matrix elements $M[i, j]$ for TM and TE light, respectively, are as follows:
For TM light:

$$r = -\frac{M[2, 1]}{M[1, 1]} \tag{A.69}$$

$$t = \frac{\epsilon^{(4)}_{xx}}{\epsilon^{(1}_{xx}}\frac{k^{(1}_z}{k^{(4)}_z}\frac{1}{M[1, 1]}. \tag{A.70}$$

For TE light:

$$r = \frac{M[2, 1]}{M[1, 1]} \tag{A.71}$$

$$t = \frac{1}{M[1, 1]}. \tag{A.72}$$

A.4 Harmonic Equations for General Uniaxial Anisotropic Media

To define the wave vector k_z in terms of the in plane wave vector k_x, we must look at the harmonic equations that can be derived from Maxwell's equations. This derivation closely follows that in Fleck et al. [144] Taking the curl of the first term in Eq. A.3, we get

$$\nabla \times (\nabla \times \boldsymbol{E}) = -\frac{\partial}{\partial t}(\nabla \times \boldsymbol{B}) = -\frac{\partial}{\partial t}\frac{\mu \overleftrightarrow{\epsilon}}{c^2}\frac{\partial \boldsymbol{E}}{\partial t} \tag{A.73}$$

$$\nabla(\nabla \cdot \boldsymbol{E}) - \nabla^2 \boldsymbol{E} = -\frac{\mu \overleftrightarrow{\epsilon}}{c^2}\frac{\partial^2 \boldsymbol{E}}{\partial t^2}. \tag{A.74}$$

For isotropic media the permittivity tensor reduces to a scalar, and hence

$$\nabla \cdot \boldsymbol{D} = \epsilon_0 \nabla \cdot \epsilon \boldsymbol{E} = \epsilon_0 \epsilon \nabla \cdot \boldsymbol{E} = 0. \tag{A.75}$$

As a result Eq. A.74 reduces to the standard wave equation,

$$\nabla^2 \boldsymbol{E} - \frac{\mu \overleftrightarrow{\epsilon}}{c^2}\frac{\partial^2 \boldsymbol{E}}{\partial t^2} = 0. \tag{A.76}$$

However, the relation in Eq. A.75 is not valid for the more general uniaxial anisotropic case in which

$$\nabla \cdot \overleftrightarrow{\epsilon} \boldsymbol{E} = \nabla \cdot \left(\epsilon_{xx}\mathcal{E}_x \hat{\boldsymbol{x}} + \epsilon_{xx}\mathcal{E}_y \hat{\boldsymbol{y}} + \epsilon_{zz}\mathcal{E}_z \hat{\boldsymbol{z}}\right) = 0. \tag{A.77}$$

Expanding, we get

$$\epsilon_{xx}\left(\frac{\partial \mathcal{E}_x}{\partial x} + \frac{\partial \mathcal{E}_y}{\partial y} + \frac{\partial \mathcal{E}_z}{\partial z}\right) + (\epsilon_{zz} - \epsilon_{xx})\frac{\partial \mathcal{E}_z}{\partial z} = 0. \tag{A.78}$$

$$\nabla \cdot \boldsymbol{E} = \left(1 - \frac{\epsilon_{zz}}{\epsilon_{xx}}\right)\frac{\partial \mathcal{E}_z}{\partial z}. \tag{A.79}$$

Eq. A.74 becomes

$$\nabla^2 \boldsymbol{E} - \frac{\mu \overleftrightarrow{\epsilon}}{c^2}\frac{\partial^2 \boldsymbol{E}}{\partial t^2} - \nabla\left(\left(1 - \frac{\epsilon_{zz}}{\epsilon_{xx}}\right)\frac{\partial \mathcal{E}_z}{\partial z}\right) = 0. \tag{A.80}$$

As before, let's assume harmonic solutions to the electric field,

$$\boldsymbol{E}(\boldsymbol{r}, t) = \left(E_x \hat{\boldsymbol{x}} + E_y \hat{\boldsymbol{y}} + E_z \hat{\boldsymbol{z}}\right)\, e^{i\boldsymbol{k}\cdot\boldsymbol{r} - i\omega t}. \tag{A.81}$$

Substituting the above expression of the electric field into Eq.A.74, we get

$$\begin{aligned}
&\left(\frac{\partial^2}{\partial^2 x} + \frac{\partial^2}{\partial^2 y} + \frac{\partial^2}{\partial^2 z}\right)\left(E_x \hat{\boldsymbol{x}} + E_y \hat{\boldsymbol{y}} + E_z \hat{\boldsymbol{z}}\right)\, e^{i\boldsymbol{k}\cdot\boldsymbol{r} - i\omega t} \\
&- \frac{\mu \overleftrightarrow{\epsilon}}{c^2}\frac{\partial^2}{\partial t^2}\left(E_x \hat{\boldsymbol{x}} + E_y \hat{\boldsymbol{y}} + E_z \hat{\boldsymbol{z}}\right)\, e^{i\boldsymbol{k}\cdot\boldsymbol{r} - i\omega t} \\
&- \left(\hat{\boldsymbol{x}}\frac{\partial}{\partial x} + \hat{\boldsymbol{y}}\frac{\partial}{\partial y} + \hat{\boldsymbol{z}}\frac{\partial}{\partial z}\right)\left(\left(1 - \frac{\epsilon_{zz}}{\epsilon_{xx}}\right)\frac{\partial}{\partial z} E_z\, e^{i\boldsymbol{k}\cdot\boldsymbol{r} - i\omega t}\right) = 0.
\end{aligned} \tag{A.82}$$

Separated into vector components,

$$\hat{\boldsymbol{x}} : -\left(k_x^2 + k_y^2 + k_z^2\right) E_x + \frac{\mu\epsilon_{xx}\omega^2}{c^2} E_x + \left(1 - \frac{\epsilon_{zz}}{\epsilon_{xx}}\right) k_x k_z E_z = 0 \tag{A.83a}$$

$$\hat{\boldsymbol{y}} : -\left(k_x^2 + k_y^2 + k_z^2\right) E_y + \frac{\mu\epsilon_{xx}\omega^2}{c^2} E_y + \left(1 - \frac{\epsilon_{zz}}{\epsilon_{xx}}\right) k_y k_z E_z = 0 \tag{A.83b}$$

$$\hat{\boldsymbol{z}} : -\left(k_x^2 + k_y^2 + k_z^2\right) E_z + \frac{\mu\epsilon_{zz}\omega^2}{c^2} E_z + \left(1 - \frac{\epsilon_{zz}}{\epsilon_{xx}}\right) k_z^2 E_z = 0. \tag{A.83c}$$

In matrix form:

$$M \begin{pmatrix} E_x \\ E_y \\ E_z \end{pmatrix} = 0, \tag{A.84}$$

where $M =$

$$\begin{pmatrix} \left(k_x^2 + k_y^2 + k_z^2 - \frac{\mu\epsilon_{xx}\omega^2}{c^2}\right) & 0 & -\left(1 - \frac{\epsilon_{zz}}{\epsilon_{xx}}\right) k_x k_z \\ 0 & \left(k_x^2 + k_y^2 + k_z^2 - \frac{\mu\epsilon_{xx}\omega^2}{c^2}\right) & -\left(1 - \frac{\epsilon_{zz}}{\epsilon_{xx}}\right) k_y k_z \\ 0 & 0 & \left(k_x^2 + k_y^2 + \frac{\epsilon_{zz}}{\epsilon_{xx}} k_z^2 - \frac{\mu\epsilon_{zz}\omega^2}{c^2}\right) \end{pmatrix}. \tag{A.85}$$

The determinant of the matrix must equal zero for the fields to be nonzero. As the matrix is upper triangular, the determinant is simply the product of the diagonal components. There are clearly two conditions where the determinant is zero:

$$\left(k_x^2 + k_y^2\right) + k_z^2 = \mu\epsilon_{xx}\left(\frac{\omega}{c}\right)^2 \tag{A.86a}$$

$$\left(k_x^2 + k_y^2\right) + \frac{\epsilon_{zz}}{\epsilon_{xx}} k_z^2 = \mu\epsilon_{zz}\left(\frac{\omega}{c}\right)^2. \tag{A.86b}$$

In the first case given in Eq. A.86a, E_z equals zero, corresponding to TE polarized light. In the second case given in Eq. A.86b, E_z is nonzero and corresponds to TM polarized light. Often times it is beneficial to define an "in-plane" wave vector $k_{||}$, such that $k_{||}^2 = k_x^2 + k_y^2$. We end up at the final relations for the wave vector k_z:

TE Polarized Light:

$$k_z = \sqrt{\mu\epsilon_{xx}\left(\frac{\omega}{c}\right)^2 - k_{||}^2} \tag{A.87}$$

TM Polarized Light:

$$k_z = \sqrt{\mu\epsilon_{xx}\left(\frac{\omega}{c}\right)^2 - \frac{\epsilon_{xx}}{\epsilon_{zz}} k_{||}^2} \tag{A.88}$$

Appendix B

DERIVATION OF ANALYTIC EXPRESSION FOR NEAR FIELD HEAT TRANSFER FOR PLANAR MEDIA

[1] Accelerating charges emit electromagnetic waves. In materials at non-zero temperature, charges jitter back and forth within a material due to their thermal energy, emitting thermal radiation. How much charges jitter at a given temperature relates to the material's intrinsic conductivity (or permittivity). This relationship is quantified in the fluctuation-dissipation theorem that relates the auto-correlation in local current density $\boldsymbol{j}((r,\omega)$ to the permittivity and temperature distribution

$$\langle j_\alpha(\boldsymbol{r},\omega) j_\beta(\boldsymbol{r'},\omega)\rangle = \epsilon_0\omega\frac{\Im(\epsilon)}{\pi}\Theta(\omega,T)\delta(\boldsymbol{r}-\boldsymbol{r'})\delta_{\alpha\beta}, \tag{B.1}$$

where $\Theta(\omega,T) = \hbar\omega/[exp(\hbar\omega/k_bT)-1)]$ is the mean energy of a harmonic oscillator and ϵ is the material permittivity. To solve for the local currents, we use the Green function formalism for the electric and magnetic fields (assuming non magnetic materials)

$$\boldsymbol{E}(\boldsymbol{r},\omega) = \int_V d^3r' i\omega\mu_0\overleftrightarrow{\boldsymbol{G}}_E(\boldsymbol{r},\boldsymbol{r'},\omega)\boldsymbol{j}(\boldsymbol{r'},\omega) \tag{B.2}$$

$$\boldsymbol{H}(\boldsymbol{r},\omega) = \int_V d^3r' \overleftrightarrow{\boldsymbol{G}}_H(\boldsymbol{r},\boldsymbol{r'},\omega)\boldsymbol{j}(\boldsymbol{r'},\omega). \tag{B.3}$$

In our case, we are interested in the heat transferred from one half-space, labeled by subscript 1, into another half-space, labeled with subscript 2, separated from the first by a vacuum gap of thickness d. The vacuum gap is labeled with subscript 3, as shown in the diagram in Figure B.1.

We must solve for the fields in medium 2, caused by a source charge in medium 1. For a source charge at $\boldsymbol{r'} = (\boldsymbol{R'}, -z')$, the Green functions for the fields at $\boldsymbol{r} = (\boldsymbol{r}, z > d)$ are [113]

$$\overleftrightarrow{\boldsymbol{G}}_E(\boldsymbol{r},\boldsymbol{r'},\omega) = \frac{i}{4\pi^2}\int_0^\infty d^2k_{||}\frac{1}{k_{z1}}(\hat{s}t_{21}^s\hat{s}+\hat{p}_2^+t_{21}^p\hat{p}_1^+)e^{i\boldsymbol{k}_{||}\cdot(\boldsymbol{R}-\boldsymbol{R'})}e^{ik_{z2}(z-d)}e^{-ik_{z1}z'} \tag{B.4}$$

[1] The derivation in this section follows closely that laid out in Joulain et al. [113] with some of the steps filled in. Other helpful resources are [145–147].

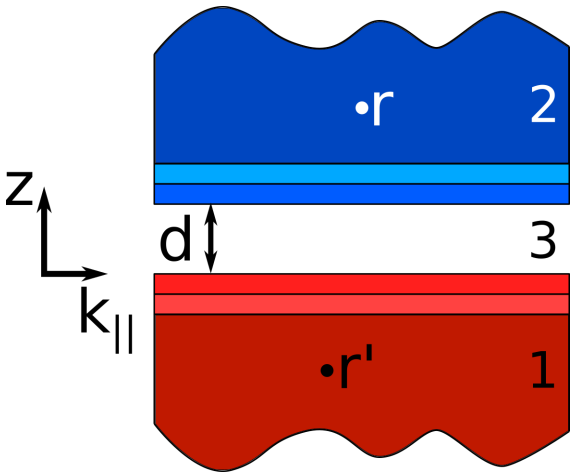

Figure B.1: Diagram of two layered half-spaces

$$\overleftrightarrow{\boldsymbol{G}}_H(\boldsymbol{r},\boldsymbol{r'},\omega) = -\frac{n_2\omega}{4\pi^2 c}\int_0^\infty d^2k_{||}\frac{1}{k_{z1}}(-\hat{p}_2^+ t_{21}^s \hat{s}\,\hat{s} + \hat{s}t_{21}^p \hat{p}_1^+)e^{i\boldsymbol{k}_{||}\cdot(\boldsymbol{R}-\boldsymbol{R'})}e^{ik_{z2}(z-d)}e^{-ik_{z1}z'}. \tag{B.5}$$

The wave vector components are $\boldsymbol{k} = (\boldsymbol{k}_{||}, k_z\hat{z})$, where $\boldsymbol{k}_{||}$ is the in-plane wave vector and k_z is the z-component, such that $k = \sqrt{\epsilon(\frac{\omega}{c})^2 - k_{||}^2}$. The unit vectors in Eqs.B.2 and B.3 are $\hat{s} = \hat{k}_{||} \times \hat{z}$ and $\hat{p}_i^\pm = (k_{||}\hat{z} \mp k_{zi}\hat{k}_{||})/(n_i\omega/c)$, and the term $t_{21}^{s,p}$ is the generalized Fresnel coefficient from medium 2 into medium 1, where for a given polarization s or p [146]

$$t_{12} = \frac{t_{13}t_{23}e^{ik_{z3}d}}{1 - r_{31}r_{32}e^{2ik_{z3}d}}. \tag{B.6}$$

Ultimately, we are interested in the energy density that these fields convey from one medium to the other, or rather the mean z-component of the Poynting vector

$$\langle S_z\rangle = \frac{1}{2}\Re\langle \boldsymbol{E}\times\boldsymbol{H}^*\cdot\hat{z}\rangle = \frac{1}{2}\Re\langle E_x H_y^* - E_y H_x^*\rangle. \tag{B.7}$$

Making use of Einstein's summation convention, we find that the vector components of the above fields are in the following form:

$$A_i(\boldsymbol{r},\omega) = C\int d^3r'\int d^2k_{||}e^{i\boldsymbol{k}_{||}\cdot(\boldsymbol{R}-\boldsymbol{R'})}e^{ik_{z2}(z-d)}e^{-ik_{z1}z'}G_{ij}j_j(\boldsymbol{r'})\forall i,j\in\{x,y,z\}. \tag{B.8}$$

Hence, the terms in Eq. B.7 evaluate to

$$\begin{aligned}\langle E_x H_y^*\rangle =& \frac{n_2^*\mu_0\omega^2}{16\pi^4 c}\int d^3r'\int d^3r''\int d^2k_{||}\int d^2k'_{||}\frac{1}{|k_{z1}|^2}\\ & e^{i\boldsymbol{k}_{||}\cdot(\boldsymbol{R}-\boldsymbol{R'})}e^{ik_{z2}(z-d)}e^{-ik_{z1}z'}e^{-i\boldsymbol{k}'_{||}\cdot(\boldsymbol{R}-\boldsymbol{R''})}e^{-ik'^*_{z2}(z-d)}e^{ik'^*_{z1}z''}\\ & (\hat{s}t_{21}^s\hat{s} + \hat{p}_2^+t_{21}^p\hat{p}_1^+)_{xk}(-\hat{p}_2^+t_{21}^s\hat{s} + \hat{s}t_{21}^p\hat{p}_1^+)^*_{yl}\langle j_k(\boldsymbol{r'},\omega)j_l^*(\boldsymbol{r''},\omega)\rangle.\end{aligned} \tag{B.9}$$

Plugging in the fluctuation-dissipation theorem in Eq. B.1, we get

$$\begin{aligned}\langle E_x H_y^* \rangle =& \frac{n_2^* \mu_0 \omega^2}{16\pi^4 c} \int d^3r' \int d^3r'' \int d^2k_{||} \int d^2k'_{||} \frac{1}{|k_{z1}|^2} \\ & e^{i\boldsymbol{k}_{||}\cdot(\boldsymbol{R}-\boldsymbol{R'})} e^{ik_{z2}(z-d)} e^{-ik_{z1}z'} e^{-i\boldsymbol{k}'_{||}\cdot(\boldsymbol{R}-\boldsymbol{R''})} e^{-ik'^*_{z2}(z-d)} e^{ik'^*_{z1}z''} \\ & (\hat{s}t^s_{21}\hat{s} + \hat{p}^+_2 t^p_{21}\hat{p}^+_1)_{xk}(-\hat{p}^+_2 t^s_{21}\hat{s} + \hat{s}t^p_{21}\hat{p}^+_1)^*_{yl} \epsilon_0 \omega \frac{\Im(\epsilon_1)}{\pi} \Theta(\omega, T)\delta(\boldsymbol{r'} - \boldsymbol{r''})\delta_{kl}.\end{aligned} \tag{B.10}$$

After applying the Kroenecker delta, and integrating over d^3r'', we get

$$\begin{aligned}\langle E_x H_y^* \rangle =& \frac{n_2^* \mu_0 \epsilon_0 \omega^3 \Theta(\omega, T)}{16\pi^5 c} \int d^3r' \int d^2k_{||} \int d^2k'_{||} \frac{1}{|k_{z1}|^2} \Im(\epsilon_1) \\ & e^{i\boldsymbol{k}_{||}\cdot(\boldsymbol{R}-\boldsymbol{R'})} e^{ik_{z2}(z-d)} e^{-ik_{z1}z'} e^{-i\boldsymbol{k}'_{||}\cdot(\boldsymbol{R}-\boldsymbol{R'})} e^{-ik'^*_{z2}(z-d)} e^{ik'^*_{z1}z'} \\ & (\hat{s}t^s_{21}\hat{s} + \hat{p}^+_2 t^p_{21}\hat{p}^+_1)_{xk}(-\hat{p}^+_2 t^s_{21}\hat{s} + \hat{s}t^p_{21}\hat{p}^+_1)^*_{yk}.\end{aligned} \tag{B.11}$$

By the definition of r', the differential $d^3r' = d^2R'dz'$. Including this fact and further consolidating terms, we get

$$\begin{aligned}\langle E_x H_y^* \rangle =& \frac{n_2^* \omega^3 \Theta(\omega, T)}{16\pi^5 c^3} \int d^2k_{||} \int d^2k'_{||} \frac{1}{|k_{z1}|^2} \Im(\epsilon_1) e^{i\boldsymbol{R}\cdot(\boldsymbol{k}_{||}-\boldsymbol{k}'_{||})} e^{i(k_{z2}-k'^*_{z2})(z-d)} \\ & (\hat{s}t^s_{21}\hat{s} + \hat{p}^+_2 t^p_{21}\hat{p}^+_1)_{xk}(-\hat{p}^+_2 t^s_{21}\hat{s} + \hat{s}t^p_{21}\hat{p}^+_1)^*_{yk} \\ & \int_{-\infty}^{0} dz' e^{(ik'^*_{z1} - ik_{z1})z'} \int d^2R' e^{-i\boldsymbol{R'}\cdot(\boldsymbol{k}_{||}-\boldsymbol{k}'_{||})}.\end{aligned} \tag{B.12}$$

The last integral equals $4\pi^2\delta(\boldsymbol{k}_{||} - \boldsymbol{k}'_{||})$. As k_z is a function of $k_{||}$, evaluating the integral over $d^2k'_{||}$ reduces $k'_z \to k_z$, and we get

$$\begin{aligned}\langle E_x H_y^* \rangle =& \frac{n_2^* \omega^3 \Theta(\omega, T)}{4\pi^3 c^3} \int d^2k_{||} \frac{1}{|k_{z1}|^2} \Im(\epsilon_1) e^{-2\Im(k_{z2})(z-d)} \\ & (\hat{s}t^s_{21}\hat{s} + \hat{p}^+_2 t^p_{21}\hat{p}^+_1)_{xk}(-\hat{p}^+_2 t^s_{21}\hat{s} + \hat{s}t^p_{21}\hat{p}^+_1)^*_{yk} \\ & \int_{-\infty}^{0} dz' e^{2\Im(k_{z1})z'}.\end{aligned} \tag{B.13}$$

The last integral simplifies to $\frac{1}{2\Im(k_{z1})}$ such that

$$\begin{aligned}\langle E_x H_y^* \rangle =& \frac{n_2^* \omega^3 \Theta(\omega, T)}{4\pi^3 c^3} \int d^2k_{||} \frac{1}{|k_{z1}|^2} \frac{\Im(\epsilon_1)}{2\Im(k_{z1})} e^{-2\Im(k_{z2})(z-d)} \\ & (\hat{s}t^s_{21}\hat{s} + \hat{p}^+_2 t^p_{21}\hat{p}^+_1)_{xk}(-\hat{p}^+_2 t^s_{21}\hat{s} + \hat{s}t^p_{21}\hat{p}^+_1)^*_{yk}.\end{aligned} \tag{B.14}$$

By symmetry of the indices the other half of the Poynting vector is

$$\begin{aligned}\langle E_y H_x^* \rangle =& \frac{n_2^* \omega^3 \Theta(\omega, T)}{4\pi^3 c^3} \int d^2 k_{||} \frac{1}{|k_{z1}|^2} \frac{\Im(\epsilon_1)}{2\Im(k_{z1})} e^{-2\Im(k_{z2})(z-d)} \\ & (\hat{s} t_{21}^s \hat{s} + \hat{p}_2^+ t_{21}^p \hat{p}_1^+)_{yk} (-\hat{p}_2^+ t_{21}^s \hat{s} + \hat{s} t_{21}^p \hat{p}_1^+)_{xk}^*.\end{aligned} \tag{B.15}$$

All that remains is to sum over the Cartesian components k. Here, it is beneficial to assume without loss of generality that the in-plane wave vector is parallel to the x-axis, such that $\hat{k}_{||} = \hat{x}$. By the definitions of $\hat{s} = \hat{k}_{||} \times \hat{z}$ and $\hat{p_i^{\pm}} = (k_{||}\hat{z} \mp k_{zi}\hat{k}_{||})/(n_i \omega/c)$, we get the following dot product relations:

$$\begin{aligned}&\hat{s} \cdot \hat{x} = \hat{s} \cdot \hat{z} = 0, \ \hat{s} \cdot \hat{y} = -1 \\ &\hat{p_i^{\pm}} \cdot \hat{x} = \frac{\mp k_{zi}}{n_i \omega/c}, \ \hat{p_i^{\pm}} \cdot \hat{y} = 0, \ \hat{p_i^{\pm}} \cdot \hat{z} = \frac{k_{||}}{n_i \omega/c}.\end{aligned} \tag{B.16}$$

It is also beneficial to adopt a more concise notation, where

$$\begin{aligned}g_{\alpha\beta}^E &= (\hat{s} t_{21}^s \hat{s} + \hat{p}_2^+ t_{21}^p \hat{p}_1^+)_{\alpha\beta} \\ g_{\alpha\beta}^{H*} &= (-\hat{p}_2^+ t_{21}^s \hat{s} + \hat{s} t_{21}^p \hat{p}_1^+)_{\alpha\beta}^*.\end{aligned} \tag{B.17}$$

For $k = x$:

$$\begin{aligned}g_{xx}^E g_{yx}^{H*} &= \left(0 + \frac{-k_{z2}}{n_2 \omega/c} t_{21}^p \frac{-k_{z1}}{n_1 \omega/c}\right) \left(0 - 1 t_{21}^{p*} \frac{-k_{z1}^*}{n_1^* \omega/c}\right) \\ &= \frac{k_{z2} |k_{z1}|^2 |t_{21}^p|^2}{n_2 |n_1|^2 \omega^3/c^3}.\end{aligned} \tag{B.18}$$

For $k = y$:

$$g_{xy}^E g_{yy}^{H*} = 0. \tag{B.19}$$

For $k = z$:

$$\begin{aligned}g_{xz}^E g_{yz}^{H*} &= \left(0 + \frac{-k_{z2}}{n_2 \omega/c} t_{21}^p \frac{k_{||}}{n_1 \omega/c}\right) \left(0 - 1 t_{21}^{p*} \frac{k_{||}}{n_1^* \omega/c}\right) \\ &= \frac{k_{z2} k_{||}^2 |t_{21}^p|^2}{n_2 |n_1|^2 \omega^3/c^3}.\end{aligned} \tag{B.20}$$

Summing these three components together results in

$$g_{xk}^E g_{yk}^{H*} = \frac{k_{z2} |t_{21}^p|^2}{n_2 |n_1|^2 \omega/c} \left(\frac{k_{||}^2 + |k_{z1}|^2}{\omega^2/c^2}\right). \tag{B.21}$$

To evaluate the expression for $\langle E_y H_x^* \rangle$, we must do the same calculation for $g_{yk}^E g_{xk}^{H*}$. For $k = x$ and $k = z$, this expression is 0. For k = y, we get

$$\begin{aligned}g_{yy}^E g_{xy}^{H*} &= \left(t_{21}^s + 0\right) \left(\frac{k_{z2}^*}{n_2^* \omega/c} t_{21}^{s*} (-1) + 0\right) \\ &= -\frac{k_{z2}^* |t_{21}^s|^2}{n_2^* \omega/c}.\end{aligned} \tag{B.22}$$

Hence the z-component of the Poynting vector, evaluated at the interface of the second half-space $z = d$, is

$$\langle S_{z1\to 2}\rangle = \Re\left(\frac{1}{2}\langle E_x H_y^* - E_y H_x^*\rangle\right) = \Re\left[\frac{n_2^*\omega^3\Theta(\omega,T_1)}{8\pi^3 c^3}\int d^2k_{||}\frac{1}{|k_{z1}|^2}\frac{\Im(\epsilon_1)}{2\Im(k_{z1})}\right.$$
$$\left.\left(\frac{k_{z2}|t_{21}^p|^2}{n_2|n_1|^2\omega/c}\left(\frac{k_{||}^2+|k_{z1}|^2}{\omega^2/c^2}\right)+\frac{k_{z2}^*|t_{21}^s|^2}{n_2^*\omega/c}\right)\right]. \tag{B.23}$$

To simplify this expression, we use a number of useful identities: [113, 147]

$$\begin{aligned}
\Im(\epsilon_i)\frac{\omega^2}{c^2} &= 2\Re(k_{zi})\Im(k_{zi}) \\
\Re(\epsilon_i^* k_{zi}) &= \Re(k_{zi})\frac{|k_{zi}|^2+k_{||}^2}{\omega^2/c^2} \\
\Im(\epsilon_i^* k_{zi}) &= \Im(k_{zi})\frac{-|k_{zi}|^2+k_{||}^2}{\omega^2/c^2}
\end{aligned} \tag{B.24}$$

and we get

$$\langle S_{z1\to 2}\rangle = \frac{\Theta(\omega,T_1)}{8\pi^3}\int d^2k_{||}\frac{1}{|k_{z1}|^2}\left(|t_{21}^s|^2\Re(k_{z1})\Re(k_{z2})\right.$$
$$\left.+\frac{|t_{21}^p|^2\Re(\epsilon_1^* k_{z1})\Re(\epsilon_2^* k_{z2})}{|n_1|^2 n_2|^2}\right). \tag{B.25}$$

After plugging in the expression for the generalized Fresnel coefficients from Eq. B.6

$$\langle S_{z1\to 2}\rangle = \frac{\Theta(\omega,T_1)}{8\pi^3}\int d^2k_{||}\frac{1}{|k_{z1}|^2}\left(\frac{|t_{13}^s|^2|t_{23}^s|^2\Re(k_{z1})\Re(k_{z2})}{|1-r_{13}^s r_{13}^s e^{2ik_{z0}d}|^2}\right.$$
$$\left.+\frac{|t_{13}^p|^2|t_{23}^p|^2\Re(\epsilon_1^* k_{z1})\Re(\epsilon_2^* k_{z2})}{|n_1|^2 n_2|^2|1-r_{13}^s r_{13}^s e^{2ik_{z0}d}|^2}\right). \tag{B.26}$$

For non-magnetic materials, the following identities hold:

$$\begin{aligned}
\Re(k_{z3})(1-|r_{13}|^2) &= \Re(k_{z1})|t_{13}|^2 \\
\Re(k_{z3})(1-|r_{23}|^2) &= \Re(k_{z2})|t_{23}|^2\frac{|k_{z3}|^2}{|k_{z2}|^2} \\
\Re(\epsilon_3^* k_{z3})(1-|r_{31}^p|^2)+2\Im(\epsilon_3^* k_{z3})\Im(r_{13}^p) &= \Re(\epsilon_1^* k_{z1})|t_{31}^p|^2\frac{|n_3|^2}{|n_1|^2} \\
\Re(\epsilon_3^* k_{z3})(1-|r_{31}^p|^2)+2\Im(\epsilon_3^* k_{z3})\Im(r_{23}^p) &= \Re(\epsilon_2^* k_{z2})|t_{32}^p|^2\frac{|n_3|^2}{|n_1|^2}\frac{|\epsilon_3|^2}{|\epsilon_2|^2}\frac{|k_{z3}|^2}{|k_{z2}|^2},
\end{aligned}$$

where r_{13}, r_{23}, t_{13}, and t_{23} are the Fresnel reflection and transmission coefficients of half-space 1 into vacuum and half-space 2 into vacuum, respectively. In medium 3, inside the vacuum gap, $n_3 = \epsilon_3 = 1$. Moreover, for propagating modes where $k_{||} < \omega/c$, the z-component of the wave vector in vacuum is purely real, $\Re(k_{z3}) = k_{z3}$, $\Im(k_{z3}) = 0$. On the other hand, for evanescent modes where $k_{||} > \omega/c$, the opposite is true, $\Re(k_{z3}) = 0$, $\Im(k_{z3}) = |k_{z3}|$. These facts allows us divide the integral in Eq. B.26 into a propagating part and an evanescent part. By applying in the identities in Eq. B.27 and the fact that for uniaxial media $d^2k_{||} = 2\pi k_{||} dk_{||}$ we get

$$\langle S_{z1\to 2}\rangle = \frac{\Theta(\omega, T_1)}{4\pi^2}\sum_{s,p}\int k_{||}dk_{||}\left(\frac{(1-|r_{31}^{s,p}|^2)(1-|r_{32}^{s,p}|^2)}{|1-r_{13}^{s}r_{13}^{s}e^{2ik_{z0}d}|^2} + \frac{4\Im(r_{31}^{s,p})\Im(r_{32}^{s,p})}{|1-r_{13}^{s}r_{13}^{s}e^{2ik_{z0}d}|^2}\right). \tag{B.27}$$

This expression is the power emitted from half-space 1 and absorbed by half-space 2. To get the net heat flux, we must also subtract the power emitted from half-space 2 back into half-space 1. The expression is identical to Eq. B.27, except the indices are reversed:

$$\langle S_{z2\to 1}\rangle = \frac{\Theta(\omega, T_2)}{4\pi^2}\sum_{s,p}\int k_{||}dk_{||}\left(\frac{(1-|r_{31}^{s,p}|^2)(1-|r_{32}^{s,p}|^2)}{|1-r_{13}^{s}r_{13}^{s}e^{2ik_{z0}d}|^2} + \frac{4\Im(r_{31}^{s,p})\Im(r_{32}^{s,p})}{|1-r_{13}^{s}r_{13}^{s}e^{2ik_{z0}d}|^2}\right). \tag{B.28}$$

As the expression inside the integral in Eqs. B.27 and B.28 is symmetric for indices 1 and 2, all that changes is the Bose-factor Θ. We define the spectral heat flux $H(\omega, T_1, T_2)$ as

$$H(\omega, T_1, T_2) = \Phi(\omega)\left(\Theta(\omega, T_1) - \Theta(\omega, T_2)\right), \tag{B.29}$$

where $\Phi(\omega)$ is the transmissivity function, partitioned over propagating modes where $k_{||} < \omega/c$, and evanescent modes where $k_{||} > \omega/c$[89],

$$\Phi(\omega) = \sum_{s,p}\int_0^{\omega/c} dk_{||}\frac{k_{||}}{2\pi}\frac{(1-|r_{13}^{s,p}|^2)(1-|r_{23}^{s,p}|^2)}{|1-r_{13}^{s,p}r_{23}^{s,p}e^{i2k_{z0}d}|^2} + \int_{\omega/c}^{\infty} dk_{||}\frac{k_{||}}{2\pi}\frac{4\Im(r_{13}^{s,p})\Im(r_{23}^{s,p})}{|1-r_{13}^{s,p}r_{23}^{s,p}e^{-2|k_{z0}|d}|^2}. \tag{B.30}$$

This expression is also valid for layered media, where the Fresnel coefficients can be calculated by the transfer matrix method, as outlined in Appendix A [89]. To get

the total heat flux we integrate the Poynting vector over all frequencies such that

$$Q(T_1, T_2) = \int_0^\infty \frac{d\omega}{2\pi} H(\omega, T_1, T_2). \tag{B.31}$$

BIBLIOGRAPHY

[1] Gustav Kirchhoff. Ueber das Verhältniss zwischen dem Emissionsvermögen und dem Absorptionsvermögen der Körper für Wärme and Licht". *Annalen der Physik und Chemie*, 109(2):275–301, 1860.

[2] Wilhelm Wien. Ueber die Energievertheilung im Emissionsspectrum eines schwarzen Körpers. *Annalen der Physik und Chemie*, 58:669, 1896.

[3] Max Planck. Zur Theorie des Gesetzes der Energieverteilung im Normalspectrum. *Verhandlungen der Deutschen physikalischen Gesellschaft*, 2(17):245, 1900.

[4] Sherwood B. Idso and Ray D. Jackson. Thermal radiation from the atmosphere. *Journal of Geophysical Research*, 74(23):5397–5403, 1969.

[5] William Shockley and Hans J. Queisser. Detailed Balance Limit of Efficiency of p-n Junction Solar Cells. *Journal of Applied Physics*, 32(3):510–519, March 1961.

[6] Nils-Peter Harder and Peter Würfel. Theoretical limits of thermophotovoltaic solar energy conversion. *Semiconductor Science and Technology*, 18(5):S151, 2003.

[7] E. Rephaeli and S. H. Fan. Absorber and emitter for solar thermophotovoltaic systems to achieve efficiency exceeding the Shockley-Queisser limit. *Optics Express*, 17(17):15145–15159, August 2009.

[8] A. Lenert, D. M. Bierman, Y. Nam, W. R. Chan, I. Celanovic, M. Soljacic, and E. N. Wang. A nanophotonic solar thermophotovoltaic device. *Nature Nanotechnology*, 9(2):126–130, February 2014.

[9] Zunaid Omair, Zunaid Omair, Gregg Scranton, Gregg Scranton, Luis M. Pazos-Outón, Myles A. Steiner, Per F. Peterson, John Holzrichter, Eli Yablonovitch, and Eli Yablonovitch. Experimental Demonstration of 28.2% Thermophotovoltaic Conversion Efficiency. In *Conference on Lasers and Electro-Optics (2018), paper AW3O.7*, page AW3O.7. Optical Society of America, May 2018.

[10] Xianliang Liu, Talmage Tyler, Tatiana Starr, Anthony F. Starr, Nan Marie Jokerst, and Willie J. Padilla. Taming the Blackbody with Infrared Metamaterials as Selective Thermal Emitters. *Physical Review Letters*, 107(4):045901, July 2011.

[11] Eden Rephaeli, Aaswath Raman, and Shanhui Fan. Ultrabroadband Photonic Structures To Achieve High-Performance Daytime Radiative Cooling. *Nano Letters*, 13(4):1457–1461, April 2013.

[12] L. X. Zhu, A. Raman, and S. H. Fan. Color-preserving daytime radiative cooling. *Applied Physics Letters*, 103(22), November 2013.

[13] Aaswath P. Raman, Marc Abou Anoma, Linxiao Zhu, Eden Rephaeli, and Shanhui Fan. Passive radiative cooling below ambient air temperature under direct sunlight. *Nature*, 515(7528):540–544, 2014.

[14] Jun-long Kou, Zoila Jurado, Zhen Chen, Shanhui Fan, and Austin J. Minnich. Daytime Radiative Cooling Using Near-Black Infrared Emitters. *ACS Photonics*, 4(3):626–630, March 2017.

[15] Yao Zhai, Yaoguang Ma, Sabrina N. David, Dongliang Zhao, Runnan Lou, Gang Tan, Ronggui Yang, and Xiaobo Yin. Scalable-manufactured randomized glass-polymer hybrid metamaterial for daytime radiative cooling. *Science*, page eaai7899, February 2017.

[16] Zhen Chen, Linxiao Zhu, Aaswath Raman, and Shanhui Fan. Radiative cooling to deep sub-freezing temperatures through a 24-h day–night cycle. *Nature Communications*, 7:13729, December 2016.

[17] H Tabor. Selective radiation. i. wavelength discrimination: A new approach to the harnessing of solar energy. *Bull. Res. Council Isr.*, 5A:119, 1956.

[18] F. Cao, K. McEnaney, G. Chen, and Z. F. Ren. A review of cermet-based spectrally selective solar absorbers. *Energy & Environmental Science*, 7(5):1615–1627, May 2014.

[19] Glen E. McDonald. Spectral reflectance properties of black chrome for use as a solar selective coating. *Sol. Energy*, 17(2):119–122, 1975.

[20] Y. Yin, Y. Pan, L. X. Hang, D. R. McKenzie, and M. M. M. Bilek. Direct current reactive sputtering cr–cr2o3 cermet solar selective surfaces for solar hot water applications. *Thin Solid Films*, 517(5):1601–1606, 2009.

[21] Lu Tang, Feng Cao, Yang Li, Jiming Bao, and Zhifeng Ren. High performance mid-temperature selective absorber based on titanium oxides cermet deposited by direct current reactive sputtering of a single titanium target. *J. Appl. Phys.*, 119(4):045102, 2016.

[22] Feng Cao, Daniel Kraemer, Lu Tang, Yang Li, Alexander P. Litvinchuk, Jiming Bao, Gang Chen, and Zhifeng Ren. High-performance spectrally-selective solar absorber based on yttria-stabilized zirconia cermet with high-temperature stability. *Energy Environ. Sci.*, 2015.

[23] Jeffrey B. Chou, Yi Xiang Yeng, Yoonkyung E. Lee, Andrej Lenert, Veronika Rinnerbauer, Ivan Celanovic, Marin Soljačić, Nicholas X. Fang, Evelyn N. Wang, and Sang-Gook Kim. Enabling ideal selective solar absorption with 2d metallic dielectric photonic crystals. *Adv. Mater.*, 26(47):8041–8045, 2014.

[24] E. Rephaeli and S. Fan. Tungsten black absorber for solar light with wide angular operation range. *Appl. Phys. Lett.*, 92(21), 2008.

[25] Pengfei Li, Baoan Liu, Yizhou Ni, Kaiyang Kevin Liew, Jeff Sze, Shuo Chen, and Sheng Shen. Large-scale nanophotonic solar selective absorbers for high-efficiency solar thermal energy conversion. *Adv. Mater.*, pages 4585–4591, 2015.

[26] Harish C. Barshilia, N. Selvakumar, G. Vignesh, K. S. Rajam, and A. Biswas. Optical properties and thermal stability of pulsed-sputter-deposited alxoy/al/alxoy multilayer absorber coatings. *Sol. Energy Mater. Sol. Cells*, 93(3):315–323, 2009.

[27] S. Lang, G. Sharma, S. Molesky, P. U. Kränzien, T. Jalas, Z. Jacob, A. Yu. Petrov, and M. Eich. Dynamic measurement of near-field radiative heat transfer. *Scientific Reports*, 7(1):13916, October 2017.

[28] Bai Song, Dakotah Thompson, Anthony Fiorino, Yashar Ganjeh, Pramod Reddy, and Edgar Meyhofer. Radiative heat conductances between dielectric and metallic parallel plates with nanoscale gaps. *Nature Nanotechnology*, 11(6):509–514, June 2016.

[29] Jesse I. Watjen, Bo Zhao, and Zhuomin M. Zhang. Near-field radiative heat transfer between doped-Si parallel plates separated by a spacing down to 200 nm. *Applied Physics Letters*, 109(20):203112, 2016.

[30] Kyeongtae Kim, Bai Song, Víctor Fernández-Hurtado, Woochul Lee, Wonho Jeong, Longji Cui, Dakotah Thompson, Johannes Feist, M. T. Homer Reid, Francisco J. García-Vidal, Juan Carlos Cuevas, Edgar Meyhofer, and Pramod Reddy. Radiative heat transfer in the extreme near field. *Nature*, 528(7582):387–391, December 2015.

[31] Michael P. Bernardi, Daniel Milovich, and Mathieu Francoeur. Radiative heat transfer exceeding the blackbody limit between macroscale planar surfaces separated by a nanosize vacuum gap. *Nature Communications*, 7:12900, 2016.

[32] Kota Ito, Atsushi Miura, Hideo Iizuka, and Hiroshi Toshiyoshi. Parallel-plate submicron gap formed by micromachined low-density pillars for near-field radiative heat transfer. *Applied Physics Letters*, 106(8):083504, 2015.

[33] Bai Song, Yashar Ganjeh, Seid Sadat, Dakotah Thompson, Anthony Fiorino, Víctor Fernández-Hurtado, Johannes Feist, Francisco J. Garcia-Vidal, Juan Carlos Cuevas, Pramod Reddy, and Edgar Meyhofer. Enhancement of near-field radiative heat transfer using polar dielectric thin films. *Nature Nanotechnology*, 10(3):253–258, March 2015.

[34] Anthony Fiorino, Dakotah Thompson, Linxiao Zhu, Bai Song, Pramod Reddy, and Edgar Meyhofer. Giant Enhancement in Radiative Heat Transfer in Sub-30 nm Gaps of Plane Parallel Surfaces. *Nano Letters*, 18(6):3711–3715, June 2018.

[35] Anthony Fiorino, Linxiao Zhu, Dakotah Thompson, Rohith Mittapally, Pramod Reddy, and Edgar Meyhofer. Nanogap near-field thermophotovoltaics. *Nature Nanotechnology*, 13(9):806, September 2018.

[36] Vazrik Chiloyan, Jivtesh Garg, Keivan Esfarjani, and Gang Chen. Transition from near-field thermal radiation to phonon heat conduction at sub-nanometre gaps. *Nature Communications*, 6:6755, April 2015.

[37] Andrei V. Shchegrov, Karl Joulain, Rémi Carminati, and Jean-Jacques Greffet. Near-Field Spectral Effects due to Electromagnetic Surface Excitations. *Physical Review Letters*, 85(7):1548–1551, August 2000.

[38] Lu Hu, Arvind Narayanaswamy, Xiaoyuan Chen, and Gang Chen. Near-field thermal radiation between two closely spaced glass plates exceeding Planck's blackbody radiation law. *Applied Physics Letters*, 92(13):133106, 2008.

[39] Hamidreza Chalabi, Erez Hasman, and Mark L. Brongersma. Near-field radiative thermal transfer between a nanostructured periodic material and a planar substrate. *Physical Review B*, 91(1):014302, June 2015.

[40] Soumyadipta Basu and Mathieu Francoeur. Near-field radiative heat transfer between metamaterial thin films. *Optics Letters*, 39(5):1266, March 2014.

[41] Yu Guo and Zubin Jacob. Thermal hyperbolic metamaterials. *Optics Express*, 21(12):15014–15019, June 2013.

[42] S.-A. Biehs, M. Tschikin, and P. Ben-Abdallah. Hyperbolic Metamaterials as an Analog of a Blackbody in the Near Field. *Physical Review Letters*, 109(10):104301, September 2012.

[43] Zhaowei Liu, Hyesog Lee, Yi Xiong, Cheng Sun, and Xiang Zhang. Far-Field Optical Hyperlens Magnifying Sub-Diffraction-Limited Objects. *Science*, 315(5819):1686–1686, March 2007.

[44] Ding Ding and Austin J. Minnich. Selective radiative heating of nanostructures using hyperbolic metamaterials. *Optics Express*, 23(7):A299–A308, April 2015.

[45] D. Ding, T. Kim, and A. J. Minnich. Active thermal extraction of near-field thermal radiation. *Physical Review B*, 93(8):081402, February 2016.

[46] D. Ding, T. Kim, and A. J. Minnich. Active Thermal Extraction and Temperature Sensing of Near-field Thermal Radiation. *Scientific Reports*, 6:32744, September 2016.

[47] X. L. Liu, R. Z. Zhang, and Z. M. Zhang. Near-field radiative heat transfer with doped-silicon nanostructured metamaterials. *International Journal of Heat and Mass Transfer*, 73:389–398, June 2014.

[48] Soumyadipta Basu and Liping Wang. Near-field radiative heat transfer between doped silicon nanowire arrays. *Applied Physics Letters*, 102(5):053101, February 2013.

[49] Sheng Shen, Anastassios Mavrokefalos, Poetro Sambegoro, and Gang Chen. Nanoscale thermal radiation between two gold surfaces. *Applied Physics Letters*, 100(23):233114, June 2012.

[50] A. H. Castro Neto, F. Guinea, N. M. R. Peres, K. S. Novoselov, and A. K. Geim. The electronic properties of graphene. *Reviews of Modern Physics*, 81(1):109–162, January 2009.

[51] S. Das Sarma, Shaffique Adam, E. H. Hwang, and Enrico Rossi. Electronic transport in two dimensional graphene. *Reviews of Modern Physics*, 83(2):407–470, May 2011. arXiv: 1003.4731.

[52] Long Ju, Baisong Geng, Jason Horng, Caglar Girit, Michael Martin, Zhao Hao, Hans A. Bechtel, Xiaogan Liang, Alex Zettl, Y. Ron Shen, and Feng Wang. Graphene plasmonics for tunable terahertz metamaterials. *Nature Nanotechnology*, 6(10):630–634, October 2011.

[53] Victor W. Brar, Min Seok Jang, Michelle Sherrott, Josue J. Lopez, and Harry A. Atwater. Highly Confined Tunable Mid-Infrared Plasmonics in Graphene Nanoresonators. *Nano Letters*, 13(6):2541–2547, June 2013.

[54] Victor W. Brar, Min Seok Jang, Michelle Sherrott, Seyoon Kim, Josue J. Lopez, Laura B. Kim, Mansoo Choi, and Harry Atwater. Hybrid Surface-Phonon-Plasmon Polariton Modes in Graphene/Monolayer h-BN Heterostructures. *Nano Letters*, 14(7):3876–3880, July 2014.

[55] G. A. Domoto, R. F. Boehm, and C. L. Tien. Experimental Investigation of Radiative Transfer Between Metallic Surfaces at Cryogenic Temperatures. *Journal of Heat Transfer*, 92(3):412–416, August 1970.

[56] C. M. Hargreaves. Philips Research Reports. *Supplement*, 5(1), 1973.

[57] Arvind Narayanaswamy, Sheng Shen, and Gang Chen. Near-field radiative heat transfer between a sphere and a substrate. *Physical Review B*, 78(11):115303, September 2008.

[58] Sheng Shen, Arvind Narayanaswamy, and Gang Chen. Surface Phonon Polaritons Mediated Energy Transfer between Nanoscale Gaps. *Nano Letters*, 9(8):2909–2913, August 2009.

[59] Jiang Yang, Wei Du, Yishu Su, Yang Fu, Shaoxiang Gong, Sailing He, and Yungui Ma. Observing of the super-Planckian near-field thermal radiation between graphene sheets. *Nature Communications*, 9(1):4033, October 2018.

[60] P. Ben-Abdallah, A. Belarouci, L. Frechette, and S.-A. Biehs. Heat flux splitter for near-field thermal radiation. *Applied Physics Letters*, 107(5):053109, August 2015.

[61] Clayton R. Otey, Wah Tung Lau, and Shanhui Fan. Thermal Rectification through Vacuum. *Physical Review Letters*, 104(15):154301, April 2010.

[62] Philippe Ben-Abdallah and Svend-Age Biehs. Near-Field Thermal Transistor. *Physical Review Letters*, 112(4):044301, January 2014.

[63] Kota Ito, Kazutaka Nishikawa, Atsushi Miura, Hiroshi Toshiyoshi, and Hideo Iizuka. Dynamic Modulation of Radiative Heat Transfer beyond the Blackbody Limit. *Nano Letters*, 17(7):4347–4353, July 2017.

[64] Nathan H. Thomas, Zhen Chen, Shanhui Fan, and Austin J. Minnich. Semiconductor-based Multilayer Selective Solar Absorber for Unconcentrated Solar Thermal Energy Conversion. *Scientific Reports*, 7(1):5362, July 2017.

[65] Ruud Kaempener. Solar heat for industrial processes. *IEA-ETSAP and IRENA Technology Brief E21*, 2015.

[66] XiaoZhi Lim. How heat from the sun can keep us all cool. *Nature*, 542:23–24, 2017.

[67] Daniel Kraemer, Bed Poudel, Hsien-Ping Feng, J. Christopher Caylor, Bo Yu, Xiao Yan, Yi Ma, Xiaowei Wang, Dezhi Wang, Andrew Muto, Kenneth McEnaney, Matteo Chiesa, Zhifeng Ren, and Gang Chen. High-performance flat-panel solar thermoelectric generators with high thermal concentration. *Nat. Mater.*, 10(7):532–538, 2011.

[68] Daniel Kraemer, Qing Jie, Kenneth McEnaney, Feng Cao, Weishu Liu, Lee A. Weinstein, James Loomis, Zhifeng Ren, and Gang Chen. Concentrating solar thermoelectric generators with a peak efficiency of 7.4%. *Nat. Energy*, 1:16153, 2016.

[69] Hazim Mohameed Qiblawey and Fawzi Banat. Solar thermal desalination technologies. *Desalination*, 220(1–3):633–644, 2008.

[70] D. E. Ackley and J. Tauc. Silicon films as selective absorbers for solar energy conversion. *Appl. Opt.*, 16(11):2806–2809, 1977.

[71] D. C. Booth, D. D. Allred, and B. O. Seraphin. Stabilized cvd amorphous silicon for high-temperature photothermal solar-energy conversion. *Sol. Energy Mater.*, 2(1):107–124, 1979.

[72] Peter Bermel, Michael Ghebrebrhan, Walker Chan, Yi Xiang Yeng, Mohammad Araghchini, Rafif Hamam, Christopher H. Marton, Klavs F. Jensen, Marin Soljačić, John D. Joannopoulos, Steven G. Johnson, and Ivan Celanovic. Design and global optimization of high-efficiency thermophotovoltaic systems. *Opt. Express*, 18(S3):A314–A334, 2010.

[73] Jaeyun Moon, Dylan Lu, Bryan VanSaders, Tae Kyoung Kim, Seong Deok Kong, Sungho Jin, Renkun Chen, and Zhaowei Liu. High performance multi-scaled nanostructured spectrally selective coating for concentrating solar power. *Nano Energy*, 8:238–246, 2014.

[74] Edward D. Palik. *Handbook of Optical Constants of Solids*, volume 1-3. Academic Press, San Diego, 1985.

[75] Dan Goldschmidt. Amorphous germanium as a medium temperature solar selective absorber. *Thin Solid Films*, 90(2):139–143, 1982.

[76] F. Edelman, Y. Komem, M. Bendayan, and R. Beserman. On the crystallization of amorphous germanium films. *Appl. Surf. Sci.*, 70–71, Part 2(0):727–730, 1993.

[77] S. G. Tomlin, E. Khawaja, and G. K. M. Thutupalli. The optical properties of amorphous and crystalline germanium. *Journal of Physics C: Solid State Physics*, 9(23):4335, 1976.

[78] Stéphane Larouche and Ludvik Martinu. Openfilters: open-source software for the design, optimization, and synthesis of optical filters. *Appl. Opt.*, 47(13):C219–C230, 2008.

[79] Michael F. Modest. *Radiative Heat Transfer (Third Edition)*. Academic Press, Boston, 2013.

[80] J. Als-Nielsen and Des McMorrow. *Elements of Modern X-ray Physics.*, volume 2nd ed. Wiley, 2011.

[81] Coblentz Society. *NIST Chemistry WebBook, NIST Standard Reference Database Number 69, eds. P.J. Linstrom and W.G. Mallard*, chapter Infrared Spectrum. National Institute of Standards and Technology, Gaithersburg, MD, 1969.

[82] Daniel Kraemer, Kenneth McEnaney, Feng Cao, Zhifeng Ren, and Gang Chen. Accurate determination of the total hemispherical emittance and solar absorptance of opaque surfaces at elevated temperatures. *Sol. Energy Mater. Sol. Cells*, 132:640–649, 2015.

[83] Merav Muallem, Alex Palatnik, Gilbert D. Nessim, and Yaakov R. Tischler. Room temperature fabrication of dielectric bragg reflectors composed of a caf2/zns multilayered coating. *ACS Appl. Mater. Interfaces*, 7(1):474–481, 2015.

[84] N. S. Gluck, H. Sankur, and W. J. Gunning. Ion-assisted laser deposition of caf2 thin films at low temperatures. *J. Vac. Sci. Technol., A*, 7(5):2983–2987, 1989.

[85] Nathan H. Thomas, Michelle C. Sherrott, Jeremy Broulliet, Harry A. Atwater, and Austin J. Minnich. Electronic Modulation of Near Field Radiative Transfer in Graphene Field Effect Heterostructures. *In preparation*, 2019.

[86] D. Polder and M. Van Hove. Theory of Radiative Heat Transfer between Closely Spaced Bodies. *Physical Review B*, 4(10):3303–3314, November 1971.

[87] Sergei M. Rytov. Theory of electric fluctuations and thermal radiation. *Air Force Cambrige Research Center, Bedford, MA*, 1953.

[88] Sergei M. Rytov, Yurii A. Kravstov, and Valeryan I. Tatarskii. *Principles of Statistical Radiophysics*, volume 3. Springer-Verlag, 1989.

[89] A. Narayanaswamy and Y. Zheng. A Green's function formalism of energy and momentum transfer in fluctuational electrodynamics. *Journal of Quantitative Spectroscopy and Radiative Transfer*, 132(0):12–21, January 2013.

[90] Geoff Wehmeyer, Tomohide Yabuki, Christian Monachon, Junqiao Wu, and Chris Dames. Thermal diodes, regulators, and switches: Physical mechanisms and potential applications. *Applied Physics Reviews*, 4(4):041304, November 2017.

[91] Q. S. Shu, J. A. Demko, and J. E. Fesmire. Heat switch technology for cryogenic thermal management. *IOP Conference Series: Materials Science and Engineering*, 278(1):012133, 2017.

[92] Jon F. Ihlefeld, Brian M. Foley, David A. Scrymgeour, Joseph R. Michael, Bonnie B. McKenzie, Douglas L. Medlin, Margeaux Wallace, Susan Trolier-McKinstry, and Patrick E. Hopkins. Room-Temperature Voltage Tunable Phonon Thermal Conductivity via Reconfigurable Interfaces in Ferroelectric Thin Films. *Nano Letters*, 15(3):1791–1795, March 2015.

[93] Brian M. Foley, Margeaux Wallace, John T. Gaskins, Elizabeth A. Paisley, Raegan L. Johnson-Wilke, Jong-Woo Kim, Philip J. Ryan, Susan Trolier-McKinstry, Patrick E. Hopkins, and Jon F. Ihlefeld. Voltage-Controlled Bistable Thermal Conductivity in Suspended Ferroelectric Thin-Film Membranes. *ACS Applied Materials & Interfaces*, 10(30):25493–25501, August 2018.

[94] Juan Antonio Seijas-Bellido, Carlos Escorihuela-Sayalero, Miquel Royo, Mathias P. Ljungberg, Jacek C. Wojdeł, Jorge Íñiguez, and Riccardo Rurali. A phononic switch based on ferroelectric domain walls. *Physical Review B*, 96(14):140101, October 2017.

[95] Ruiting Zheng, Jinwei Gao, Jianjian Wang, and Gang Chen. Reversible temperature regulation of electrical and thermal conductivity using liquid–solid phase transitions. *Nature Communications*, 2:289, April 2011.

[96] Hwan Sung Choe, Joonki Suh, Changhyun Ko, Kaichen Dong, Sangwook Lee, Joonsuk Park, Yeonbae Lee, Kevin Wang, and Junqiao Wu. Enhancing Modulation of Thermal Conduction in Vanadium Dioxide Thin Film by Nanostructured Nanogaps. *Scientific Reports*, 7(1):7131, August 2017.

[97] Renjie Chen, Yalong Cui, He Tian, Ruimin Yao, Zhenpu Liu, Yi Shu, Cheng Li, Yi Yang, Tianling Ren, Gang Zhang, and Ruqiang Zou. Controllable Thermal Rectification Realized in Binary Phase Change Composites. *Scientific Reports*, 5:8884, March 2015.

[98] Kwangnam Kim and Massoud Kaviany. Thermal conductivity switch: Optimal semiconductor/metal melting transition. *Physical Review B*, 94(15):155203, October 2016.

[99] Jungwoo Shin, Minjee Kang, Tsunghan Tsai, Cecilia Leal, Paul V. Braun, and David G. Cahill. Thermally Functional Liquid Crystal Networks by Magnetic Field Driven Molecular Orientation. *ACS Macro Letters*, 5(8):955–960, August 2016.

[100] Soumyadipta Basu and Mathieu Francoeur. Near-field radiative transfer based thermal rectification using doped silicon. *Applied Physics Letters*, 98(11):113106, March 2011.

[101] Hideo Iizuka and Shanhui Fan. Rectification of evanescent heat transfer between dielectric-coated and uncoated silicon carbide plates. *Journal of Applied Physics*, 112(2):024304, July 2012.

[102] Junlong Kou and Austin J. Minnich. Dynamic optical control of near-field radiative transfer. *Optics Express*, 26(18):A729–A736, September 2018.

[103] Kota Ito, Kazutaka Nishikawa, Hideo Iizuka, and Hiroshi Toshiyoshi. Experimental investigation of radiative thermal rectifier using vanadium dioxide. *Applied Physics Letters*, 105(25):253503, December 2014.

[104] Feng Wang, Yuanbo Zhang, Chuanshan Tian, Caglar Girit, Alex Zettl, Michael Crommie, and Y. Ron Shen. Gate-Variable Optical Transitions in Graphene. *Science*, 320(5873):206–209, April 2008.

[105] Marcus Freitag, Hsin-Ying Chiu, Mathias Steiner, Vasili Perebeinos, and Phaedon Avouris. Thermal infrared emission from biased graphene. *Nature Nanotechnology*, 5(7):497–501, July 2010.

[106] Zheyu Fang, Sukosin Thongrattanasiri, Andrea Schlather, Zheng Liu, Lulu Ma, Yumin Wang, Pulickel M. Ajayan, Peter Nordlander, Naomi J. Halas, and F. Javier García de Abajo. Gated Tunability and Hybridization of Localized

Plasmons in Nanostructured Graphene. *ACS Nano*, 7(3):2388–2395, March 2013.

[107] Victor W. Brar, Michelle C. Sherrott, Min Seok Jang, Seyoon Kim, Laura Kim, Mansoo Choi, Luke A. Sweatlock, and Harry A. Atwater. Electronic modulation of infrared radiation in graphene plasmonic resonators. *Nature Communications*, 6:7032, May 2015.

[108] Michelle C. Sherrott, Philip W. C. Hon, Katherine T. Fountaine, Juan C. Garcia, Samuel M. Ponti, Victor W. Brar, Luke A. Sweatlock, and Harry A. Atwater. Experimental Demonstration of >230° Phase Modulation in Gate-Tunable Graphene–Gold Reconfigurable Mid-Infrared Metasurfaces. *Nano Letters*, 17(5):3027–3034, May 2017.

[109] Jaesung Lee, Zenghui Wang, Keliang He, Rui Yang, Jie Shan, and Philip X.-L. Feng. Electrically tunable single- and few-layer MoS2 nanoelectromechanical systems with broad dynamic range. *Science Advances*, 4(3):eaao6653, March 2018.

[110] Bai Song, Anthony Fiorino, Edgar Meyhofer, and Pramod Reddy. Near-field radiative thermal transport: From theory to experiment. *AIP Advances*, 5(5):053503, May 2015.

[111] Z. M. Zhang and S. Basu. Entropy flow and generation in radiative transfer between surfaces. *International Journal of Heat and Mass Transfer*, 50(3):702–712, February 2007.

[112] Alejandro W. Rodriguez, Ognjen Ilic, Peter Bermel, Ivan Celanovic, John D. Joannopoulos, Marin Soljačić, and Steven G. Johnson. Frequency-Selective Near-Field Radiative Heat Transfer between Photonic Crystal Slabs: A Computational Approach for Arbitrary Geometries and Materials. *Physical Review Letters*, 107(11):114302, September 2011.

[113] Karl Joulain, Jérémie Drevillon, and Philippe Ben-Abdallah. Noncontact heat transfer between two metamaterials. *Physical Review B*, 81(16):165119, April 2010.

[114] Kaifeng Chen, Parthiban Santhanam, Sunil Sandhu, Linxiao Zhu, and Shanhui Fan. Heat-flux control and solid-state cooling by regulating chemical potential of photons in near-field electromagnetic heat transfer. *Physical Review B*, 91(13):134301, April 2015.

[115] A. Narayanaswamy and Y. Zheng. A Green's function formalism of energy and momentum transfer in fluctuational electrodynamics. *Journal of Quantitative Spectroscopy and Radiative Transfer*, 132(0):12–21, January 2014.

[116] Ognjen Ilic, Marinko Jablan, John D. Joannopoulos, Ivan Celanovic, Hrvoje Buljan, and Marin Soljačić. Near-field thermal radiation transfer controlled by plasmons in graphene. *Physical Review B*, 85(15):155422, April 2012.

[117] V. B. Svetovoy, P. J. van Zwol, and J. Chevrier. Plasmon enhanced near-field radiative heat transfer for graphene covered dielectrics. *Physical Review B*, 85(15):155418, April 2012.

[118] Ognjen Ilic, Nathan H. Thomas, Thomas Christensen, Michelle C. Sherrott, Marin Soljačić, Austin J. Minnich, Owen D. Miller, and Harry A. Atwater. Active Radiative Thermal Switching with Graphene Plasmon Resonators. *ACS Nano*, March 2018.

[119] P. J. van Zwol, S. Thiele, C. Berger, W. A. de Heer, and J. Chevrier. Nanoscale Radiative Heat Flow due to Surface Plasmons in Graphene and Doped Silicon. *Physical Review Letters*, 109(26):264301, December 2012.

[120] Georgia T. Papadakis, Bo Zhao, Siddharth Buddhiraju, and Shanhui Fan. Gate-tunable near-field heat transfer. *arXiv:1812.02882 [physics]*, December 2018. arXiv: 1812.02882.

[121] L. A. Falkovsky. Optical properties of graphene. *Journal of Physics: Conference Series*, 129(1):012004, 2008.

[122] T.J. Lyon, J. Sichau, A. Dorn, A. Centeno, A. Pesquera, A. Zurutuza, and R.H. Blick. Probing Electron Spin Resonance in Monolayer Graphene. *Physical Review Letters*, 119(6):066802, August 2017.

[123] Riccardo Messina and Philippe Ben-Abdallah. Graphene-based photovoltaic cells for near-field thermal energy conversion. *Scientific Reports*, 3:1383, 2013.

[124] Steven G. Johnson. The NLopt nonlinear-optimization package.

[125] M J D Powell. The BOBYQA algorithm for bound constrained optimization without derivatives. *Department of Applied Mathematics and Theoretical Physics, Cambridge England, technical report*, page NA2009/06, 2009.

[126] Karl Joulain, Rémi Carminati, Jean-Philippe Mulet, and Jean-Jacques Greffet. Definition and measurement of the local density of electromagnetic states close to an interface. *Physical Review B*, 68(24):245405, December 2003.

[127] Chen-Cai Song, Tong-Biao Wang, Qing-Hua Liao, Tian-Bao Yu, and Nian-Hua Liu. Electromagnetic local density of states in graphene-covered hyperbolic metamaterial. *The European Physical Journal B*, 90(10), October 2017.

[128] Jan Kischkat, Sven Peters, Bernd Gruska, Mykhaylo Semtsiv, Mikaela Chashnikova, Matthias Klinkmüller, Oliana Fedosenko, Stephan Machulik, Anna Aleksandrova, Gregorii Monastyrskyi, Yuri Flores, and W. Ted Masselink. Mid-infrared optical properties of thin films of aluminum oxide, titanium dioxide, silicon dioxide, aluminum nitride, and silicon nitride. *Applied Optics*, 51(28):6789–6798, October 2012.

[129] T. S. Eriksson, A. Hjortsberg, G. A. Niklasson, and C. G. Granqvist. Infrared optical properties of evaporated alumina films. *Applied Optics*, 20(15):2742–2746, August 1981.

[130] Rei Kitamura, Laurent Pilon, and Miroslaw Jonasz. Optical constants of silica glass from extreme ultraviolet to far infrared at near room temperature. *Applied Optics*, 46(33):8118–8133, November 2007.

[131] T. J. Bright, J. I. Watjen, Z. M. Zhang, C. Muratore, and A. A. Voevodin. Optical properties of HfO2 thin films deposited by magnetron sputtering: From the visible to the far-infrared. *Thin Solid Films*, 520(22):6793–6802, September 2012.

[132] Giuseppe Cataldo, James A. Beall, Hsiao-Mei Cho, Brendan McAndrew, Michael D. Niemack, and Edward J. Wollack. Infrared dielectric properties of low-stress silicon nitride. *Optics Letters*, 37(20):4200–4202, October 2012.

[133] C. M. Osburn and E. J. Weitzman. Electrical Conduction and Dielectric Breakdown in Silicon Dioxide Films on Silicon. *Journal of The Electrochemical Society*, 119(5):603–609, May 1972.

[134] Mohammad Ghashami, Hongyao Geng, Taehoon Kim, Nicholas Iacopino, Sung Kwon Cho, and Keunhan Park. Precision Measurement of Phonon-Polaritonic Near-Field Energy Transfer between Macroscale Planar Structures Under Large Thermal Gradients. *Physical Review Letters*, 120(17):175901, April 2018.

[135] Xuesong Li, Yanwu Zhu, Weiwei Cai, Mark Borysiak, Boyang Han, David Chen, Richard D. Piner, Luigi Colombo, and Rodney S. Ruoff. Transfer of Large-Area Graphene Films for High-Performance Transparent Conductive Electrodes. *Nano Letters*, 9(12), December 2009.

[136] Robert D. Deegan, Olgica Bakajin, Todd F. Dupont, Greb Huber, Sidney R. Nagel, and Thomas A. Witten. Capillary flow as the cause of ring stains from dried liquid drops. *Nature*, 389(6653):827–829, October 1997.

[137] N. S. Gluck, H. Sankur, and W. J. Gunning. Ion-assisted laser deposition of CaF2 thin films at low temperatures. *Journal of Vacuum Science & Technology A: Vacuum, Surfaces, and Films*, 7(5):2983–2987, 1989.

[138] A. Donnadieu and B. O. Seraphin. Optical performance of absorber-reflector combinations for photothermal solar energy conversion. *Journal of the Optical Society of America*, 68(3):292–297, March 1978.

[139] D. C. Booth, D. D. Allred, and B. O. Seraphin. RETARDING CRYSTALLIZATION OF CVD AMORPHOUS-SILICON BY ALLOYING. *Journal of Non-Crystalline Solids*, 35-6(JAN-):213–218, 1980.

[140] Vito Sorianello, Lorenzo Colace, Nicola Armani, Francesca Rossi, Claudio Ferrari, Laura Lazzarini, and Gaetano Assanto. Low-temperature germanium thin films on silicon. *Optical Materials Express*, 1(5):856–865, September 2011.

[141] Svend-Age Biehs and Philippe Ben-Abdallah. Near-Field Heat Transfer between Multilayer Hyperbolic Metamaterials. *Zeitschrift für Naturforschung A*, 72(2):115–127, 2016.

[142] Hamed Dalir, Yang Xia, Yuan Wang, and Xiang Zhang. Athermal Broadband Graphene Optical Modulator with 35 GHz Speed. *ACS Photonics*, 3(9):1564–1568, September 2016.

[143] Ming Liu, Xiaobo Yin, Erick Ulin-Avila, Baisong Geng, Thomas Zentgraf, Long Ju, Feng Wang, and Xiang Zhang. A graphene-based broadband optical modulator. *Nature*, 474(7349):64–67, June 2011.

[144] J. A. Fleck and M. D. Feit. Beam propagation in uniaxial anisotropic media. *JOSA*, 73(7):920–926, July 1983.

[145] Ognjen Ilic. *Nanophotonics for tailoring the flow of thermal electromagnetic radiation*. PhD thesis, Massachusetts Institute of Technology, 2015.

[146] J. E. Sipe. New Green-function formalism for surface optics. *Journal of the Optical Society of America B*, 4(4):481–489, April 1987.

[147] Karl Joulain, Jean-Philippe Mulet, François Marquier, Rémi Carminati, and Jean-Jacques Greffet. Surface electromagnetic waves thermally excited: Radiative heat transfer, coherence properties and Casimir forces revisited in the near field. *Surface Science Reports*, 57(3), May 2005.